SYNTHESIS AND TESTING OF MIXED MAGNETITE AND IRON CARBIDE NANOCATALYSTS FOR ENHANCED SLURRY PHASE FISCHER TROPSCH SYNTHESIS

Obert Mupomoki

[BEng. Hons. NUST]

A thesis submitted in the College of Agriculture, Engineering and Science

University of KwaZulu-Natal

Durban

In fulfilment of the requirements for the degree

Master of Science in Engineering, Chemical Engineering

June 2018

Supervisor: Dr. David Lokhat.

Declaration:

I, Obert Mupomoki declare that:

The research reported in this dissertation/thesis, except where otherwise indicated, is my original work.

(i) This dissertation/thesis has not been submitted for any degree or examination at any other university.

(ii) This dissertation/thesis does not contain other persons' data, pictures, graphs or other information, unless specifically acknowledged as being sourced from other persons.

(iii) This dissertation/thesis does not contain other persons' writing, unless specifically acknowledged as being sourced from other researchers. Where other written sources have been quoted, then:

a) their words have been re-written, but the general information attributed to them has been referenced;

b) where their exact words have been used, their writing has been placed inside quotation marks, and referenced.

(iv) Where I have reproduced a publication of which I am an author, co-author or editor, I have indicated in detail which part of the publication was actually written by myself alone and have fully referenced such publications.

(v) This dissertation/thesis does not contain text, graphics or tables copied and pasted from the Internet, unless specifically acknowledged, and the source being detailed in the dissertation/thesis and in the References sections.

Signed: _____

Date: _____

As the candidate's supervisor, I, Dr. D. Lokhat agree to the submission of this dissertation:

_____

Dr. David Lokhat

Acknowledgements:

I would like to take this opportunity to acknowledge and extend my deepest gratitude to my supervisor Doctor David Lokhat for his invaluable contributions in this project. It's been a privilege working with him as he was always available to give me the much needed insights and guidance in the execution of this work. Thank you for giving me the opportunity to work on this exciting project.

I would also like to acknowledge Sasol for the financial support and the opportunities they availed to me so that I could interact with some of their staff and other students working on similar projects. The presentations we had on platforms such as the 2017 Sasol University Research Seminar were an eye opener.

The invaluable support from the Chemical Engineering staff at the University of KwaZulu – Natal is hereby acknowledged. I would like to also thank the Chemical Engineering chemical technicians for their support. Special mention goes to Ms Thobekile Mafokeng, Ms Xoli Hadebe and Mr Rajen Singh. I would also like to express my gratitude for the help I got from the Chemical Engineering Workshop staff, particularly Ken Jack, Danny Singh, Gerald, Patrick Mlambo, Elliot Mlambo and Preyothen Nayager.

I would like to express my deepest gratitude to the staff at the UKZN Microscopy and Microanalysis Unit for their support in the TEM, SEM and EDX analyses of my catalysts samples. Special thanks to Phillip Christopher, Subashen Naidu and Vishal Bharuth for helping me to understand the whole microanalysis concept. Pradeep Suthan is acknowledged for his friendship and help in the XRD analyses of all my catalysts.

Personal thanks go to my postgraduate colleagues; Edward Marondedze, Tauheedah Fakir, Phakamile Ndlovu, Tshepo Mahura, Lindelani Ndovu, Paul Ngcobo, Marcin Durski, Eva Mary and Sandile Nkwanyana. I would also like to thank my mother, my dad and my girlfriend Tendai for their support and encouragement.

Finally, I would like to thank God for the unconditional Love and Grace. Father I thank you for this yet another milestone.

Abstract:

This study focused on the preparation and performance testing of iron-based nanocatalysts. The performance evaluation for slurry phase Fischer – Tropsch reaction was carried out in a bench-scale compact reactor. The investigation was focused on determining whether the product yield and hydrocarbons distribution from the processing of syngas can be significantly improved through the coupled use of unsupported magnetite and preformed iron carbide nanocatalysts. Iron oxides and iron carbide nanoparticles (NPs) are believed to be the active phases in the Fischer–Tropsch reaction. In this work, effects of nanoscale magnetite and iron carbide particles on the rate, yield, selectivity and product distribution of the Fischer–Tropsch Synthesis (FTS) were investigated in a bench scale slurry phase reactor. Nanoparticles were prepared separately and mixed in different proportions to obtain the required catalysts mixtures. Magnetite catalysts were prepared using a modified solvothermal synthesis route while Iron carbide nanocatalysts were prepared using three (3) different biopolymer routes in which an iron precursor was suspended in the biopolymer matrix. The resulting product was subsequently exposed to a thermal degradation step in a box furnace under a constant flow of nitrogen to form carbides. Structural characterization of the catalysts was performed by TEM, SEM, EDX and XRD analyses. Particle sizes of both magnetite and iron carbide nanoparticles as determined from XRD patterns (Scherrer equation) and TEM images was about 8.07 and 13 nm, respectively. Catalyst evaluation was conducted in a 600ml slurry phase stainless steel Parr reactor and the system performance was classified according to methane selectivity, C_2-C_4 selectivity and the yield of C_{5+} hydrocarbons. The results revealed that, the addition of preformed iron carbide nanocatalysts resulted in better yields of higher range hydrocarbons. A C_{5+} hydrocarbons selectivity of 82% was recorded with a catalysts mixture containing 50% iron carbides. This was accompanied by a minimum methane selectivity of 6.9%.

List of publications and conference contributions:

1. Mupomoki, O. and Lokhat, D., "Synthesis and Characterisation of magnetite and iron carbide nanocatalysts for enhanced slurry phase Fischer – Tropsch synthesis", University of KwaZulu – Natal Postgraduate Research Symposium (2017) Westville, Durban South Africa, 26th October 2017.

2. Mupomoki, O. and Lokhat, D., "Synthesis and testing of mixed magnetite and iron carbide nanocatalysts for enhanced slurry phase Fischer – Tropsch synthesis", Sasol University Research Seminar (2017), Wierda Valley, Sandton, South Africa, 02 November 2017.

3. Mupomoki, O. and Lokhat, D., "Synthesis and testing of mixed magnetite and iron carbide nanocatalysts for enhanced slurry phase Fischer – Tropsch synthesis", Catalysis Society of South Africa, CATSA 2017, Pilanesberg Game Reserve, Pilanesberg, South Africa, 19th – 22end November 2017.

Nomenclature:

Notation		Unit
A_i	Response area of component *i* in chromatogram	
đc-$_{XRD}$	Average crystallite diameter from XRD analysis	nm
d_p	Particle diameter	m
$f_{FID,i}$	FID response factor of component *i*	
$f_{TCD,i}$	TCD response factor of component *i*	
k	Debye-Scherrer shape factor	
N_c	Number of carbon atoms in a molecule	
n	Number of carbon atoms in a molecule	
n_i	Molar flow rate of component *i*	mol/min
p_g	Chain growth probability	
W_n	Mass fraction of a product consisting of carbon number n	wt%

Greek letters		
α	Chain growth probability	
β	Line broadening at FWHM	radians
λ	Wavelength	m

Abbreviations	
ASF	Anderson-Schulz-Flory
EDX	Energy Dispersive X-ray
FWHM	Full Width at Half Maximum intensity
FT	Fischer-Tropsch
FID	Flame Ionisation Detector
GC	Gas Chromatograph
HCNs	Hydrocarbons
MS	Mass Spectrometer
NTP	Normal Temperature and Pressure (25 °C, 1.013 bar)
rpm	Revolutions per minute
SEM	Scanning Electron Microscope
SV	Space Velocity
sccm	standard cubic centimeter per minute
TCD	Thermal Conductivity Detector
TEM	Transmission Electron Microscope
TPR	Temperature Programmed Reduction
VOC	Volatile Organic Compounds
XRD	X-ray Diffraction

Table of contents

List of Figures:

List of Tables:

Chapter 1

Preliminaries:

1 Introduction:

To show the context and relevance of this current study, this chapter is aimed at providing the reader with a reasonable background on the Fischer–Tropsch synthesis. It includes studies done on various projects involving slurry phase Fischer–Tropsch Synthesis (FTS). A brief overview of enhanced slurry phase reactor technologies is presented as well as iron phases that are believed to be active in FT catalysis. The chapter also introduces the reader to the need for process intensification and the idea of robust catalyst design for the development of catalytic processes.

1.1 Background:

The ever-growing global population has brought associated challenges such as the provision of energy to current societies. Environmental and health concerns have also continued to put more pressure to society on how to manage these issues. It is believed that catalysts have the potential to leverage the optimal conversion of renewable resources to usable transportation fuels and chemicals. Amongst these materials are iron oxide nanoparticles which have found wide application in the field of catalysis, medicine and water treatment. Their preparation and application in organic reactions as catalysts has lately been an essential area of research and development. A lot of research has been happening in the area of heterogeneous nanocatalysis and in particular, significant attention has been from industry and academia. The physical and chemical properties of nanoparticles are especially different from those of bulk materials as they possess large surface area per volume ratios. This gives them the advantage of being used as good catalysts in the production of various chemicals (Sun et al., 2011). In addition, they are more dispersible in heterogeneous catalysis such as the slurry phase FTS.

Fischer and Tropsch in the early 1920's (Germany) invented a technology to produce long chain hydrocarbons from carbon monoxide (CO) and hydrogen (H_2) using iron catalysts. This discovery marked the beginning of what is now popularly known as the Fischer-Tropsch Synthesis (FTS). The process came at a time when there was considerable work being done to find alternatives to reduce massive importation of crude oil for transportation fuels. Initially it was done at high pressures of up to 300 bars (Fischer *et al*., 1925) but when precipitated cobalt catalysts were used, low pressures (1–5 bar) were used to achieve the same results (Fischer and Tropsch, 1926). Recently there have been great strides that have been made with regards to methods for the preparation of metal oxide nanocatalysts

for use in Fischer–Tropsch Synthesis (FTS). These include water-oil micro-emulsion, solution precipitation, sol-gel processing, hydrothermal method and the solvothermal synthesis, just to mention a few (Lokhat et al., 2015).

The choice of catalysts preparation method is dependent on whether the process produces particles with the required particle size, size distribution and activity. The quantity of catalysts that can be produced using a particular method also dictates the type of preparation technique to be adopted since some methods result in the production of only a few grammes which will not be enough for large scale commercial operation. The cost of the process associated with each preparation technique in terms of precursor prices and purification processes is also considered. Amongst the various methods reported so far for the synthesis of magnetite, (which is one of the preferred catalysts for this work) the chemical co-precipitation of Fe^{2+} and Fe^{3+} salts by addition of sodium hydroxide is the simplest and cheapest. When using this method, ultrasonic agitation of the reaction medium during co-precipitation can aid in the formation of uniform nanosized particles by preventing agglomeration (Dang et al., 2009).

Iron – based catalysts are usually preferred over other transition metal catalysts because of their low price and easy availability. Their ability to catalyze both the Fischer – Tropsch and the water gas shift reactions (WGS) gives them an edge over most catalysts in the selection of catalysts for major chemical reactions especially those which are organic in nature. Recently Zeng et al. (2015) reported an efficient and facile route to synthesize highly crystalline magnetite nanoparticles using a modified solvothermal method. These nanoparticles can be conveniently used as catalysts for the slurry phase Fischer – Tropsch synthesis. The slurry phase reactor is considered to be the best in terms of flexibility during operation since it allows isothermal operation and efficient heat and mass transfer. It is the reactor that is expected to likely transform the future of Gas to liquid (GTL) operations in the world. The reactor can easily be scaled up or down without considerably affecting process operating parameters.

1.2 Sasol's slurry phase reactor (SPR):

The slurry bed reactor or the slurry phase reactor (SPR) came into operation at SASOL in May 1993 as a result of its continued research and development in reactor technologies (Espinoza et al., 1999). The idea of slurry phase processing in FT operations had been a topic of investigation for quite a long time which began in the 1950's until the late 70's, as pioneered by Kölbel and fellow researchers in the field of syngas processing. They made some great strides in this direction, but they however faced difficulties with the process pertaining the method of extracting the spent catalysts after the reaction. It was this challenge that lead to more research to be done in catalysts separation processes from products. Nowadays the use of magnetic separation and other proprietary separation techniques has since solved this problem for Sasol. This also necessitates the need for catalysts to be highly magnetic for use in

slurry phase processing and is of paramount importance since it will enable the application of this technology.

The slurry phase reactor was mainly designed with the idea of processing abundant methane gas to liquid transportation fuels. Other long chain hydrocarbons that can be used as raw materials for downstream process such as petrochemicals and pharmaceuticals can also be produced from this process. This process vessel is now one of the best performing reactors and of late, most of their fixed bed reactors have been replaced by giant slurry phase reactors as seen at Sasol II and III plants (Espinoza et al., 1999).

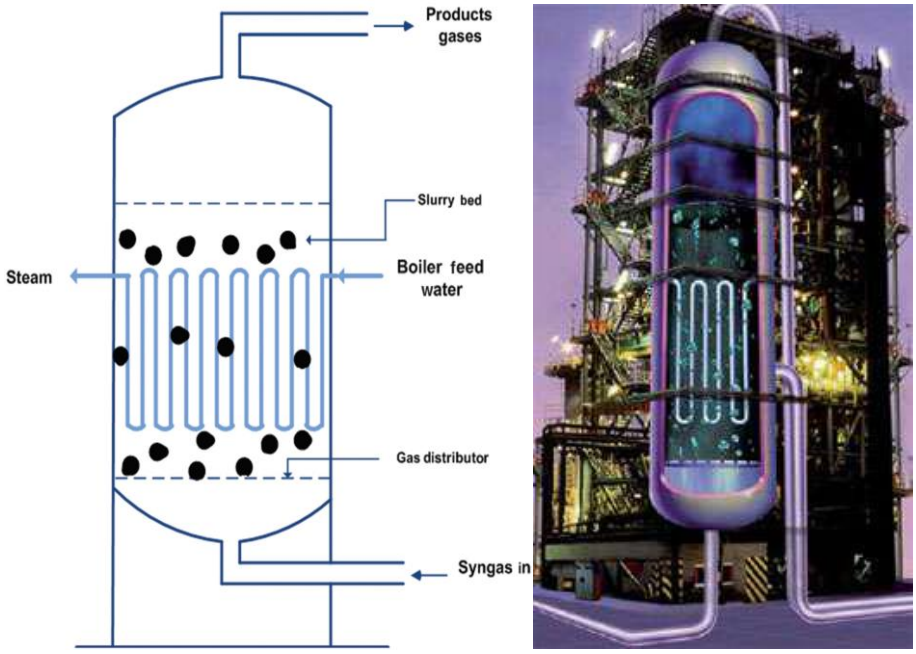

Figure 1. 1: The internal configuration of the Slurry Phase Reactor (Saeidi et al., 2014).

The advantage of the slurry phase reactor is that it is much simpler than the multitubular reactor since it is easier to fabricate. It is simply composed of a shell and cooling coils which serve as heat removal conduits from this highly exothermic reaction. Syngas is distributed at the bottom and it rises through the slurry. In this reactor, an initial solvent which is usually composed of various long-chain hydrocarbons is mixed with the solid catalysts particles to make the slurry. These long-chain hydrocarbons are thermally stable even at very high temperatures. The reactant gases (syngas) are usually forced to enter the reactor at a high pressure and hence bubbling and diffusing through the slurry. This results in a three-phase media as the gases contact the suspended catalysts particles and the slurry. Heavy liquid products that are formed by the reaction also condense and become part of the slurry. Some light and volatile liquid hydrocarbon products, water as well as gaseous products are diffused through the reactor and come out from the top of the reactor where they are condensed and collected. The use of this reactor has stimulated interest from industry and academia. More research on

enhanced reactor technologies which are likely to change the scale and product selectivities of current production rates per reactor is still ongoing.

1.3 Enhanced reactor technologies:

Current sizes of slurry phase FTS reactors in commercial operation are considerably massive. As a result, the use of technologies that enhance the level of productivity in Fischer – Tropsch operations will likely have an immense improvement on process economics and selectivity. Process intensification is a modern technology that is aimed at replacing gigantic, usually costly and somehow obsolete equipment with new pieces of equipment and processes that are compact and less energy intensive. The implementation of which has the potential to transform the face of the energy and petrochemicals industry. In particular, process intensification results in the development of smaller and compact processes which require less capital and have minimal wastes generated as a result of inefficiencies. The Slurry phase F–T synthesis is a prime candidate for process intensification, where the effect of nanosized catalysts, coupled with compact reactor technologies may result in improved heavy products selectivity. It will also bring about improvements in process chemistry, process steps and pave way for the use of processing technologies such as the use of microwaves, magnetic as well as centrifugal fields which are more intensified methods. Higher energy-efficiency, enhanced product specificity, CO_2 mitigation and waste minimization in processes are some of the benefits that come with process intensification (Lokhat et al., 2015).

1.3.1 Compact slurry phase reactors:

Catalytic compact reactors are an interesting alternative to conventional stirred tank reactors for gas-liquid and slurry phase reactions. The different types of reactors being commercially used are shown in figure 1.2. Production units employing intensified compact reactor principles have recently been made commercial by Velocys and Compact GTL (Jacobs, 2013). These technologies have reaped some benefits since they allow the utilization of smaller volumes of feedstock for the Fischer–Tropsch Synthesis. There has been concerns regarding conventional reactors, particularly size of Slurry Phase reactors, intensification of reactors has been considered in recent years and different advances have been put in place which include the design of advanced compact reactors. Monolithic, membrane and microstructured reactors are innovative alternatives that were developed based on modification and intensification of current configurations. Operating conditions were also tuned to bring improvements to FTS. In this work, focus was placed on the development of a catalysts mixture that would produce the best selectivity in Low Temperature F–T (LTFT) operations. To develop a robust industrial scale process for converting carbonaceous raw materials to hydrocarbons, a good knowledge of reactor and catalyst design as well as expertise in the production of clean syngas is necessary. This is particularly

true when dealing with the low temperature Fischer – Tropsch synthesis and aiming for higher selectivity for long chain hydrocarbons.

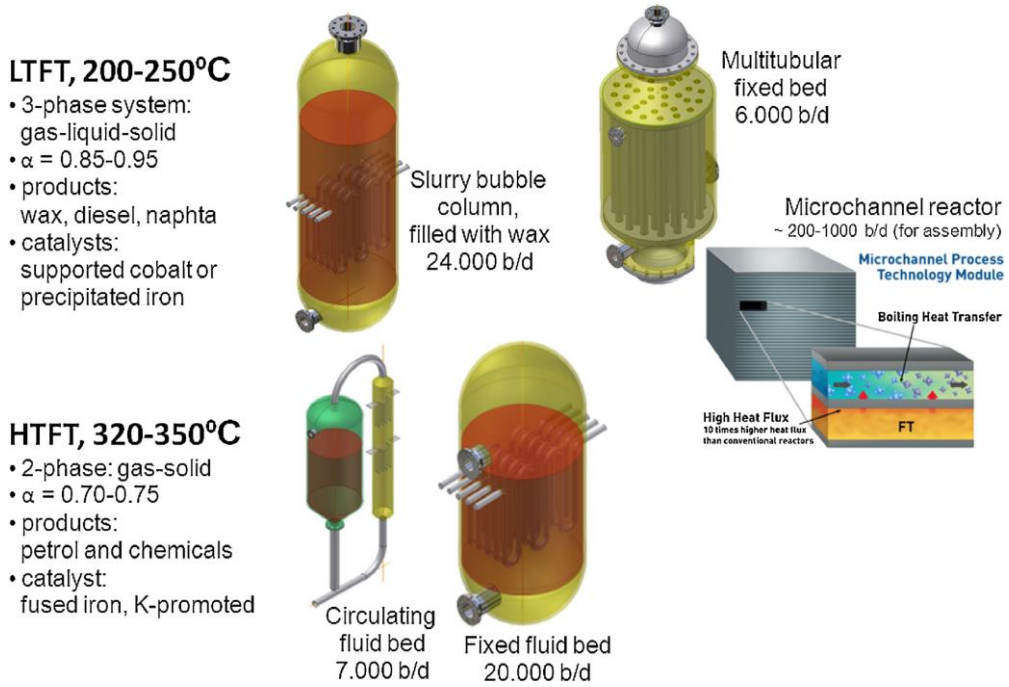

Figure 1. 2: High temperature and Low temperature F-T reactors with commercial relevance (figure on microchannel reactor: courtesy of Oxford Catalysis Group).

The challenge with iron-based Fischer Tropsch catalysts is the fact that, the composition of the active iron phases under reaction conditions is not clearly understood. Other researchers have reported that magnetite (Fe_3O_4) is the active phase and others are of the idea that the in-situ formation of iron carbides results in it being the active phase. Different carbides of iron have been prepared from iron catalysts by the controlled temperature reduction of iron oxides using carbon monoxide or synthesis gas. This however has the obvious challenge of failing to predict the extent of the carburization achieved. So, in effect the resulting catalysts will be a combination of several carbides, metallic iron, and iron oxides phases. Recently, Schnepp et al., (2010) used a biopolymer route to produce iron carbide nanocrystallites which were highly magnetic using several biopolymer matrices followed by a thermal degradation step. To better understand the role of iron carbide phases in enhancing slurry phase Fischer Tropsch synthesis this route of preparing iron carbide catalysts was used.

1.3.2 Iron based nanocatalysts:

Unlike industrial cobalt-based FTS catalysts which are active in the metallic form (Iglesia, 1997), iron-based catalysts are believed to behave in a different way. Although there is still debate on active phases in FTS, carbide phases (Shroff et al., 1995; Biel, 2005) are believed to be active phase in the reaction (Li et al., 2001). A trend that was reported by Malan et al. (1961) which laid out the changes in the

active phases of iron-based catalysts under Fischer – Tropsch conditions. They found that there is a continued change in the active phase which depends on the time on stream (TOS) as metallic iron is initially converted to cementite, followed by Hägg carbide and finally magnetite. This is depicted in figure 1.3 below which shows that magnetite phase dominates in the reaction system for a longer time on stream. A transformation of the carbides from Hägg carbide to Eckström-Adcock carbide was also reported to occur under these conditions as more carbon enrichment unfolds according to this order: Cementite (**1C**) ~ Hägg carbide (**2Cs**) ~ Eckström-Adcock carbide (**3Cs**)

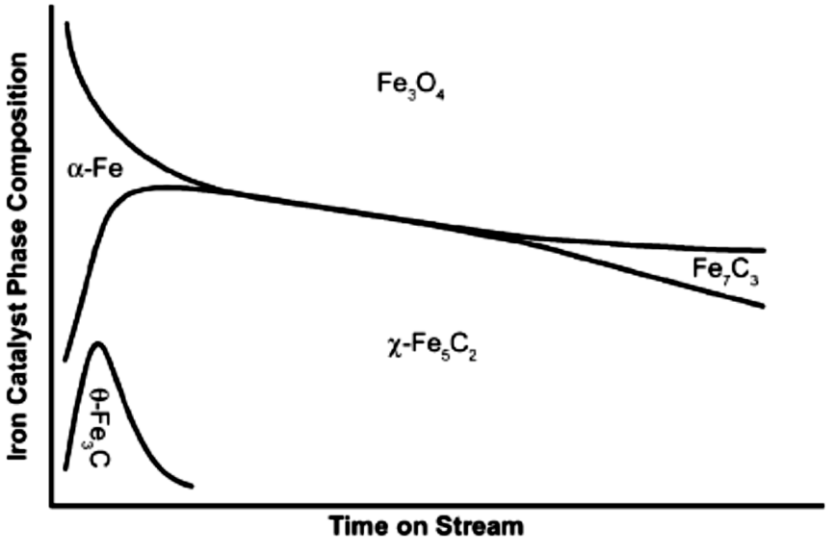

FiFigure 1. 3: Effects of time on stream on the phase changes in iron-based catalysts (adapted from Malan et aI, (1961)).

Before any catalysts are used in any Fischer – Tropsch synthesis regime, it is firstly activated either using hydrogen, syngas or carbon monoxide. It is in this process that some catalysts phase changes happen, and it has been reported by Herranz et al. (2006) that Hägg carbide was the most active phase in fixed bed FT experiments they did. These iron-based catalysts were tested for performance after they were exposed to several activation gases to yield different iron phases. Dry, (1981) also reported that, with iron based catalysts, after activation with H_2, metallic iron was formed and during reaction it was converted to several carbides as well as magnetite (Fe_3O_4). Herranz et al. (2006) also performed activation using CO and they yielded cementite as the active phase and they went on to use syngas which is a mixture of CO and H_2 and in this case, they produced Hägg carbide. Using the same fixed bed reactor, they tested these catalysts for their performance under industrial FT conditions. Performance was measured using CO conversion and 37% was achieved using cementite while Hägg carbide resulted in 74 % CO – conversion on a methane free basis. What was important from this study was the fact that, they also discovered that cementite can actually be transformed under Fischer – Tropsch conditions to Hägg carbide which was considered to be more active in this case. This agreed well with the observations and conclusions made by Malan et al., (1961) as illustrated above. The main

variable being the time on stream which when made long enough, a total conversion to Hägg carbide was assumed to be possible.

The above observations did not only bring some debate in the field of iron-based FTS, but it introduced some confusion as to which phase is actually active in the FTS. In the same period, Ning et al. (2006) got to work with the aim of unravelling this confusion and used iron based catalysts synthesised using the precipitation method. They also introduced some promoters in some of their samples while others remained unpromoted. The same type of reactor (a fixed bed) was used at 16 bar and 503K. CO was used as an activation gas and they carried out some PXRD to ascertain the phases both after activation and after the reaction. They reported that a maximum activity in terms of CO conversion was achieved at a TOS = 8 hour for the unprompted iron catalysts. They also managed to detect some iron carbides such as Fe_xC and Fe_5C_2 soon after activation of the unpromoted iron catalysts and during reaction it was found to be oxidised to Fe_3O_4. For the promoted iron catalysts which used copper Cu, potassium, K and Indium, carbides were also detected after reduction, but these remained for the entire reaction time of up to 29 hours TOS. Thus, they concluded that carbides are the active phase in FT reaction.

The oxidation of the iron carbides in the unpromoted iron catalysts was attributed to water oxidation. Excess water in FTS is thought to be responsible for the conversion of the various carbides to magnetite or even other iron oxides. This phenomenon was also believed to be responsible for the deactivation of iron based catalysts especially when there is high water gas shift activity. The situation is however different when promoters such as (K, Cu and In) are used as they are believed to supress this competing reaction in iron based Fischer-Tropsch reaction. This is the reason that Ning et al. (2006) used to justify the prolonged presence of iron carbides for the 29 hours of FT activity. Again, the issue of the active phase in the Fischer – Tropsch synthesis was not fully resolved and it therefore required further research. This resulted in more investigations being conducted in iron-based FTS catalysis for application in both fixed bed and slurry phase Fischer-Tropsch reactors.

1.4 Research Objectives:

Most of research that has been done on FT catalysis focused only on supported transition metals such as cobalt, iron, ruthenium and nickel since they are the most widely researched catalysts for organic syntheses as they have demonstrable activities in both academic and industrial FTS. Sasol adopted the slurry phase reactor system in May 1993 (Espinoza et al., 1999) and since then, realizations have been made that the reactor is best suited for processes aimed at producing long chain hydrocarbons. The reactor is very versatile in terms of efficient heat and mass transfer, but its massive size (10m dia., 60m height) makes it a good candidate for process intensification. Since it can be operated with cheap iron catalysts, it is imperative that properly configured, highly active, selective and robust catalysts be designed and synthesized for maximum hydrocarbons production.

The aim of this project was to investigate the effect of mixing two iron-based nanocatalysts on the Fischer–Tropsch product distribution and selectivity. In particular, the effect of using nanosized unsupported catalysts, coupled with efficient slurry mixing in a compact slurry phase FT reactor was studied to find if it can result in improved heavy products selectivity. The specific objectives of the study were: -

1. To synthesize nanosized magnetite and iron carbide nanocatalysts and characterize them using spectroscopic and microscopic characterization techniques.
2. To design, assemble and commission a bench scale slurry phase Fischer-Tropsch synthesis testing rig.
3. To study the comparative performances (with regard to product yield and selectivity) of magnetite and a magnetite/iron carbide nanoparticle mixture for low temperature slurry phase Fischer Tropsch (LTFT) reaction.
4. To assess whether the rate and product quality for slurry phase Fischer Tropsch reaction is improved by using nanocatalysts prepared via the solvothermal and biopolymer routes.

The main hypothesis was that a system incorporating iron nanocatalysts, efficient slurry mixing, and compact slurry phase reactor technology can be used to carry out slurry phase Fischer Tropsch synthesis and supersede the performance of currently available slurry phase reactors.

1.5 Outline of the dissertation:

In this chapter the reader has been familiarized with the fundamental aspects of the Fischer-Tropsch synthesis. The historical development of the process, reactors and catalysts that are best suited for the production of long chain hydrocarbons has been outlined. The need for process intensification for the reactors to improve heavy products selectivity and aspects of design and synthesis of robust catalysts has also been presented. The chapter concluded with the concept of catalysts phases that are present in the iron oxide-carbide system and the debate that still stands in terms of which phase is active for the Fischer-Tropsch reaction. Specific objectives of the current study were also laid out and these acted as the benchmark of all the activities that were done in this work.

Chapter 2 presents an overview of the current knowledge about iron-based Fischer-Tropsch catalysis and the underlying reactions that occur during the Fischer-Tropsch synthesis. Product distribution as predicted by Anderson, Schultz and Flory is discussed and factors that influence the kind of product distribution resulting from using such reaction conditions. The Idea of using different Fischer-Tropsch regimes to favour the production of a certain product cut such as heavy waxes or light olefins is also presented in this chapter and the economic implication of either operating in the Low Temperature range (LTFTS) or high temperature range (HTFTS). The chapter then goes onto discuss the catalysts

synthesis techniques that have been used to prepare iron oxide and carbide nanocatalysts for application in different reactions. Main emphasis was on those techniques that result in the production of closely controlled active catalysts for FTS. The advent of the Solvothermal and Biopolymer synthesis routes were then presented as the methods of choice for the preparation of catalysts which were used in this work.

Chapter 3 presents the Experimental Equipment and Methodologies that were used in this work and in particular, it presents the equipment that was used in the preparation of the catalysts. All the in-depth details of the amounts and sizes that were involved in this work is also presented. Characterisation equipment for the as-synthesised catalysts were also discussed as well as the conditions that resulted in optimal yield of catalysts samples having the desired particle size and size distribution. The scientific background and explanation of the characterisation techniques of catalysts used in this study closes the chapter with a clear illustration of what sort of calculations were made on the synthesised catalysts. This chapter also elaborates on the experimental setup and procedures that were followed during the performance testing of the synthesised catalysts and the nature of calculations that were performed. Formulae for mass balance calculations, conversions and selectivities of both gaseous and liquid products from the Fischer-Tropsch reaction is also expounded out here.

Chapter 4 begins with a presentation of the results of the microscopic characterisation of the as-synthesised catalysts. SEM, TEM and EDX analysis results are discussed and their interpretation given therein. PXRD results for both the magnetite and carbide catalysts are also presented, and comparisons of particle size and size distribution done on the results from TEM micrographs. Fischer-Tropsch catalyst performance testing results are also given, and the chapter closes with a discussion on the obtained products selectivity and distribution of the various hydrocarbons.

Chapter 5 gives overall conclusions and recommendations for future work in enhanced slurry phase iron-based Fischer-Tropsch catalysis.

Chapter 2

Literature Review:

2 Introduction:

This chapter provides the reader with a reasonable background on the Fischer–Tropsch Synthesis (FTS) as well as the catalysts that are used in the process. Catalysts preparation methods, particularly nanocatalysts are discussed. Emphasis is on iron-based Fischer-Tropsch catalysts (magnetite and iron carbide phases) which are believed to be the active phases in this surface polymerization reaction.

2.1 Fischer-Tropsch synthesis:

The Fischer – Tropsch synthesis converts synthesis gas (syngas), a mixture of hydrogen and carbon monoxide into liquid and gaseous hydrocarbons as well as oxygenates (alcohols, carbonyls and carboxylic acids). This gas to liquid (GTL) technology utilises syngas derived from, biomass, natural gas or coal to produce liquid transportation fuels and petrochemical industry feedstocks. The process is a promising alternative for producing chemicals and fuels from coal since it produces fuels that are free from nitrogen and sulphur compounds and hence cleaner combustion. Crude oil reserves are being depleted at a faster rate and the price of crude oil continues to increase. It is in this regard that the dependence on crude oil-based transportation fuels should be reduced.

Since its discovery in 1923 by Franz Fischer and Hans Tropsch, the process has gained widespread attention and interest by researchers and industrialists. Fischer and Tropsch managed to convert a mixture of hydrogen and carbon monoxide to a range of hydrocarbons using an iron catalyst (Fischer and Tropsch, 1926). Since then, more catalysts have been discovered and used for the process and these have different activities, selectivities and water-gas shift (WGS) activity. The choice of the catalyst to use therefore depends on these characteristics as well as the cost and the natural abundance of the catalyst precursors so that it can be used for commercial purposes.

2.2 Fischer-Tropsch reactions:

The Fischer –Tropsch Synthesis is basically a set of surface polymerization reactions which result in the formation of various oligomers with different carbon chain lengths, functional groups and therefore different physical states. The process is highly exothermic, and a wide range of products are produced. These include the main products, which are linear paraffins and α-olefins, as well as water as a by-product. Branched compounds and oxygenates such as alcohols, acids, aldehydes and ketones are some

of the products that are also formed. The chemical reactions that take place in FTS can be sub-divided into the following categories:

1. Main reactions,
2. Side reactions and
3. Reactions responsible for catalyst modification. These are as shown in equations (R2.1) to (R2.8) below (Weil and Lane, 1949):

Main reactions:

Paraffin /Alkanes formation:

$$n\mathrm{CO} + (2n + 1)\mathrm{H_2} \rightarrow \mathrm{C}_n\mathrm{H}_{2n+2} + n\mathrm{H_2O} \quad \text{(R2.1)}$$

Olefin /Alkenes formation:

$$n\mathrm{CO} + 2n\mathrm{H_2} \rightarrow \mathrm{C}_n\mathrm{H}_{2n} + n\mathrm{H_2O} \quad \text{(R2.2)}$$

Water-gas shift (WGS) reaction:

$$\mathrm{CO} + \mathrm{H_2O} \leftrightarrow \mathrm{CO_2} + \mathrm{H_2} \quad \text{(R2.3)}$$

Side reactions:

Alcohol production:

$$n\mathrm{CO} + 2n\mathrm{H_2} \rightarrow \mathrm{C}_n\mathrm{H}_{2n+1}\mathrm{OH} + (n-1)\mathrm{H_2O} \quad \text{(R2.4)}$$

Boudouard reaction:

$$2\mathrm{CO} \rightarrow \mathrm{C} + \mathrm{CO_2} \quad \text{(R2.5)}$$

Catalyst modifications:

Catalyst oxidation/ reduction:

a. $\mathrm{M}_x\mathrm{O}_y + y\mathrm{H_2} \leftrightarrow y\mathrm{H_2O} + x\mathrm{M}$ (R2.6)
b. $\mathrm{M}_x\mathrm{O}_y + y\mathrm{CO} \leftrightarrow y\mathrm{CO_2} + x\mathrm{M}$ (R2.7)

Bulk carbide formation:

$$y\mathrm{CO} + x\mathrm{M} \leftrightarrow \mathrm{MxCy} \quad \text{(R2.8)}$$

where n is the carbon number.

2.3 Fischer – Tropsch product spectrum:

Since the Fischer –Tropsch synthesis is a surface polymerization reaction (Schulz et al., 1988), the resulting products are diverse since it occurs through a stepwise growth process. Knowledge in predicting F-T product distribution remain crucial as it will give an insight into the nature of the products being formed. The hydrocarbon chain grows at the catalyst surface and a variety of mechanisms have been postulated to explain this growth. Some researchers have put forward a mechanism depicted in in

Figure 2.1 as shown. This mechanism postulates that the hydrocarbon chain either continue to grows or desorbs as soon as it is supplied with a hydrogen atom to form methane (Claeys and Van Steen, 2004). The chain growth probability is a measure of continuing chain growth. It is expressed as a probability factor α, which is also popularly known as the chain growth probability factor. For a good catalyst, this value should be large since an α value greater than 0.5 will yield valuable products (liquid hydrocarbons and waxes).

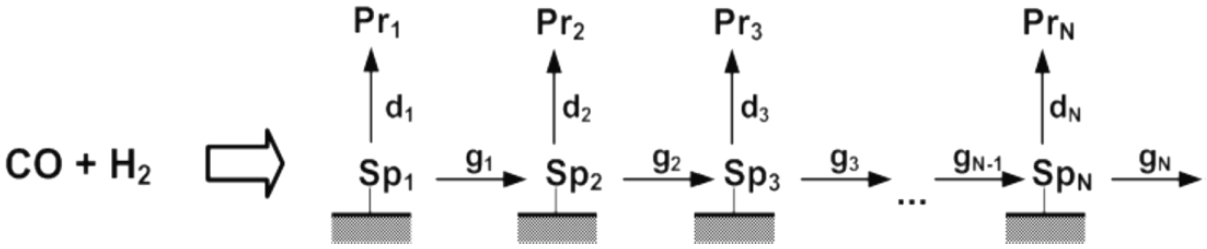

Figure 2. 1: Fischer-Tropsch step-wise growth process with a surface species (S_{pi}), products (P_{ri}) g: growth, d: desorption (Claeys and Van Steen, 2004).

The chain growth probability factor (α) can also be expressed as a ratio of the rate of chain growth (r_g) to the sum of the chain propagation and termination (r_d) terms as shown below.

$$\alpha = \frac{r_g}{r_g + \ r_d}$$

The product distribution can then be predicted if α, has no relationship with the number of carbon atoms in the resulting molecule. The rate of formation of a product Pr_n with n carbon atoms is given by:

$$r_{Pr_n} = \ r_{d_n} = \ \alpha^{n-1}.(1-\alpha).r_{f,1}$$

Here, $r_{f,1}$ is the rate at which the species with one (1) carbon atom is formed. All product compounds are formed via the formation of Sp_1 (see Fig. 2.1). Under transient conditions, the total molar rate of forming all products must be equal to the rate at which the species with 1 carbon atom is formed.

$$\frac{r_{Pr_n}}{\sum_{i=1}^{i=\infty} i.r_{Pr_n}} = X_n = \ \alpha^{n-1}.(1-\alpha)$$

From a commercial view point the mass fraction of a certain product is of more interest. The relative mass fraction of the product with n carbon atoms is given by:

$$W_n = \frac{n.r_{Pr_n}}{\sum_{i=1}^{i=\infty} i.r_{Pr_i}}$$

Which can also be linked to the Anderson-Schulz-Flory distribution:

$$\frac{W_n}{n} = \frac{r_{Pr_n}}{\sum_{i=1}^{i=\infty} i.r_{Pr_i}}$$

$$log\left(\frac{W_n}{n}\right) = log\left(r_{Pr_n}\right) - log\left(\sum_{i=1}^{i=\infty} i.r_{Pr_i}\right) = log\left(\alpha^{n-1}.(1-\alpha)\right) - log\left(\frac{1}{1-\alpha}\right)$$

$$log\left(\frac{W_n}{n}\right) = 2.\log(1-\alpha) + (n-1).\log(\alpha)$$

Y = C + X.m (Claeys and Van Steen, 2004).

2.3.1 Anderson-Schulz-Flory (ASF) model:

The way in which all the carbon containing products (hydrocarbons) are distributed in the products spectrum is normally predicted using the ASF model, as follows:

$$\frac{W_n}{n} = \alpha^{n-1}(1-\alpha)^2$$

In this case W_n represents the mass fraction of products which have n carbon atoms, α has the usual meaning (i.e. the measure of the likelihood of a molecule to continually grow producing long chain hydrocarbons). The nature and properties of the catalysts being used governs the magnitude of α. Conditions such as temperature and pressure also contributes to α. (Tau et al., 1990). Plotting the logarithm of the relative weight fraction, $\log(\frac{W_n}{n})$ against the number of carbon atoms in the molecule produces a linear relationship when α is not dependent on the number of carbon atoms. The value of (α) is usually equal to the gradient of the plotted straight line. Furthermore, the maximum selectivity of the different product classes that can be formed can be estimated by plotting the selectivity in mass or weight percent as a function of α. The change in the product weight fraction as the chain growth probability increases is shown in **Figure 2.2.** Increasing the chain growth probability turns to increase the average molecular weight of the product. In theory methane is the only product that can be formed and achieve 100 % product selectivity, and this happens when α, the chain growth probability equals zero. The distribution of the other products is shown, and it can be noted that only heavy paraffin wax can be produced in large proportions. The light liquid products (gasoline fraction) peaks at a maximum of 48% and for the diesel fraction, the maximum it can achieve is 40% product selectivity and this value is also dependent on the carbon number range being included in the product fraction.

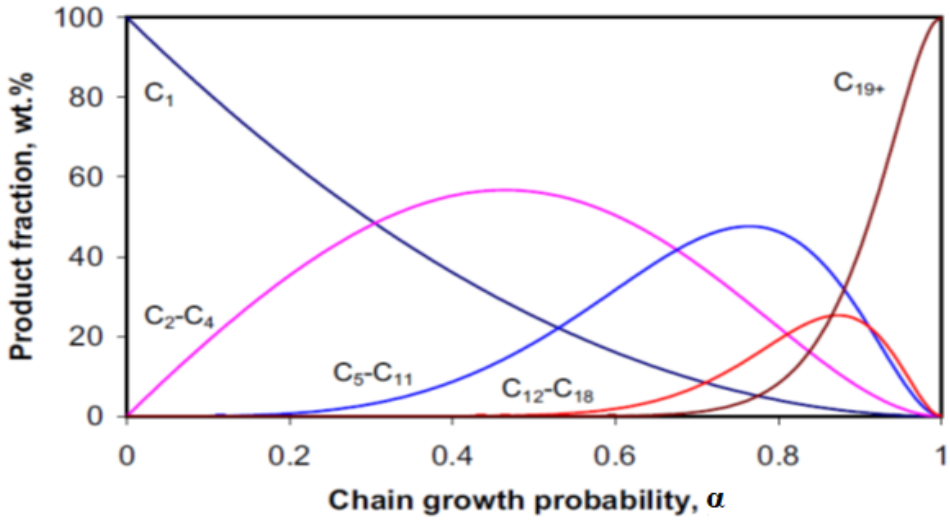

Figure 2. 2: Graphical representation of the predicted hydrocarbons product distribution plotted against α assuming ideal ASF kinetics. (Mbileni., 2006)

From the ASF distribution curves, a greater/maximum selectivity for gasoline and diesel fractions, is obtained when the growth probability factor is fairly large, typically greater than 0.5. This is favoured by good catalyst design and operating conditions. The Fischer-Tropsch synthesis product distribution is to a greater extent affected by the reaction conditions (i.e., pressure temperature, and the inlet H_2/CO-ratio) and the type of catalysts used. The extent to which the FTS product selectivity is affected by the process conditions selected for the process in shown in table 2.1 and it is observed that as the temperature increases the production of undesirable methane also increases. CH_4 selectivity is also affected by an increase in the H_2/CO ratio.

Table 2. 1: Influence of process conditions on Fischer-Tropsch synthesis product selectivity (adapted from Mabaso, 2005).

Parameter	Temperature	Pressure	H_2/CO ratio
Methane selectivity	↑	↓	↑
Olefin selectivity	~	~	↓
Oxygenate selectivity	↓	↑	↓
Chain growth	↓	↑	↓
Chain branching	↑	↓	~
Carbon deposition	↑	~	↓

↑ Increase with increasing parameter.

↓ Decrease with increasing parameter.

~ No clear effect

It can be observed from this table that if long chain hydrocarbons are to be produced, then low temperatures should be preferred as they favour chain growth. With low temperature ranges, chain growth probabilities of above 0.9 are possible. On the other hand, increase in pressure also has the effect of increasing growth probability factors. The hydrogen to CO ratio contributes immensely to the extent of Fischer – Tropsch activity that produces long chain hydrocarbons. High ratios usually have a direct impact on the amount of alkenes and oxygenated hydrocarbons that are produced. If the amount of hydrogen is high, quantities of olefins and oxygenates decrease considerably since hydrogen will promote full hydrogenation of these compounds to paraffins under reaction conditions.

2.3.2 Fischer-Tropsch operating regimes:

The Fischer-Tropsch process is typically composed of two operating regimes which are the high temperature Fischer-Tropsch (HTFT) and the low temperature (LTFT) process. The low temperature Fischer-Tropsch (220-250 °C) process is used in the synthesis of heavy hydrocarbons found in the boiling range of diesel to hard waxes (Dry, M.E;1982) while high temperature Fischer-Tropsch (320-350 °C) process produces lighter products including associated petroleum gas (APG), gasoline and chemicals (Steynberg et al., 2004, Mark E. Dry, 2004). Since LTFT mostly takes place in a slurry, the main mass transfer limitation encountered under this regime is due to the contact between the reactants and the liquid slurry phase. Thus, the HTFT is advantageous in this regard since interphase mass transfer effects are nearly negligible. **Table 2.2** below shows the typical product selectivities from operations at Sasol plants.

Table 2. 2: Hydrocarbon products selectivity from the two regimes (Jager and Espinoza, 1995).

Products (wt. %)	**LTFT**	**HTFT**
CH_4	4	7
C_2 to C_4 olefins	4	24
C_2 to C_4 paraffins	4	6
Gasoline	18	36
Middle distillate	19	12
Heavy oils/waxes	48	9
Oxygenates	3	6

There are two major types of products that are favoured by the Fischer – Tropsch reaction which are basically alkanes and alkenes. The type of catalyst and the H_2/CO ratio in the syngas employed (Weil and Lane, 1949) determines whether more of paraffins or olefins are produced. Paraffins formation is favoured by high hydrogen to carbon monoxide ratios and catalysts which have powerful hydrogenating abilities. On the other hand, olefins formation is favoured in cases where a less hydrogenating catalyst is used and when reactants with a low hydrogen to CO ratios are used. Water also forms part of the

primary products in addition to hydrocarbons that are mainly produced (Ning et al., 2006). Water accumulation in the reactor is undesirable in the Fischer Tropsch reaction since it affects hydrocarbon selectivity, syngas conversion, FT product distribution as well as catalyst longevity due to its deactivating effect on the catalyst. It does so by inhibiting the adsorption of syngas on the catalyst surface, thereby affecting the ability of hydrocarbons to start to grow, elongate and the subsequent full addition of hydrogen to produce saturated compounds (paraffins) or dehydrogenation to alkenes (Dalai and Davis, 2008). High water concentration is one factor that leads to oxidation and deactivation of iron carbides (Thüne et al., 2012, Pileni, 2003, Li et al., 2001, Shultz et al., 1955, Hayakawa et al., 2006, Bukur et al., 1995). Therefore, an understanding of the extent of water formation and desorption in the FTS reactor is an important aspect in optimizing FTS activity.

The water-gas-shift (WGS) reaction (eqn. R2.3) consumes CO and the water that would have been formed in the F-T reaction. This is converted to hydrogen and carbon dioxide. WGS activity is normally high over iron catalysts promoted with potassium and it is very low over cobalt or ruthenium catalysts. As a result, the WGS reaction is a very important one in the FTS as it helps to maintain the amount of H_2 in the syngas (Bukur et al., 2016, Mark E. Dry, 2002). This makes iron-based catalysts a better choice for GTL applications that uses coal-derived syngas for the FTS. Alcohols and other oxygenates such as carbonyl compounds and carboxylic acids are also produced during the Fischer Tropsch Synthesis (Yang et al., 2004). Iron catalysts favour the production of oxygenates especially when promoted with potassium (M. E. Dry and Hoogendoorn, 1981). They also stated that oxygenate formation increases with potassium content, but there is an optimized potassium content that must be used for an increased yield of oxygenates when iron based catalysts are being used (Yang et al., 2004, Teng et al., 2005). Dictor and Bell, 1986 and Bukur et al., 1990 reported that potassium has the effect of suppressing the production of only methanol but promotes the formation of longer chain alcohols.

2.4 Fischer-Tropsch catalysts:

The choice of catalyst to use in FTS is critical because the hydrocarbons distribution is governed by the type and characteristics of the catalyst being employed. The three key properties of an FT catalyst to be considered are its catalytic activity, stability and product selectivity, (Bukur et al., 2005, Bartholomew, 2001). At the time Franz Fisher and Hans Tropsch discovered the FTS process in 1923, an iron catalyst was used in the conversion of syngas ($CO + H_2$) to liquid fuels. Other catalytically active FTS catalysts which were later discovered include cobalt, nickel and ruthenium. Some have shown considerable effectiveness, but they have their own advantages and disadvantages in this process. Comparisons of the different properties for these metals are shown below in table 2.3. Comparison is based on the properties such as the price, FT activity, WGS activity and hydrogenation activity. Cobalt and iron-based catalysts are so far the only catalysts that are presently being used at an industrial scale as a result of some advantages they possess.

Table 2. 3: F-T active metal catalysts properties (F. Morales and Weckhuysen, 2006).

Active metal	Price	FT activity	WGS activity	Hydrogenation activity
Ni	++++	+	+/-	+++++
Fe	+	+	+++	+
Co	+++	+++	+/-	+++
Ru	+++++	+++++	+/-	+++

2.4.1 Price:

The price of the metal used to make FT catalysts contributes to the economic feasibility of the process. The following table shows the relative costs of the above transition metals that are widely used as catalysts in the Fischer-Tropsch synthesis.

Table 2. 4: Relative costs of FTS active metals (Van de Laan 1999; Dry, 2002).

Metal	Relative cost
Iron (Fe)	1
Nickel (Ni)	250
Cobalt (Co)	1000
Ruthenium (Ru)	31000
Rhodium (Rh)	570 000

From the table, it is apparent that the catalysts choice is influenced by these prices.

2.4.2 Fischer-Tropsch activity:

The catalytic activity of a metal is a measure of its ability to increase the conversion of reacting species into the desired products. In the case of the Fischer – Tropsch reaction, the catalyst activity is determined by the CO conversions which is usually determined over a reasonable time on stream. The catalysts activity is often governed by the surface properties of the catalysts sites and the level of adsorption of these species (methyl or CO). The variation of activity of the F-T active metals is shown in table 2.3 above and increases as we go down the group. Ruthenium is known to be the best performing catalysts for the Fischer – Tropsch process and can show considerable activity even at very low temperatures such as 150 ^{0}C (Morales and Weckhuysen, 2006). When selecting a catalyst to use for the process, it is important to choose one that promotes the production of long chain hydrocarbons since a metal that produces mainly methane is not economic to use for this very sensitive catalytic reaction.

2.4.3 WGS activity:

A lot of work has been done in assessing the was-gas shift activity of F-T active metals and iron has been singled out to the best catalyst that promotes the WGS activity. This reaction as shown in equation (R2.3) is considered essential in the Fischer – Tropsch reaction when feeding syngas with a low H_2/CO ratio. The reaction provides the much-needed hydrogen which promotes the formation of long-chain

hydrocarbons by its continued addition to the growing hydrocarbon chain. Hindermann et aI., 1993 reported that magnetite (Fe_3O_4) is the best iron oxide phase that promotes the WGS reaction and Dry, 1981 observed that iron carbides are the catalytically active phase to produce long-chain hydrocarbons. From these observations, it therefore implied that, a mixture of iron-based catalysts encompassing these two phases forms the best catalysts composition for processes meant to produce high-value hydrocarbon products. The other advantage will be that, even when using synthesis gas with a low H_2/CO ratio significant catalytic activity will be experienced.

2.4.4 Hydrogenation activity:

This is a measure of the ability of the metal to add hydrogen atoms on the inserted carbon atoms on the catalyst surface. Nickel displays high hydrogenating abilities in the Fischer Tropsch reaction, therefore it produces undesirably high methane selectivities. The reason being that, under reaction conditions, nickel produces carbonyls that are highly toxic (Enger and Holmen, 2012). The presence of these carbonyls can result in severe catalyst poisoning and hence a considerable loss of catalyst activity. The Fischer-Tropsch reaction becomes more economically viable when it produces long chain hydrocarbons or olefins which may later find their way into the market as valuable products. When using Nickel as a catalyst it becomes clear that you won't produce as much long chain hydrocarbons since methane selectivities as high as 50% can be achieved. It is because of these properties which nickel and other metals display that makes it imperative that we here discuss the properties of the most widely used Fischer – Tropsch catalysts. A review of each of these metals is therefore necessary.

2.4.5 Ruthenium as a Fischer Tropsch catalyst:

Ruthenium is believed to be the most active F-T catalyst which has the unbelievable ability of working at the lowest reaction temperatures. It does so with a higher selectivity to very high molecular weight products. Reactions done so far with this catalyst have produced long chain hydrocarbons at temperatures as low as 150 ^{0}C (Fernando Morales et al., 2007). The only drawback with the use of Ru is its price tag. It is too expensive to use as an F–T catalyst as its deposits worldwide are insufficient for large-scale commercial F–T operation. Ru is therefore not commonly used as FT catalysts and its use has only been limited to laboratory R & D research.

2.4.6 Cobalt as a Fischer Tropsch catalyst:

Bulk cobalt is mainly active in the metallic state during the F-T reaction. Usually it is either active as α-Co which is in the hexagonally closed packed (hcp) or the β-Co face centred cubic (fcc) form. For the smaller crystallites which are smaller than 20 nm in size, it is more stable in the (fcc) phase which is pure (Zhen Yan et al., 2009). In addition to that, (Schulz, 1999, Khodakov et al., 2007) also suggested that cobalt in the nanoparticle size range is active in the metallic phase. This means it is active in the

zero (0) oxidation state. The major advantage that is provided by cobalt as a Fischer – Tropsch catalyst is that, it produces mainly long chain hydrocarbons and is thus by far more catalytically active than iron – based F-T catalysts. It is also known to have a high ability to resist deactivation by carbon deposition or by water oxidation to form oxides. On the other hand, cobalt crystallites as F-T catalyst have their downside especially their price which is about 250 times that of iron catalysts. The WGS activity of cobalt catalysts is so little and thus it will not be highly recommended to use it for synthesis gas mixture with a low H_2/CO ratio.

2.4.7 Iron as a Fischer-Tropsch catalyst:

Iron has remained to be the catalyst of choice for many catalytic processes in industrial applications since it is relatively inexpensive. Iron catalysts are easy to prepare, and also tolerate harsh operating conditions, and they give a good turnover with a broad product spectrum (Ngantsoue-Hoc et al., 2002, Senzi Li et al., 2002, Motjope et al., 2002). Promotion of iron based catalysts using alkali metals such as sodium or potassium has now become a common practise and it is believed to enhance the production of more olefins and increase the average molecular weight of the products stream. It is also known to promote the water-gas-shift reaction (Dragomir B. Bukur et al., 1990). Copper which is known to improve the catalyst reducibility during activation is also often added to iron based F-T catalysts. To enhance the number of surface iron atoms available for interacting with the reactants, some silica or zinc oxide might also be added. This means that these materials improve the dispersion of the iron based catalysts. When iron is used as the active metal it promotes the reaction of CO and water in the water-gas-shift reaction as given in (equation R2.3) yielding more H_2 and carbon dioxide (Luo et al., 2009). The WGS activity favours the use of synthesis gas that has a low H_2/CO ratio. This particularly becomes useful when using coal derived syngas as it has a low H_2/CO ratio.

As previous mentioned, there are various iron phases that forms the catalysts mixture during and after catalyst activation. These include metallic iron, various iron carbides and oxides. Some researchers (Luo et al., 2009), have postulated that surface iron carbides are the active species in FTS but, this is a debatable area and hence remains controversial. Studies conducted by Schulz et al., investigating the behaviour of a Fe-Al-Cu/K_2O catalyst concluded that, the FT activity was linked to the formation of Hägg carbides (Fe_5C_2). These researchers also reported that metallic iron was less active. Iron in the metallic form is believed to rapidly change to these carbides (mainly Fe_5C_2) when reactants (syngas) are introduced. This was reported to occur mainly if prior hydrogen activation is performed (Dry and Hoogendoorn, 1981). It was therefore one of the objectives of this work to establish which iron phase is the most active in a slurry phase Fischer–Tropsch reaction setup. Catalysts were prepared using two separate methods for the iron oxide and the iron carbide respectively. Iron-based catalysts however have the challenge of quickly deactivating and hence resulting in a relatively short catalyst life-span. A closer look at these catalysts will give an in-depth knowledge on how to improve them.

2.5 Iron oxide phases

Iron – based Fischer – Tropsch catalysts may be present as different oxide phases (Yen et al., 2002) prior, during and post Fischer-Tropsch synthesis. These include haematite (α–Fe_2O_3), maghemite (γ-Fe_2O_3), magnetite (Fe_3O_4) and wüstite (FeO). It is these oxide phases that are believed to be active in the Fischer – Tropsch synthesis. As a result, it is therefore important at this juncture to have a brief look at the structure and chemistry of these phases. The arrangement of oxygen or hydroxide anions in the lattice of these structures is what differentiates them. Cations in the lattice occupy different positions relative to the anions layers. It is important to note that since the oxide and carbide phases of iron are the ones that are believed to be by far the most active phases (Shroff et al., 1995) in the FT reaction, an understanding of the crystallographic information and chemical properties of the iron oxides which take part in the Fischer-Tropsch synthesis is necessary. This information is shown in table 2.5 below. Some of the oxides have a face centred cubic lattice (fcc) while others have hexagonal close packing (hcp) crystallographic structures.

Table 2. 5: Crystallographic and chemical property information on the listed iron oxides.

Name of Oxide	Chemical Composition	Crystallographic System	Density (gcm^{-3})	Type of Magnetism
Haematite	α– Fe_2O_3	Hexagonal	5.26	Weakly ferromagnetic or anti – ferromagnetic
Maghemite	γ-Fe_2O_3	Cubic	4.87	Ferrimagnetic
Magnetite	Fe_3O_4	Cubic	5.18	Ferromagnetic
Wüstite	FeO	Cubic	5.90	Anti – ferromagnetic

The catalysts of interest, magnetite is formed during activation of Fe_2O_3 and is considered to be present and mostly active during the Fischer-Tropsch synthesis. Magnetite (Fe_3O_4) has a chemical formula of iron (II, III) oxide, which may also be written as FeO.Fe2O3, thus it is one part wüstite and the other part haematite (Tau et al., 1990). Magnetite is black or brownish black in colour. The crystal structure of magnetite is shown in Figure 2.4 below:

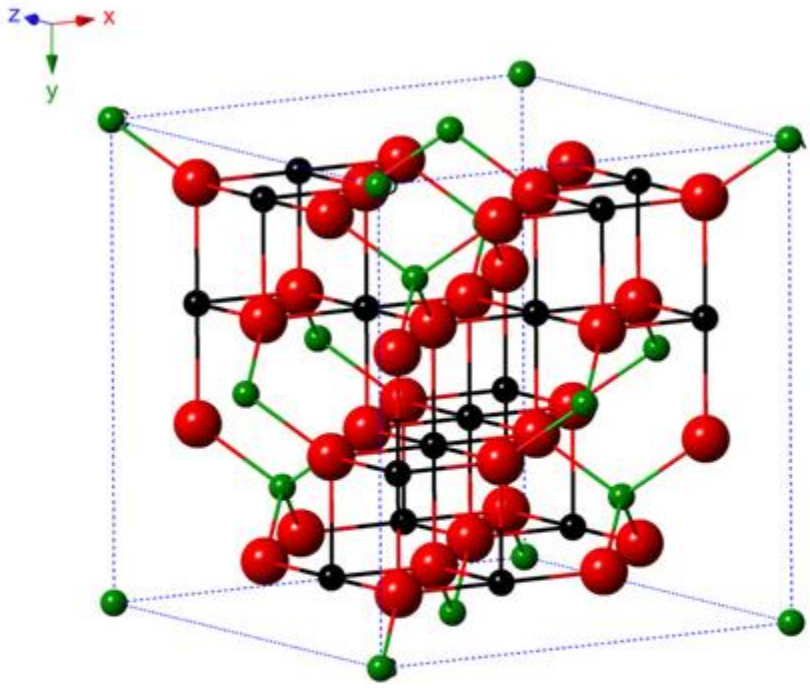

Figure 2. 3: Crystal structure of Cubic magnetite (Fe_3O_4), the black ball is Fe^{2+}, the green ball is Fe^{3+} and the red ball is O^{2-}, (Wu et al., 2015)

It is believed that during the activation stage and during the FTS process some of the magnetite and metallic iron phases that would have been formed are converted into various carbide phases which are also believed to be active in the Fischer – Tropsch Synthesis. These carbides come in different forms.

2.6 Iron carbides:

Iron carbides (Fe_xC) that are formed during FTS can be classified into stable TP-carbides which are those with carbon atoms in trigonal prismatic interstices and also O-carbides which are less stable and have carbon atoms in octahedral interstices (Wu et al., 2015, Wojciechowski, 1988, Komaya and Bell, 1994) as given in Table 2.4.

Table 2. 6: List of the different iron carbides formed during Fischer Tropsch synthesis.

		Formula	Structural name	Crystal lattice
Fe_xC	Trigonal Prismatic (TP) carbides	α– Fe_7C_3	Eckström – Adcock	Orthorhombic
		χ-Fe_5C_2	Hägg	Monoclinic
		θ-Fe_3C	cementite	Orthorhombic
	Hexagonal (O) carbides	ε-Fe_2C	Pseudo-hexagonal	Hexagonal to monoclinic
		έ-$Fe_{2.2}C$		Hexagonal

As previously discussed various researchers have reported their findings about the nature of the active phases under reaction conditions. Before the studies which were done in 2006 by Ning et al. (2006) as

well as Herranz et al., (2006), there were ongoing studies and previous studies which were reporting conflicting standpoints concerning iron-based Fisher–Tropsch catalysts. In 1986, Dictor and Bell reported that it was essentially a mixture of χ- and ε-carbides which constitute the active phase under reaction conditions. They did arrive at this conclusion when Zhang and Schrader in the previous year, 1985, had concluded that it was ideally a mixture of both oxides (mainly Fe_3O_4) and iron carbides. The other aspect which these researchers were not in agreement upon were the catalysts sizes that were being used and the way their preparation was done. Some were using micron-sized catalysts and some nanosized crystallites. It is therefore essential to note that the type of catalysts and the phases that will consequently be produced are determined by the type of catalyst preparation method that would have been used. Extensive work has been done to this day in search of facile ways of producing the right catalysts for research and hence commercial application. A review of the most commonly used methods is presented here.

2.7 Catalyst preparation methods:

Commercially, the preparation of iron catalysts varies depending on the process temperatures at which the catalyst will be operated. Low temperature Fischer-Tropsch catalysts are prepared by precipitation or co-precipitation while catalysts utilised in HTFT synthesis are prepared by fusing magnetite together with promoters (Dry M.E, 2002). Catalysts preparation techniques can assist in gaining new insights and give way to new and improved catalyst development of existing syntheses.

Heterogeneous catalysts being used in industrial processes today can be classified into three common classes (Gallei et al., 2008) :

- Carrier free: These are those catalysts that have no additional support material or chemicals that alter their activity or chemical or physical make-up. It contains the active catalyst only for example the case of pure magnetite.
- Supported catalysts: These have physical material that are added to them for example silica and alumina which are common support materials. The support material usually increases the dispersion of the catalysts and is particularly used for expensive catalysts such as cobalt. There are specialized techniques that are used to achieve this.
- Coated catalysts: This is almost similar to supported catalysts but in this case a carefully applied coat which is usually very thin is sprayed on top of an inert support material. It is usually used to catalyze reactions that are kinetically fast.

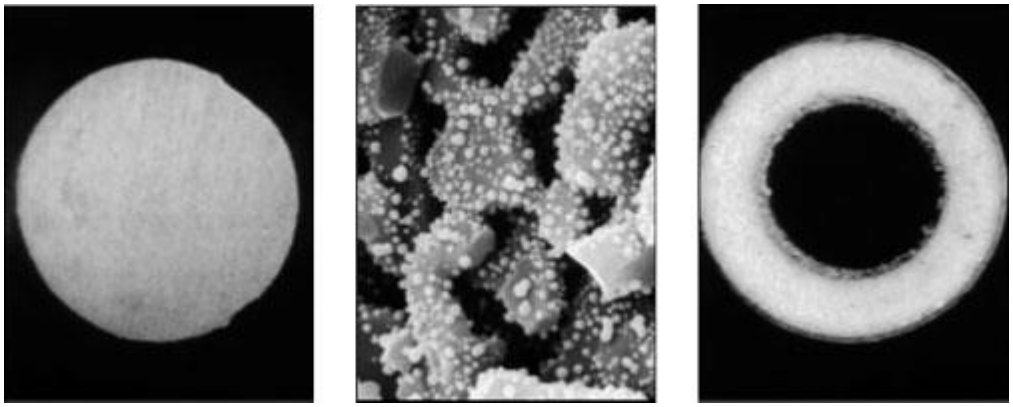

Carrier-free catalyst Supported catalyst Coated catalyst

Figure 2. 4: Types of heterogeneous catalyst, (Gallei et al., 2008).

Several breakthroughs have been recorded with regards to the preparation of various nanoparticles for use as catalysts in both academia and industry. But what is important to note is that, most of these catalysts preparation techniques which have been proposed, have limitations when it comes to the yield of catalysts that are produced. Most of them can produce samples that are only enough for laboratory testing and hence a major drawback for industrial scale catalysts consumers. It is very important that during the synthesis, proper control of nucleation and growth of nanocatalysts should be achieved since the chemical and physical properties of most of the nanocatalysts are size and morphology/shape dependent (Henglein, 1989, Alivisatos, 1996, Burda et al., 2005). It is also of concern that some of the methods that have been developed for catalysts synthesis make use of very expensive precursors and surfactants which in turn affect the activity of the catalysts. This has since initiated more research to be done in the field of designing robust catalysts for both fundamental and industrial use.

For example in the precipitation method, the catalyst precursor of the active metal is dissolved in a solvent such as water, and thereafter, precipitated on the support (Geus and Van Dillen, 2008). This precipitation step is achieved when there is a change in the solution pH. The pH adjustment can either be forced to happen when the support material is already in the solution as a solid or it can be formed via a simultaneous precipitation with the corresponding precursor or metal salt (co-precipitation). After drying and calcination, the oxidic catalyst precursors are obtained. The advantages of the precipitation method as compared to other techniques are that:

- the composition obtained is homogenous,
- the crystallite size distribution is typically much narrower; and
- it is possible to synthesize catalysts which have a high metal loading on the support in one single preparation step (Reuel and Bartholomew, 1984a, Reuel and Bartholomew, 1984b, Nijs and Jacobs, 1980).

2.7.1 Conventional preparation techniques for iron oxide catalysts:

The preparation methods for iron oxide nanocatalysts are essential in determining the nanoparticles' crystallite size, particle size distribution, morphology, magnetic characteristics and surface functionality. Many methods have been developed but it is impossible to list all these methods here. As a result, only a limited number of approaches are discussed including co-precipitation, impregnation, hydrothermal synthesis, micro-emulsion, sonochemical and solvothermal synthesis techniques. The advantages and disadvantages of each preparation technique are going to explored and why it was not or chosen for this work.

2.7.1.1 Precipitation and co-precipitation:

Precipitation has been used for a long time in the preparation of catalysts for wide applications. It is the simplest method of making heterogeneous catalysts for use in both industrial and academic setups. The process requires a solution of the metal precursor as homogeneously mixed ions and a precipitating agent (Schüth, F., et al, 2008; Geus J.W., 1993**)** such as a base which is required to force the precipitation of the ions out of the solution by altering the pH of the solution. This implies that even in situations where bimetallic catalysts are required, this process can be used successfully to produce a homogenous solid mixture of the bimetallic catalysts. Catalysts such as aluminium oxide, titanium dioxide, and iron III oxide are industrially prepared using precipitation (Hooff, 1993). Control of the nucleation and growth of the nanoparticles when using co-precipitation or even precipitation is very difficult and in most cases the particle size distribution range of the produced nanoparticles is wide (Twigg, 1989). During the precipitation process, particles are usually precipitated in the form of amorphous hydroxide and sometimes carbonates. These have to be then transformed into the corresponding metal oxides after drying and calcination. Since the sizes of the particles that are produced using this process is not within the required size range of particles needed for this work, it was considered not suitable for this application.

2.7.1.2 Co-precipitation:

Co-precipitation is considered a better alternative in synthesising magnetite nanocatalysts because it produces particles with a relatively narrow particle size range and in large quantities. The process requires an equimolar (1:1) mixture of the two iron ions in a homogenous solution and a precipitating agent. Ammonia is used as the precipitating agent for this process. Two methods are popular for this preparation. The first one being the Massart method and the second one is the titration hydrolysis technique (Kang et al., 1996). Titration hydrolysis involves the careful addition of the equimolar solution containing the ferric and ferrous ions to the alkaline ammonia solution. On the other hand, the Massart method which was developed by Massart (Massart, 1981) involves the addition of the alkaline solution into the solution to be precipitated. The magnetite nanoparticles that are produced are reported to be completely precipitated within the 8-14 pH range. It is known that the size and morphology of the

particles that are produced is determined by the nature of the salt used. For example, it is known that the particle size and hence size distribution of particles produced using iron sulphate is different from the one that is produced using the chloride or nitrate salts. The size and shape of the particles is also known to be dictated by the ionic strength and pH of the medium (Yang et al., 2004, Arakawa and Bell, 1983) and also the type of capping agent used. Co-precipitation is known to produce smaller nanoparticles even without the use of surfactants and that is an advantage over ordinary precipitation. When the pH is not properly tuned, the magnetite nanoparticles can be oxidised into hematite (α-Fe_2O_3) or iron hydroxide $Fe(OH)_3$ or to maghemite (γ-Fe_2O_3) as depicted in Figure 2.5 below (Yamaura et al., 2004). The only disadvantage of this method is that careful elimination of oxygen and pH control are important in this preparation. Also, for proper size control, surfactants should be added but these will cause problems later.

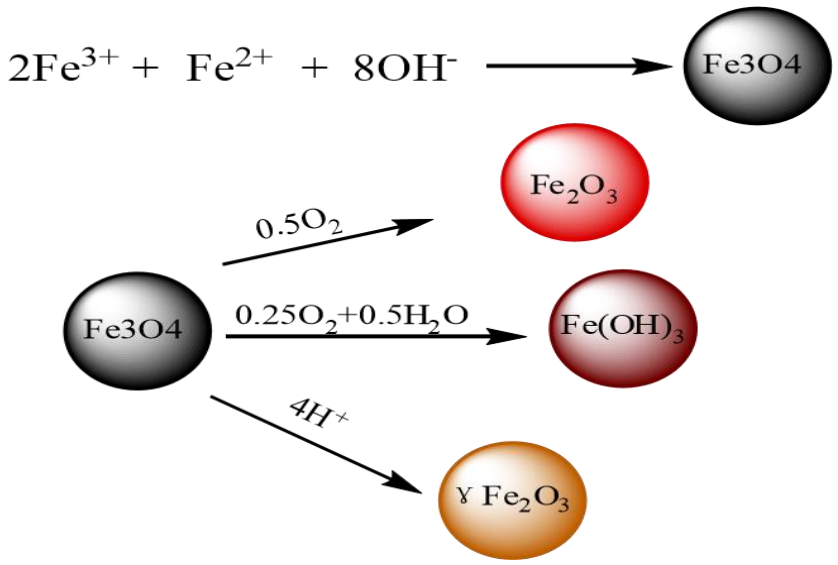

Figure 2. 5: Magnetite catalysts preparation and possible side reactions (Xue-Mei et al., 2011).

It has been shown that the pH of the alkaline solution affects the size of the nanoparticles (D. K. Kim et al., 2001) in that decreasing pH from 14 to 11.54 led to larger particles from 3 to 6 nm. The temperature of the solution where the particles are being precipitated affects the nanocrystallites size since a higher temperature results in the production of larger particles (Do Kyung Kim et al., 2003).

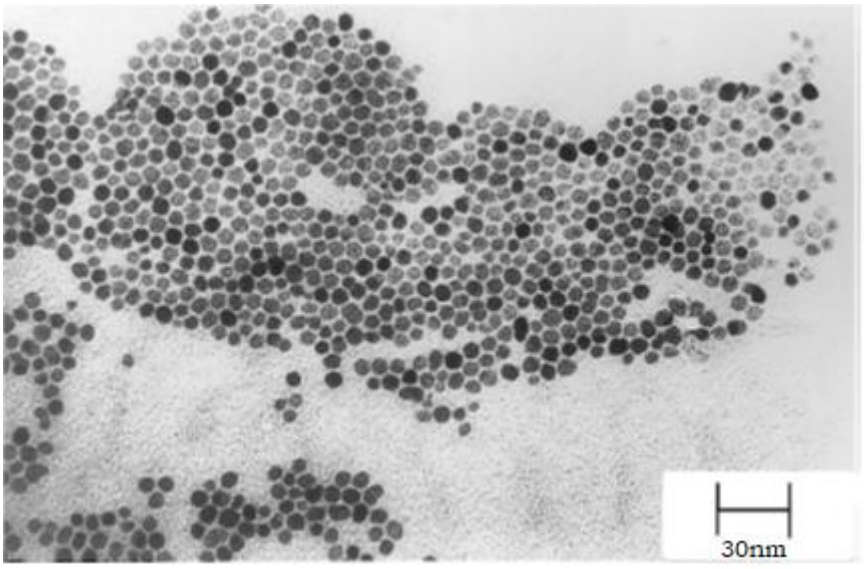

Figure 2. 6: Scanning electron micrograph of Fe_3O_4 particles prepared by co-precipitation technique (Kang et al., 1996).

The size distribution in co-precipitation is relatively broad because in the precipitation process, nucleation and particle growth are both present and in competition. Nevertheless, co-precipitation has the potential to produce particles at large scale and hence it is used for the synthesis of catalysts for industrial applications. For this work, the co-precipitation method was not selected for use.

2.7.1.3 The impregnation technique:

For the preparation of supported metal catalysts, the impregnation technique is the best option. It's the most favourable when preparing catalysts which are made from very expensive precursors such as cobalt based F-T catalysts. The process requires a solution that contains the metal precursor and this is either added onto the support (Bartholomew, 1990) using one of the three ways which are used to fix the metal crystallites onto the support (J.W. Geus, 1993, Marceau et al., 2008). It can be applied using capillary impregnation which is used to load the catalytic active metals onto the dry support material (Marceau et al., 2008). The support material usually has some pores which takes up the solution which will then be subsequently evaporated later leaving the crystallites distributed on the support. When the volume of solvent required to be absorbed by the support is exactly the same as the total volume of the available pores on the support, incipient wetness impregnation results (Mccullen, 1990). It is a subtype of capillary impregnation, but it has this distinguishing feature that the volumes should exactly match each other. The main challenges which are experienced with these two kinds of impregnation techniques are the issue of exothermic processes and the build-up of internal pressures due to internal reactions in the pores. These processes might result in the shape distortion of the support material structure and hence affecting catalysts loading and distribution. To avoid these problems, diffusional impregnation (Marceau et al., 2008) is employed and this involves a situation where the support material is dipped

into the solution containing the metal precursors which it has a pure solvent already loaded into its pores. This means that the metal precursor ions will then diffuse into the pores and this avoid the pressure build-ups. The only disadvantage of this method is that it is slow. Overall, the impregnation technique suffers drawbacks such as compromised catalysts loading onto support, low dispersion and difficulties in controlling the particle size distribution (Marceau et al., 2008). Therefore, for this work, impregnation technique was not suitable for the synthesis of nanocatalysts.

2.7.1.4 Hydrothermal Synthesis:

In search for better ways of synthesising nanosized crystallites, researchers use the hydrothermal synthesis which makes use of water as a cheaper solvent. In this technique the preparation is however done using high pressures and high temperatures (Fan et al., 2001). The iron-based nanocrystals that are produced are usually from a single iron precursor and not equimolar mixtures like in co-precipitation.

In general, in a hydrothermal synthesis, relatively larger particles are yielded compared to co-precipitation. For example, Zhong Jie Zhang et al., 2008b reported the preparation of magnetic iron oxide nanoparticles from $FeSO_4 \cdot 7H_2O$ by hydrothermal synthesis using polyvinyl pyrrolidone (PVP) as the surfactant. Nanoparticles with an average diameter of 80 nm were obtained. The nanoparticles showed ferromagnetic behaviour with a remnant magnetization of 12.5 emu/g owing to their large particle size.

On the other hand, it has been reported that nanoparticle size control via the control of the reaction temperature at such higher temperatures yielded larger particles (Jun Wang et al., 2003). It should be noted that particles prepared under these conditions showed ferromagnetic behaviour in contrast to their high degree of crystallinity (D. Chen and Xu, 1998).

Overall, hydrothermal synthesis can yield particles with high crystallinity and controlled morphology, but the nanoparticles thus prepared are bigger in particle diameter in contrast to co-precipitation. These larger magnetic nanoparticles especially with diameters greater than 50 nm may display ferromagnetic behaviour instead of super-paramagnetic behaviour, which is a problem if you wish to separate the catalysts using magnetic separation in slurry phase Fischer-Tropsch process.

2.7.1.5 The Micro-emulsion technique:

Preparation of magnetic iron based catalysts by the micro-emulsion method is aimed at producing nanoparticles that are almost of the same size. This implies that it is a technique that results in the production of particles which can be easily dispersed owing to their good morphology and ability to resist particle agglomeration (Y. Deng et al., 2003, Pillai et al., 1995, Zhou et al., 2001). Micro-emulsions make use of a mixture of solvents like water, a surfactant and a co-surfactant in their makeup.

Thus, it utilises the immiscibility of two solvents in the presence of a surfactant. Particles of various size and morphology have been prepared including spheres, needle-shapes, cubes and hollow spheres.

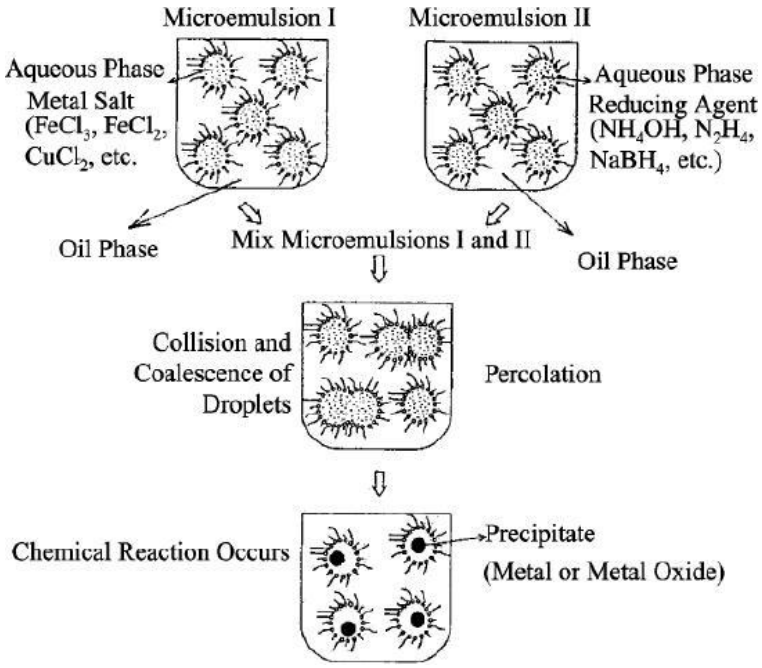

Figure 2. 7: Reaction steps for the formation of metal particles via the micro-emulsion techniques, adapted from Eriksson et al., (2004).

Micro-emulsion can be used to control the size of the nanocrystals by adjusting the oil/water ratio. Moreover, the morphology of the resulting particles can be tuned by controlling the pH of the reaction mixture. For example, Zhou et al., (2012) used an oil-in-water emulsion to prepare nanocatalysts using cyclohexane as the oil phase. They used this in conjunction with the two surfactants, NP5 (polyoxyethylene isooctyl ether phosphate) and NP9 (nonoxynol-9 phosphate). Iron sulphate and iron nitrate were the aqueous precursors. They found needle-like particles at pH = 8.5, a combination of needle-like rods and the perfectly spherical particles at pH = 10.5, and spherical particles at pH = 13.5. This can be related to the shape of the micelle change with pH value of the medium.

Besides needles and rods, hollow spheres (Zhang et al., 2008) have been reported. The hollow microspheres were ferromagnetic, instead of super-paramagnetic. In a micro-emulsion approach, a principal advantage is that the nanoparticle size can be modulated by controlling the aqueous phase. By proper control of the conditions, various morphologies can be obtained. Care must however be observed to ensure that the magnetic properties do not change with the morphology. The disadvantage of this methods lies with the issue of using many surfactants which are usually expensive and often stick to the catalysts particles (Pinna et al., 2011) which will in turn reduce their activity in the Fischer Tropsch synthesis.

2.7.1.6 Sonochemical Synthesis:

The use of ultrasonic agitation in catalysts syntheses involves cavitation bubbles that are formed when a liquid is irradiated by ultrasound and in the process promoting the occurrence of chemical reactions. These reactions such as reduction, hydrolysis and oxidation under the initiation of ultrasound is what is known as sonochemistry (Suslick and Price, 1999). Accordingly, ultrasonic frequency, sonication duration, and reaction temperature (Gedanken, 2004, Abu Mukh-Qasem and Gedanken, 2005) are important parameters in controlling the particle size, morphology and eventually their magnetic behaviour.

Figure 2. 8: Experimental setup for ultrasonic agitation required in sonochemical synthesis of iron oxide catalysts (Fischer Scientific).

For instance, Vijayakumar et al. (2000) managed to synthesise iron oxide nanocatalysts sonochemically which had a mean particle diameter of 10 nm. A high-intensity ultrasonic horn (20 kHz) was used for these experiments to irradiate iron (II) acetate which was in de-oxygenated water at a pressure of 1.5 bar and temperature of 298K. The Fe_3O_4 nanoparticles formation mechanism was proposed as that water molecules turned into hydrogen peroxide upon the absorption of ultrasound which oxidized Fe(II) leading to magnetic nanoparticle formation (Zhu et al., 2005). It was also reported that MFe_2O_4 (M = Fe, Zn) nanocrystals were prepared sonochemically in an aqueous solution of $FeCl_2$/urea (or $ZnCl_2$/$FeCl_2$/urea). The final product was Fe_3O_4 and $ZnFe_2O_4$ and were 15-20 nm and 20-50 nm in diameter respectively. The drawback for this technique for this work is in the quantity of nanocatalysts that can be produced. The process has not yet reached commercial production levels. Particle size control is also very difficult as particles might assume different particle sizes and shapes. It however reduces particle agglomeration to the extent that it will be highly recommended if it can be used in conjunction with the precipitation or co-precipitation techniques (Hexing Li et al., 2007).

2.8 Remarks:

From the review of the catalysts synthesis techniques that have so far been discussed in this work, a lot of work has been done in finding the best solution to produce good nanocatalysts particles. Avenues that involve the use of solution routes have been widely investigated and they seem to have the potential to produce catalysts for commercialisation, but they have their own drawbacks. One of the earliest method to be discovered in the synthesis of nanoparticles is the reverse micelle technique (Pileni, 2003) which gives the developers the ability to properly and closely monitor particle size growth. The ideal nanocatalysts required by both academia and industry are those which are highly crystalline, dispersible, good particle morphology, correct particle size and size distribution(Pileni, 2001). In the case of slurry phase processes such as the Fischer – Tropsch reaction, particles should preferably be highly magnetic to allow for easy separation.

In order to fulfil these requirements, solution routes massively make use of surfactants in order to strike a balance between particle nucleation and particle size growth (Jun et al., 2006). Most of these surfactants are however very expensive and toxic to the environment and therefore don't live up to sustainable environmental standards. As-synthesised catalysts will also be coated with these huge organic molecules and hence blocking catalysts sites. These are some of the reasons why these methods are limited and cannot be used for large scale industrial applications and hence the need for better synthesis techniques.

Considerations have also been made for the possible use of traditional sol-gel chemistry, but they tend to produce more of amorphous particles (Matijevic, 1993, Livage et al., 1988, Cushing et al., 2004) which require further heat treatment to convert them into crystalline particles and hence a big challenge. This further step will compromise the particle size distribution as it results in particle agglomeration. To avoid the use of huge organic molecules (ligands) in catalysts synthesis, recent methods have been devised to use the solvent to also act as a ligand in controlling particle size growth.

Niederberger et al., 2005 proposed a method of synthesising iron oxide nanoparticles using benzyl alcohol as an environmentally clean way of producing highly magnetic ad cystalline nanoparticles without the use of additional ligands (Niederberger et al., 2005, Niederberger et al., 2006). The technique which is solvothermal in nature is known to be envrionmentally friendly since the solvent is non toxic and is capable of acting as both a base solvent and a ligand (Niederberger et al., 2006). It was discovered as well that the route offered highly reproducible results in terms of particle size distribution since there is close control of both the growth and nucleation of nanoparticles during synthesis. The only challenge that was discovered with this approach was the issue of particle redispersion but for the case of the slurry phase Fischer – Tropsch synthesis, it is not necessary since particles are readily redispersed when they are loaded into the reactor. No functionalization is required since particles only require activation by exposing them to a reducing atmosphere of either hydrogen, CO or syngas.

2.8.1 Solvothermal Synthesis:

This is a technique that is in many respects analogous to the hydrothermal method of catalysts synthesis. The only difference is that it makes use of organic solvents as opposed to water which is used by the hydrothermal synthesis. The method usually achieves high catalysts reproducibility and particle size control even at atmospheric pressure which is different from hydrothermal synthesis which makes use of high pressure autoclaves. The use of organic solvents brought some more advantages (Parkinson, 1995) since more catalysts options which were impossible to synthesise using water in the hydrothermal synthesis were now easily being prepared. For example catalysts mixture containing both iron and copper (Hyeon et al., 2001) were now easy to synthesize and since copper helps in the reducibility of iron catalysts during activation, this was a further advance in material syntheses.

The selection of the best conditions necessary for the production of the desirable catalysts particles is very important and it begins with the proper choice of the temperature to use during the synthesis as well as the residence time in the reactor. A suitable solvent is also necessary as solvents exert varying size control mechanisms during catalysts synthesis. Benzyl alcohol (BA) and iron (III) acetyl acetonate as the iron source were found to be ideal precursor and solvent for the solvothermal synthesis of magnetite nanocatalysts since it produces highly magnetic and crystalline nanoparticles (Pinna et al., 2005). It is also good at tuning the particle sizes of the nanoparticles yielding reasonable amounts of very clean (pure) and well dispersible nano-crystalline powders with size ranges of 8 – 25 nm. In the laboratory, autoclaves with a PTFE (Teflon) cup are often used to synthesize these highly pure nanocatalysts.

Figure 2. 9: Bench scale stainless steel autoclave with a PTFE cup used in the synthesis of magnetite nanocatalysts.

Solvothermal synthesis has shown great advantages in tuning the shape of the nanoparticles. For example, (Jana et al., 2004) studied the synthesis magnetic iron oxide dots and cubes using the pyrolysis of iron oleate at 300^{o}C using 1-octadecene as the solvent. Results showed that the particle size and morphology are dependent on the excess of oleic acid and reaction duration. This technique has been extended to the synthesis of various magnetic nanoparticles including Cr_2O_3, MnO, Co_3O_4, and NiO.

Hollow particles (Leyu Wang et al., 2006) have also been prepared by dissolving $FeCl_3 \cdot 6H_2O$ in ethylene glycol in the presence of anhydrous sodium acetate and 1,6-hexadiamine followed by heating to 200^{o}C for 6 h in an autoclave. It was suggested the hollow spheres consisted of agglomeration of single crystals of much smaller size. The size of the nanocrystals can be controlled by reaction time (Hong Deng et al., 2005), starting concentration of the reactants, and protective reagents (Aiguo Yan et al., 2008) similarly to hydrothermal synthesis.

Besides size and morphology control, solvothermal synthesis shows advantages in yielding hydrophobic particles directly, which is not possible by co-precipitation. Sun and Zeng (2002) studied the use of iron acetyl acetonate, $Fe(acac)_3$ in the synthesis of magnetite nanoparticles in which they added alcohol, oleylamine and oleic acid by refluxing at 265^{o}C. These nanoparticles are soluble in nonpolar solvent. Their further studies (Sun et al., 2004) gave insights to the effect that the method can be used in the synthesis of other nanoparticles such as MFe_2O_4 (M = Fe, Co, Mn).

Overall, in solvothermal syntheses, nanoparticles with larger diameters are a result of prolonged reaction time, which is due to particle growth during prolonged incubation. To counter such effects, the addition of small amounts of surfactants helps to reduce particle size because surfactant can prevent the growth of small-sized nanoparticles by adsorbing on their surface. The advantages presented by this method resulted in it being selected to be the catalysts preparation method for this work.

2.8.2 Synthesis of iron carbide by the biopolymer route:

The synthesis of iron carbides is not straightforward since most of the discussed techniques have failed to produce metal carbides. The traditional way of synthesizing iron carbide nanoparticles for use in industry or laboratory testing for Fischer Tropsch synthesis has been to synthesise them in-situ. The procedure usually involves exposing iron oxide crystallites to a high temperature and simultaneously introduce a reducing stream of carbon monoxide. The result is mixture of various iron carbide and oxide phases in different proportions. The problem with this method is that, it is difficult to easily distinguish which phase was active during the reaction and proper fine-tuning of the particle size and size distribution of particles is also a challenge. Particles tend to grow due to agglomeration during the carburization process and this will result in the formation of bigger crystallites and reduce the surface area available for reaction. In-situ synthesis of iron carbide materials, for example Fe_3C nanoparticles presents a considerable challenge.

Biopolymers have recently gained popularity in the synthesis of nanoparticles due to their capability to control the particle size growth in many catalysts syntheses. They have since became so useful, particularly in the preparation of metal carbide nanoparticles which are usually difficult to synthesise using the traditional catalysts preparation techniques such as precipitation and impregnation. Fe_3C is such an example of a carbide (Nikitenko et al., 2004) that is difficult to synthesize in its phase pure state but the use of biopolymers has made this possible. Gelatin, ammonium alginate and chitosan are some of the biopolymers that have found widespread acceptance in the preparation of such nanoparticles. They control particle size growth due to the formation of a network of fibres that surrounds the growing particles as shown in figure 2.10 below:

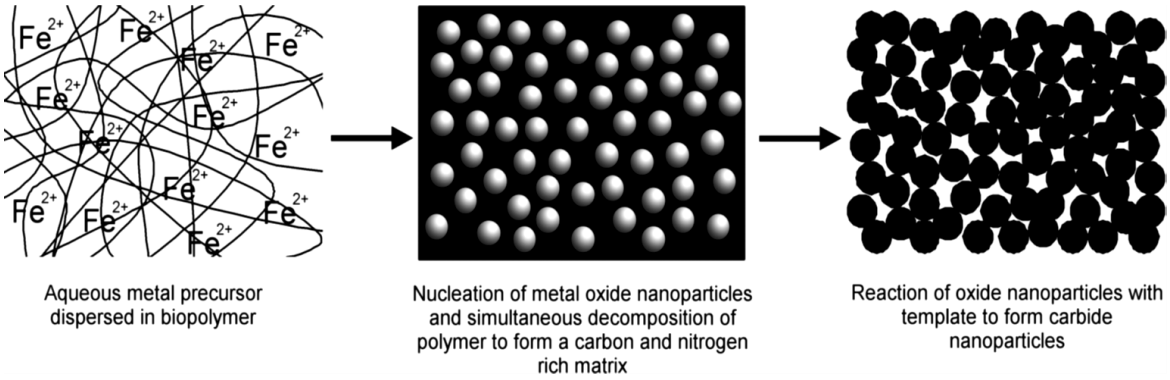

Figure 2. 10: Formation of Fe_3C nanoparticles from a biopolymer gel precursor (Schnepp et al., 2010).

Biopolymers are usually made into a solution first before the addition of a solution of metal precursors which will later be turned to metal carbides and the biopolymer will be the carbon source during the calcination stage. The biopolymer solution will therefore help in the uniform dispersion of the metal precursors in the solution as well as controlling the growth of the particles. The biopolymer also influences the shape of the nanoparticles (Fe_3C). The proved viability of preparing phase pure iron carbide nanocatalysts using this method, resulted in it being selected for the preparation of iron carbides for this work. These crystallites synthesised using this method have never been tested for their performance in Fischer-Tropsch synthesis. This was their first testing, achieved using a slurry phase reactor. After a crystalline sample of the required catalysts is prepared and isolated from the solution, catalysts undergo an activation stage. This makes it assume a crystallite phase that can readily catalyse the desired reaction. For the Fischer Tropsch reaction, the following activation stages are required.

2.9 Catalyst activation:

The term “activation” refers to the transformation of an inert catalyst precursor into a composition and structure that facilitates the reaction between hydrogen and carbon monoxide to take place and produce hydrocarbons. Catalysts activation takes place soon after the synthesis of the catalysts. It is basically a step that prepares the catalysts for use in the reaction. This does not necessarily mean that all catalysts

are supposed to be activated but it is a necessary step in F-T reactions since it has proved to be the best way if high product yields are to be realised. It also serves to inform us about the nature of the active phases under reaction conditions. Activation steps for FTS catalysts consist of drying, calcination and reduction (Adesina, 1996).

2.9.1 Drying:

Drying commences with the evaporation of solvent from within the catalyst support's pores if the catalysts are supported (Perego and Villa, 1997). The initial drying stages are driven by evaporative forces which take place at near to normal temperatures up to about 200°C (Sewell et al., 1996). This happens until the moisture drops down to about 50% and in this drying region, capillary driving forces are responsible for the drying process. It is at this stage that the drying of the catalysts must be properly controlled since this is when metal crystallites start to form on the support surface. If not well controlled, uneven crystallite dispersion will result (Perego and Villa, 1997).

Studies were done to compare the drying process of supported cobalt catalysts so as to ascertain the method that yields better dispersed nanocatalysts on the support material (Rosynek and Polansky, 1991). Use was made of vacuum drying technology and normal oven drying and it was observed that the catalysts that were vacuum dried were evenly dispersed as compared to the oven dried catalysts. The anomaly was explained in terms of the formation of a concentration gradient that arises in air drying hence distorting the even distribution of the nanoparticles on the catalysts support. These studies concluded that it is advisable to use vacuum drying instead of air/oven drying before catalysts calcination so as to promote even active catalysts dispersion.

2.9.2 Calcination:

Calcination is among the final stages in some catalysts activation processes and it results in the formation of the active phase that will be present for the few first hours or minutes in the reaction media depending on the stability of the catalysts. This stage involves exposing the catalysts particles to high temperatures which are higher than drying temperatures. Temperatures as high as 650°C can be utilised depending on the recommended procedure. It is important that the calcination procedure be done properly since and changes in the required conditions will result in a totally different phase. Calcination is usually associated with the decomposition of the material to form a totally different substance with the evolution of gaseous products such as CO_2 or chemically bonded water. In some instances, the process is carried out in an inert environment to prevent unwanted aerial oxidation of the samples. This is particularly true in the synthesis of cementite, (Fe_3C) using the biopolymer route. During calcination, particles tend to grow as they agglomerate and therefore the need to closely monitor the calcination step to avoid undesirable particle size distributions. This phenomenon can also be observed with cobalt based Fischer – Tropsch catalysts as reported by (Coulter and Sault, 1995).

2.9.3 Reduction:

This is mainly achieved using either carbon monoxide or hydrogen as the reducing agent. In the Fischer – Tropsch reaction the catalysts are usually reduced in order to bring the catalytically active metal to the correct phase. In most instances, the process is carried out in-situ and the F-T synthesis commences soon after the process is completed. The reduction stage usually converts the catalyst into its metallic phase as shown in the following reaction:

$$MxOy(s) + H_2(g) \sim M(s) + H_2O(g)$$

With iron-based catalysts, the catalysts are reduced to the metallic phase through several stages. When the initial phase is magnetite (Fe_3O_4), the catalysts will be reduced to wüstite (FeO) and subsequently into the metallic iron (van Steen, 1993). To enhance catalysts reducibility, some noble metals such as copper are added to the catalysts as promoters. The importance of reducibility lies with the fact that, it makes it easier to adjust catalysts so that they are turned to be in the required active phase. The more the reduction time when dealing with iron based catalysts, the bigger the particle sizes (Zsoldos et al., 1996) and the reverse is true for shorter reduction times.

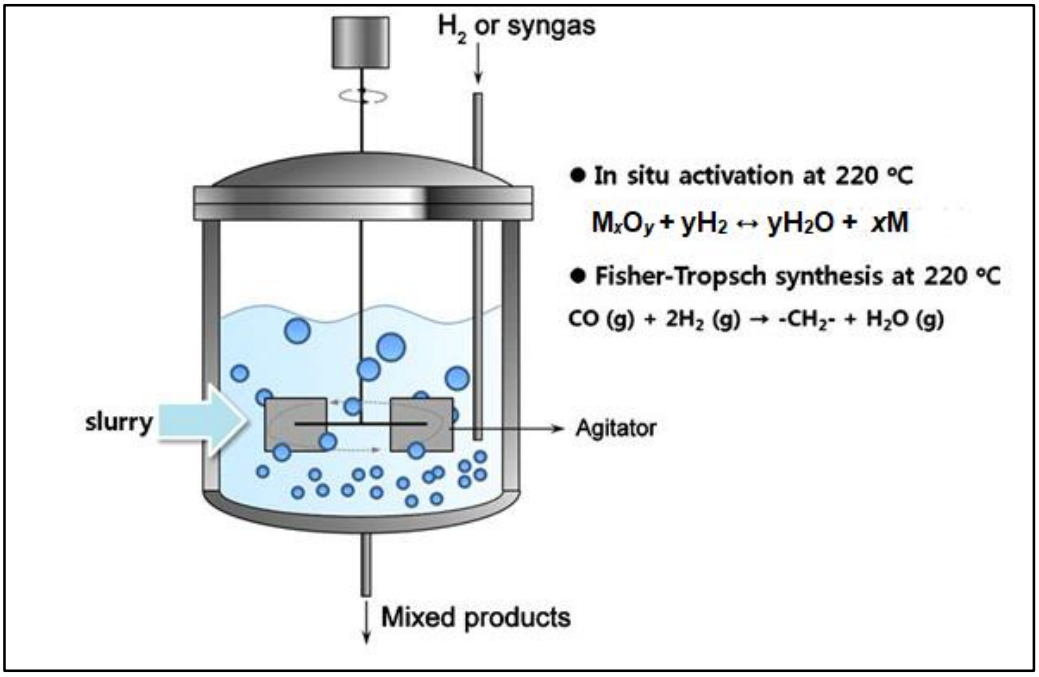

Figure 2. 11: In-situ catalysts activation setup using reducing gases prior to Fischer Tropsch setup for ultrasonic agitation required in sonochemical synthesis of iron oxide catalysts.

2.10 Activation procedure for iron catalysts:

The use of hydrogen (H_2), carbon monoxide (CO) and synthesis gas (H_2/CO) as activation gases has been well documented in the open literature (Senzi Li et al., 2002, Burtron H. Davis, 2003, Dragomir B. Bukur et al., 1999, Hao et al., 2007, Herranz et al., 2006). The phase transformation of Fe_2O_3 during

H_2 activation is shown in Figure 2.11. Catalyst activation in FTS is done by reducing the catalysts with either H_2 (eqn. R2.6), CO (eqn. R2.7) or syngas. As previously mentioned, cobalt catalyst is usually activated with hydrogen and the produced Co^0 is reported to be the active phase in the Fischer – Tropsch reaction. It is believed (Hao et al., 2007) that the type of activation gas selected usually affects the catalytic performance of iron based catalysts. It has been reported that when using unsupported ion-based catalysts, their activity is much lower if hydrogen gas is used than when CO is used as the activation gas. These catalysts have even superior performance to synthesis gas reduced catalysts (Dragomir B. Bukur et al., 1999).

Studies conducted on the reduction of Fe_2O_3 showed that it occurs in a two-step reduction process via Fe_3O_4; the first reduction step corresponds to $Fe_2O_3 \rightarrow Fe_3O_4$ and the second reduction step corresponds to $Fe_3O_4 \rightarrow \alpha$-Fe (Hong Wang et al., 2009). The activation of Fe_2O_3 in CO or H_2/CO also proceeds in a two-step process, the reductive decomposition of the iron oxide and the carburization of the iron oxide (Fe_3O_4) to the iron carbide. The first step corresponds to the reduction of $Fe_2O_3 \rightarrow Fe_3O_4$ and the second carburization step corresponds to $Fe_3O_4 \rightarrow Fe_xC$, resulting in a number of different iron carbides. The term carburization is therefore used to describe the transformation of the iron oxide to the iron carbide phase. Hence, irrespective of the activation gas used Fe_3O_4 is always an intermediate step in the reduction process (Herranz et al., 2006). Moreover, depending on the extent of reduction FeO may also form as an intermediate step, altering the overall reduction to a three-step process:

$Fe_2O_3 \rightarrow Fe_3O_4 \rightarrow FeO \rightarrow \alpha$-Fe (during H_2 activation) or Fe_xC (during CO activation).

The formation of various iron carbides is dependent on the activation condition employed as well as the nature of the catalyst. For instance, the hexagonal carbide (ε-Fe_2C) has been reported to form by carburizing of the iron oxide or iron powder at temperatures as low as 170^{o}C in a flow of CO. By increasing the temperature to 250^{o}C ε-Fe_2C may transform into the Hägg carbide (χ- Fe_5C_2), which at temperatures above 450^{o}C may eventually decompose into cementite (θ-Fe_3C). Cohn et al. 1950, reported that θ-Fe_3C could also be formed by the reaction of iron with χ-Fe_5C_2 at temperatures above 260^{o}C. The transformations discussed above are illustrated in figure 2.12, and it was imperative to understand this reduction behaviour as it affected the choice of activation procedure used in this work.

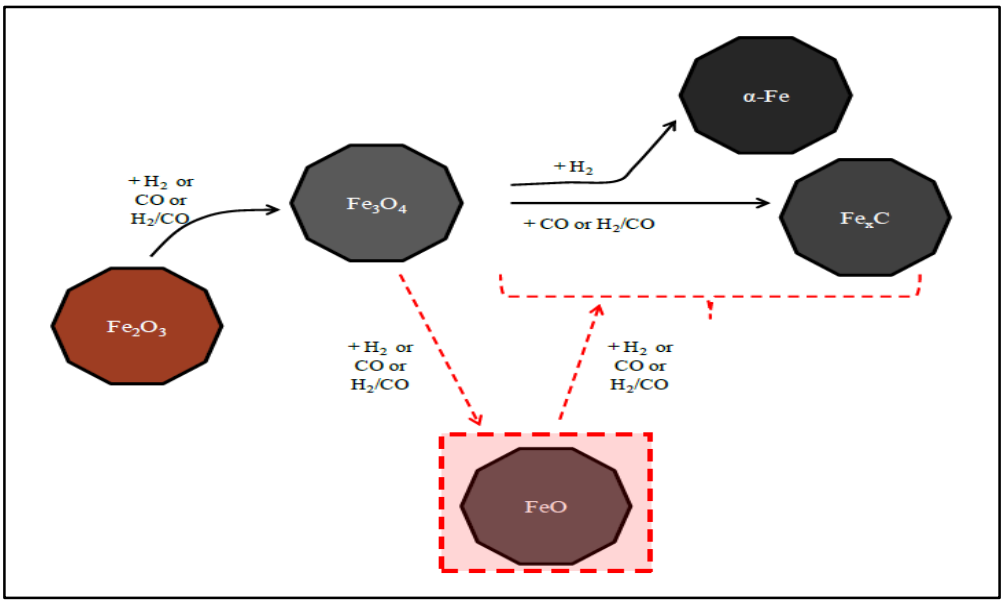

Figure 2. 12: Phase(s) transformation of the iron-based Fischer-Tropsch catalyst during H_2, CO or H_2/CO activation.

2.11 Effect of iron phases (Fe_3O4, Fe_xC) on performance of the iron-based FT catalyst:

The nature of the final phase(s) formed after the activation process plays a vital role in the Fischer-Tropsch synthesis performance (Dragomir B. Bukur et al., 1995a). The proposition that under FT synthesis conditions, iron catalysts co-exist as a mixture of metallic iron, magnetite, and several iron carbides phases creates part of the confusion as to which phase is responsible for the Fischer-Tropsch synthesis performance. Several researchers have tried to know the effect of different pre-treatment as well as correlate the phase(s) with the FTS activity observed (D. B. Bukur et al., 1995b, Rao et al., 1996). A closer look at the work done to date was therefore necessary.

2.11.1 Magnetite (Fe_3O_4) as the active phase for the Fischer-Tropsch synthesis:

Studies conducted by (Loaiza-Gil et al., 1999) highlighted the formation of carbonaceous deposits on iron-based catalysts in FTS. They studied specifically the effect of pressure. Activation of catalysts were done using hydrogen. The results showed that increasing the pressure led to high CO conversion. After the reaction, determination of the phase composition of the spent catalyst by Mössbauer Emission spectroscopy revealed that α-Fe, χ-Fe_5C_2 and Fe_3O_4 were the dominant phases. A conclusion was made that Fe_3O_4 was the active phase for F-T synthesis since it appeared that there was a relationship between the Fischer – Tropsch activity and the phase composition. Other scholars such as (Blanchard et al., 1982, Reymond et al., 1982) were also of the proposition that Fe_3O_4 was the active phase for Fischer-Tropsch synthesis.

2.11.2 Iron carbide as the active phase for the Fischer-Tropsch synthesis:

Bukur et al., 1995c, studied the effect of activation conditions on iron catalysts activity during FT synthesis. They used a supported iron-based catalyst which was activated at 280ºC, for various times (1-12 hrs.) in H_2 and CO gases, respectively. They reported that the H_2 activated catalyst exhibited a steady increase in FTS activity. The increase in activity was accompanied with the carbiding of metallic iron to pseudo-hexagonal ε-carbide. The initial activity obtained over the CO activated catalyst was higher than that of the H_2 activated catalyst. Furthermore, the CO activated catalyst showed a decrease in FT activity with time on stream, due to the partial conversion of χ-Fe_5C_2 to less active magnetite, in agreement with the hypothesis that an iron carbide is the active phase for the Fischer-Tropsch synthesis (Amelse et al., 1978, Raupp and Delgass, 1979, Dragomir B. Bukur et al., 1989).

In another study, (Ding et al., 2011) investigated the effect of reducing agents on microstructure and catalytic performance of precipitated iron-manganese catalyst for the Fischer-Tropsch synthesis. The iron catalyst was activated in H_2, CO and H_2/CO at 265 ^{0}C for 24 hrs. They reported that the CO activated catalyst showed the highest initial activity compared with the H_2 and H_2/CO activated catalysts. A slight deactivation of the CO activated catalyst was also observed. This was attributed to the conversion of χ-Fe_5C_2 to Fe_3O_4. The activity of the H_2 activated catalyst increased gradually with the conversion of metallic iron to χ-Fe_5C_2 and ε-carbide upon exposure to syngas. The relationship between iron phases and FTS activity indicated that the formation of χ-Fe_5C_2 on the surface layers had a higher activity for the Fischer-Tropsch synthesis than ε- carbide. The formed Fe_3O_4 had a negligible effect on the Fischer-Tropsch synthesis activity. Similar, results have been reported by Bell and Dictor, (1986), (Shroff et al., 1995). The above studies were therefore all of the idea that iron carbides are the active phases. These conflicting reports necessitated the preparation of both magnetite and iron carbides separately as explained in the following chapter.

Chapter 3

Experimental and Analytical Details:

3 Introduction:

This chapter presents a summary of the experimental techniques used for the synthesis, characterization and performance testing of magnetite and iron carbide nanoparticle mixtures. Nanocatalysts were prepared using a modified solvothermal technique and biopolymer route respectively. Catalysts were then characterised using traditional techniques which included transmission electron microscopy (TEM), scanning electron microscopy (SEM), and X-ray diffraction (XRD). A detailed description of each procedure employed in the synthesis of nanocatalysts is presented and the theoretical background on each of the three main characterisation techniques used to investigate the surface chemistry and morphology of the synthesized samples is also discussed. The chapter then closes with an overview of the procedures employed during the running of the Fischer – Tropsch reaction as well as the sampling and analysis of the products.

3.1 Background:

Catalysts for Fischer – Tropsch reaction are synthesized using various techniques which have been discussed earlier in this work (literature review). Some of the methods however have some major drawbacks especially in controlling size and size distribution of the synthesized particles. The benzyl alcohol route, which is a solvothermal synthesis technique has been proved to be a versatile option for the synthesis of iron oxide nanoparticles as demonstrated by Niederberger et al., 2005 and Niederberger et al., 2006. The method has the benefit of overcoming the main drawbacks of surfactant- assisted routes and traditional aqueous sol–gel chemistry techniques. Consequently, it offers benefits such as high crystallinity of the as-synthesized nanoparticles and high reproducibility in terms of the produced particle size distributions. This is mainly achieved through controlling the growth of crystals from the solution in the absence of any additional ligands (Niederberger et al., 2006). The only problem with this approach that is that, particles will require functionalisation. However, for application in slurry phase FTS, no functionalisation and redispersion is required since particles will be able to achieve the desired result if only activated by initially exposing them to reducing atmospheres of either hydrogen, CO or syngas. The following sections will outline the experimental procedures that were used to synthesize all the iron based nanocatalysts.

3.2 Preparation of magnetite nanocatalysts:

Magnetite nanocatalysts were synthesized through a modified solvothermal technique which occurred at a constant elevated temperature of 190 ^{0}C for a period of two (2) hours. The synthesis procedure was based on the benzyl alcohol, solvothermal synthesis route. Magnetite NPs with diameters of about 7 – 15 nm were prepared by using 4 grams of an iron precursor, iron acetylacetonate, $(Fe(acac)_3)$. This was added into a homogenous mixture of 140 ml Benzyl alcohol (BA) and 20 ml of Benzaldehyde (BD) which was preloaded in a 600 ml stainless steel stirred tank Parr reactor from Parr Instruments Company. Magnetic stirring of the mixture at speed of 700 rpm ensured the production of uniformly sized nanoparticles. An inert atmosphere was maintained by continuously bubbling argon gas through the solution at a flow rate of 100 ml/min and simultaneously heating the reaction mixture to 190 ^{0}C at a rate of 5 ^{0}C/min under ambient pressure. Figure 3.1 below shows the setup that was used for the synthesis.

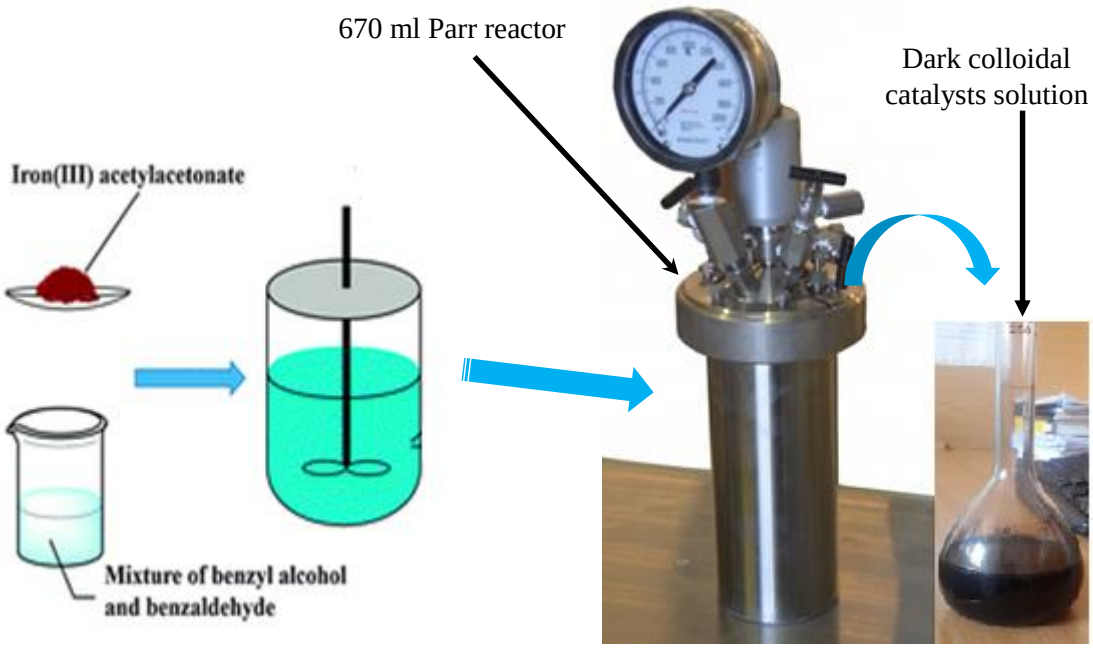

Figure 3. 1: Process flow for the synthesis of magnetite nanoparticles (NPs).

The mixture was then kept at 190 ^{0}C for 2 hours yielding a dark colloidal solution which was cooled to room temperature. Uniform NPs of different sizes ranging from 7 nm to 15 nm were fabricated depending on the composition of the initial mixture of the reagents. The cooled dark colloidal solution was then transferred to plastic centrifugation bottles and the solution was centrifuged for seven (7) minutes at 5000 rpm to separate the nanoparticles from the solution. Isolated nanoparticles were then washed alternately with ethanol and dichloromethane until they were clean and separated from the remaining solvent. Samples of the washed nanoparticles were then oven dried at 90 ^{0}C for 24 hours. Uniform NPs of different sizes ranging from 7 nm to 15 nm were fabricated.

3.3 Synthesis of Carbides F_3C nanocatalysts:

Iron carbide nanoparticles were prepared using three routes which used three different biopolymers. Gelatin, chitosan and ammonium alginate were used for particle size control and as carbon sources in the synthesis of iron carbide nanoparticles.

3.3.1 The Gelatin route:

In this preparation route, 2g of powdered gelatin was dissolved in 100 ml of deionized water at 90 ^{0}C, forming a clear colourless solution. This solution when left to cool formed a thick gel that could be easily reversed to a liquid by warming the solution to approximately 65 ^{0}C at atmospheric pressure. The iron precursor for this synthesis was an oxidized form of Iron (II) acetate. A few drops of hydrogen peroxide (H_2O_2) was used to oxidise and achieve this increase in oxidation state of iron (II) to iron (III) acetate which is highly soluble and yields uniformly sized nanoparticles. Two (2) grams of 95% iron (II) acetate from Sigma Aldrich, was dissolved in 20 ml of deionized water to give a dark brown solution. To produce iron carbides, 6 ml of iron acetate solution was added dropwise to 5 ml of the biopolymer solution accompanied by fast stirring, to give a clear brown, viscous solution. This resulting viscous product was then cast to watch glasses and allowed to dry at 50 ^{0}C in an oven for 24 hours, resulting in the formation of clear red/brown films.

Figure 3. 2: Laboratory equipment setup for the preparation of iron carbide nanoparticles.

The resulting films were calcined at 2 ^{0}C per minute to 650 ^{0}C in long glass crucible in a box furnace under a continuous flow of nitrogen to provide an inert environment and cooled immediately. The inert atmosphere prevented the combustion of the biopolymer under adverse heating conditions.

3.3.2 The Alginate Route:

Iron carbide nanocatalysts were also prepared using an ammonium alginate biopolymer matrix. A 2% ammonium alginate solution was prepared by the addition of 2g powdered FMC Biopolymer alginic acid in 100 ml of deionized water. Ammonium alginate does not readily dissolve in water and to dissolve the solid, ammonium hydroxide solution was carefully added dropwise until the resulting solution had a final pH of 6.5. A solution of iron (III) acetate which worked as the iron source was prepared separately by dissolving 2 g of iron (II) acetate procured from Sigma Aldrich in 20 ml of deionized water giving a dark brown solution. A few drops of H_2O_2 was also added to the solution to give a more homogenous solution of iron III acetate. To synthesize iron carbide, the hydroxide form of the compound was first prepared by adding 6 ml of iron acetate solution dropwise to 5 ml of the biopolymer solution with fast stirring using a magnetic stirrer bar, forming a brown cross-linked thick gel. This gel was then cast into Petri dishes as shown in figure 3.2 and dried in an oven which was maintained at 50 ^{0}C to produce mottled red/brown films. The resulting films were then calcined at 2 ^{0}C /min to 650 ^{0}C in a long glass sample holder that was inserted into a box furnace. Nitrogen gas was continuously introduced to create an inert atmosphere and the sample was removed immediately when the temperature reached 650 ^{0}C and cooled in a closed glass conical flask to prevent further oxidation.

3.3.3 The chitosan Route:

This route made use of 75-85% deacetylated chitosan flakes secured from Sigma Aldrich (product number: 448869). The synthesis procedure involved the preparation of a chitosan solution by stirring 2g of the flakes in 100 ml of 2% aqueous acetic acid for 24 hours. The iron precursor solution was then prepared in the same way as for the other biopolymers. The clear brown, viscous solution that was produced was also placed in watch glasses which were oven dried by exposing them to a temperature of 50 ^{0}C resulting in the formation of clear red/brown films. The resulting films were also calcined in the carbolite box furnace shown in figure 3.3 below which was equipped with a temperature controller for the accurate control of the thermal degradation step to yield the desired iron carbide nanocatalysts.

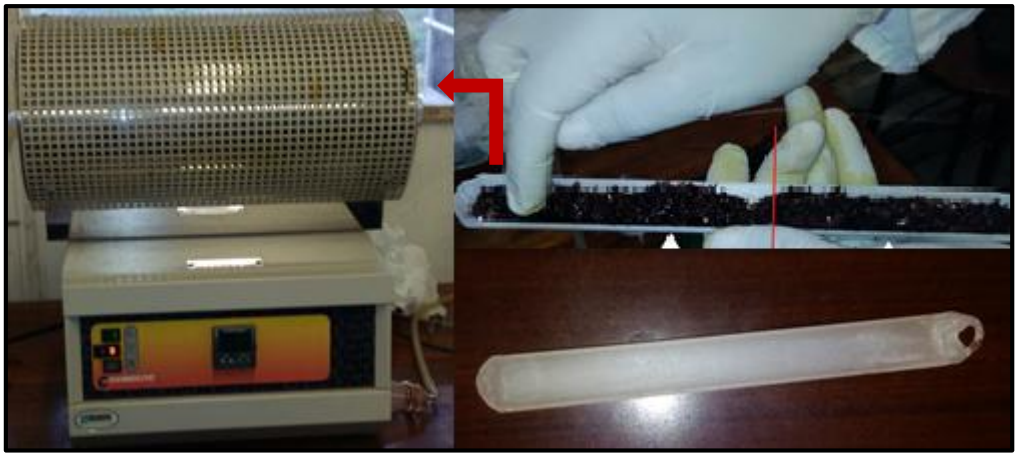

Figure 3. 3: Carbolite box furnace with a Eurotherm temperature controller and sample holder.

Catalysts were prepared in small batches to promote a closer control of the size and morphology of the resulting catalyst particles. Figure 3.2 shows hot plate magnetic stirrers that were used for these syntheses. Quantities were accurately measured out using standard laboratory measurement equipment which will not be discussed in depth in this work.

3.4 Characterisation of Nanocatalysts particles:

In catalysis, characterisation of particles uses electron microscopy as the first characterization tool to get direct, local information on target catalysts particles at atomic level resolutions. Samples are analysed in a contaminant-free environment under high-vacuum conditions. The fact that it enables us to view particles at atomic resolution is very useful in getting more insights about the catalysts being investigated. Electron microscopy uses an electron beam source in place of the light source as used in light microscopes. Optical lenses are replaced by electro-magnetic lenses. The principle of operation remains the same but with electron microscopy, enhanced capabilities and magnification are produced. Electrons in the electron beam have typical wavelengths of $\lambda = (5 – 10)$ picometers, which give them the capability of imaging nanometer-sized crystallites with greater flexibility. The reason being that the wavelengths of such electron beams are by far shorter than those of visible light which has values in the range of $\lambda = (400 – 800)$ nm. When electrons hit the sample (target), they generate a range of signals which are used for all kinds of characterization techniques and this gives rise to the difference in operating principles of SEM and TEM.

Table 3. 1: Differences between SEM and Transmission Electron Microscopy (TEM).

SEM	TEM
Based on secondary or back-scattered electrons.	Based on transmitted electrons.
Focuses on topology and composition of a surface.	Shows many characteristics of the sample, such as particle size and morphology, crystallization and even magnetic domains.
Allows for large amount of sample to be analysed at a time.	Only small amount of sample can be analysed at a time.
It provides a 3-dimensional image.	Provides a high resolution 2-dimensional image.

3.4.1 Scanning electron microscopy (SEM)

To understand the surface topography, structure and morphology of the catalysts, a scanning electron microscopy (SEM) was used. This is one of the common characterization techniques in catalysis that allows three-dimensional viewing of small particles. Sample preparation of all the catalysts involved breaking of catalysts lumps using a ceramic pestle and mortar to iron out the small lumps that had been formed during storage. The resulting very fine powder was then sprinkled on small sticky black paper containing graphite. The sample papers were initially stuck on aluminium stubs and the loaded samples were then coated with a thin layer of gold. This was done to make the samples conductive and therefore prevent charge build up. Single spot analysis was done on different parts of the samples to determine the surface topography, structural morphology, shape and elemental concentrations of the catalysts.

A scanning electron microscope (JEOL JSM 6100 SEM) connected to a 4 Quadrant Back Scatter Detector and an EDX analysis software was used as a tool in the determination of the approximate concentrations of iron, carbon and oxygen in the catalysts. The SEM was operated in a high vacuum mode with an accelerating voltage of 10 kV.

3.4.1.1 SEM operating principles:

Scanning electron microscopes work by rastering and focusing the beam on the catalysts surface in a systematic way and the elemental composition of the sample from within the deep parts of the catalysts can also be determined. This is usually achieved through the use of back scattered electrons which are more energetic than secondary electrons that are used to give surface information. It is the number of the electrons detected relative to the position of the primary beam that gives the surface information of the sample. Heavy metals are more efficiently scattered and appear brighter in the image displayed on the screen which can be saved for future analyses.

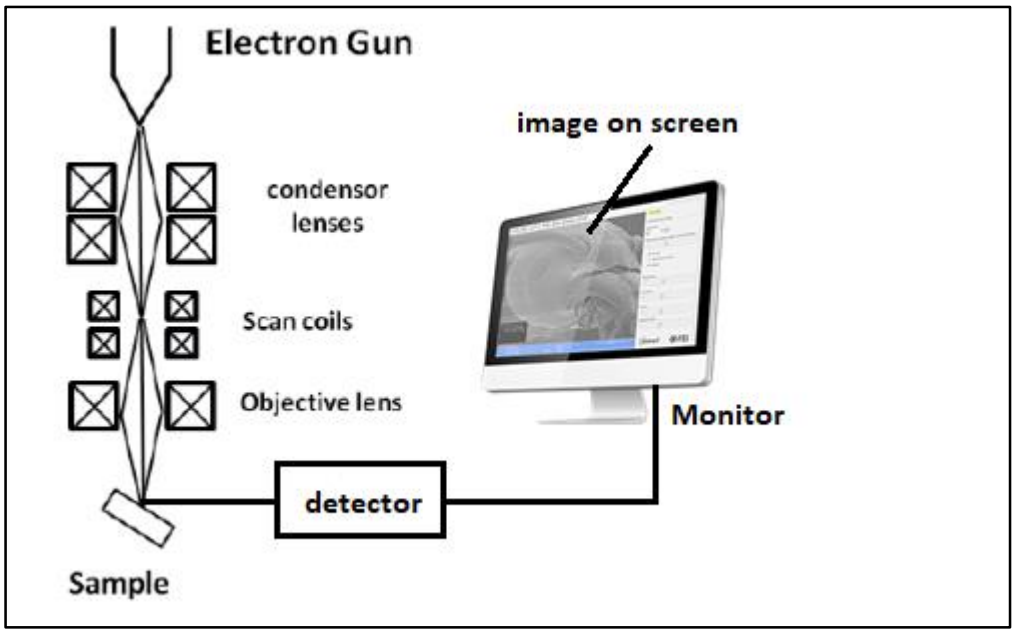

Figure 3. 4: Schematic representation of scanning electron microscope, adapted from (Niemantsverdriet, 2007).

3.4.2 Energy Dispersive X-Ray Analysis (EDX):

This spectroscopic technique which is also referred to as EDS, is an X-ray technique used to identify and approximate the elemental composition of materials. It is usually used in materials and product research, troubleshooting and deformulation. EDX systems usually do not work as separate units but as attachments to electron microscopy instruments such as Scanning Electron Microscopy (SEM) or Transmission Electron Microscopy (TEM). In this instance, the imaging capability of the microscope identifies the specimen of interest. Through EDX analysis, a spectrum showing peaks corresponding to the elements making up the composition of the sample being analysed is produced. Elemental mapping of a sample and image analysis are also possible in EDX measurements in which the distribution of the elements making up the specimen is ascertained.

As an initial step in qualitatively identifying the elements making up the catalysts samples, Energy dispersive X-ray spectroscopy (EDX) was used and this made use of a Bruker X-ray spectrometer that was connected to the JEOL JSM 6100 SEM instrument. The amount of iron, carbon and oxygen detected by this instrument from the magnetite and iron carbide catalysts was just approximate since XRD was believed to be more precise in determining the phases and hence the relative amounts. A working distance of 4mm was chosen as it gave the best magnifications.

To study the distribution of the elements on the catalysts surface, elemental mapping was carried on using another instrument connected to the SEM. A JEOL 2100 was used and it gave approximate data that was used to quantify these elements. There was concern that the information obtained from this analysis will not be very accurate due to fluctuating amounts of electrons reaching the sample and

intensity of the X-Rays generated and emitted. Therefore, identification only was possible as these affect repeatability and precision of quantitative analysis.

3.4.3 Transmission electron microscopy (TEM):

In order to extensively study and analyse the size, shape and catalysts phase compositions of the nanocatalysts, a transmission electron microscope was used. The samples to be analysed were first crushed using a ceramic pestle and mortar to form a very fine powder and a few micrograms of the samples were added to microcentrifuge tubes containing ethanol. The microtubes were then sealed and sonicated in an ultrasonic bath for 20 minutes. This caused the nanoparticles to form a sufficiently thin slurry of nanocatalysts. Carbon-coated copper grids were then used to hold a few drops of the sonicated sample for analysis. Samples on grids were allowed to dry out by exposing them to air. TEM measurements were performed with a FEI Tecnai G2 Sphera electron microscope mounted with a LaB6 filament powered at 200 kV. The images that were obtained were then processed using the iTEM® software to measure approximately 70 crystallites on each image to obtain the crystallite size distributions. These images were taken using a 1024 x 1024 Gatan CCD camera that was connected at the bottom. To enhance visibility, bright field mode was selected for all the images that were produced.

3.4.3.1 TEM operating principles:

In a transmission electron microscope, an electron beam is transmitted through a thin electron transparent sample. At the top of the TEM column a high voltage electron emitter (electron gun) produces a beam of electrons possessing a high energy (100 300 keV) and intensity.

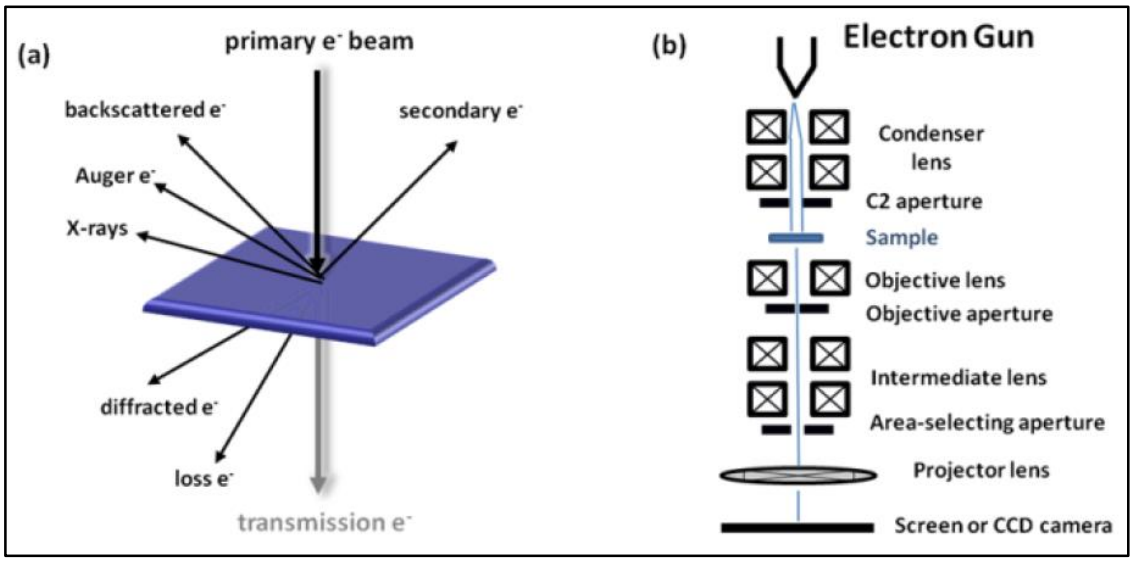

Figure 3. 5: (a) Signals used for transmission electron microscopy; **(b)** schematic setup of TEM.

These electrons have such a high kinetic energy that samples thinner than 50 nm become partly electron transparent and the so-called transmission electrons will travel through a condenser aperture to create

parallel rays which impinge on the sample (less than 100 nm in thickness) and generate a shadow-image. This shadow-image gives detailed information about the internal structure of the materials (crystal lattices, stacking faults, etc.). Since the attenuation of the beam depends on the thickness and density of the sample, the transmitted electrons form a two-dimensional projection of the sample mass and is subsequently magnified by the electron optics to produce a so-called bright-field image. When one diffracted electron beam is selected it is called the dark field method (and a dark field image is produced).

The benefit of using TEM to characterize particles especially iron carbide nanoparticles which were embedded in the biopolymer matrix is the distinctive contrast between particles and the carbon matrix. This difference in contrast arises due to density and thickness variation of the sample which influences electron scattering. Dense regions or those with heavier elements can scatter the electron beam stronger, resulting in darker features in the TEM image. Also, less dense regions or those with lighter elements show as brighter features. A typical transmission electron microscope and a sample holder is shown in figure 3.6.

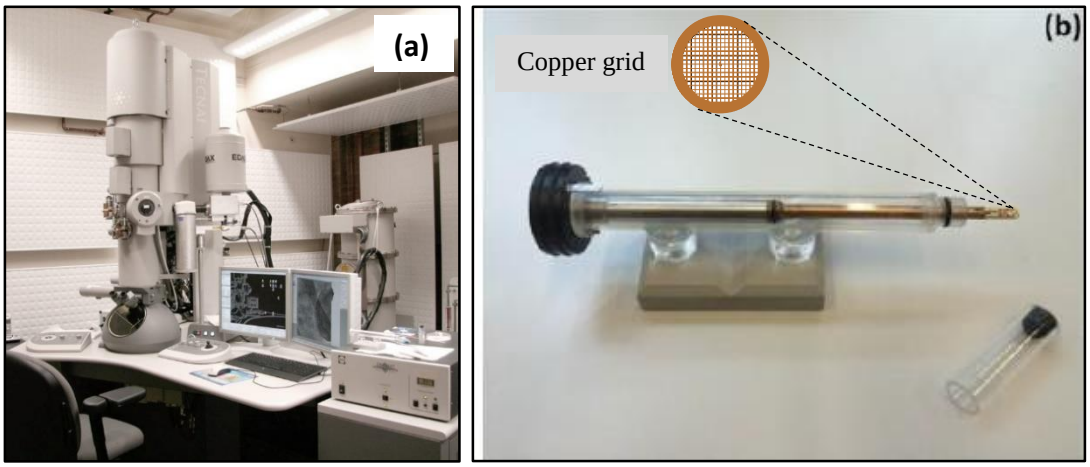

Figure 3. 6: **(a)** FEI Tecnai G2 Sphera microscope; **(b)** sample holder with copper grid.

3.4.4 X-ray diffraction

The determination of the crystallite sizes and identity of crystalline phases of catalysts in the prepared iron carbide and dried magnetite samples, used X-ray diffraction. The main objetive of this characterisation step was to assess whether the catalysts were in the required phases, that is magnetite (Fe_3O_4) for the iron oxides and cementite (Fe_3C) for the iron carbide. Crystallite phases of spent catalysts were also determined by means of X-ray diffraction to assess whether major phase changes happened during their activity in the reaction medium.

Powder X-ray diffraction is a non distructive technique and for this analysis a one gram sample of each catalyst type was required. Sample prepararion involved removal of lumps in the samples so as to have

a homogeneous sample using a cermamic pestle and motar. The prepared samples were carefully loaded and compacted into four (4) circular stainless steel sample holders which were then loaded into the diffractometer.

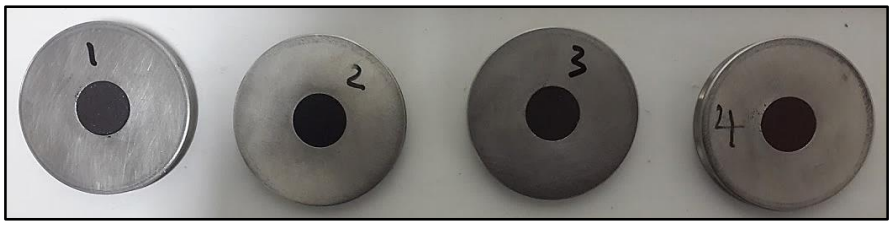

Figure 3. 7: Magnetite and cementite samples loaded into stainless steel sample holders for PXRD analysis.

Measurements were done on a Malvern Panalytical's X-ray Diffractometer with a Co-Kα radiation source (λ = 1.78897Å). The scan range was $0° < 2\theta < 90°$. All diffraction patterns were recorded in the step-scan mode with a step size of 0.01 degrees and a scan rate of 1 °/min. The diffractograms were analysed using X'Pert Highscore Plus® software and the diffraction peaks of crystalline phases were also compared with those of standard compounds reported in the JCPDS3 data file. Average crystallite sizes, d_{c-XRD} (mean volume diameters) were calculated from the peak width at half maximum using the Debye-Scherrer equation:

$$d_{c-XRD} = \frac{K\lambda}{\beta Cos\,\theta} \qquad Equation\ 3.1$$

Where *K* is the Scherrer constant (usually taken as unity, when the exact particle shape is unknown), λ is the wavelength of X-rays the incident on sample, β is a parameter known as the full width at half maximum (FWHM) of the identified peaks which is measured in radians. The diffraction angle θ is given in degrees and is at the maximum point of the peak. The units for d_{c-XRD} are in nanometers.

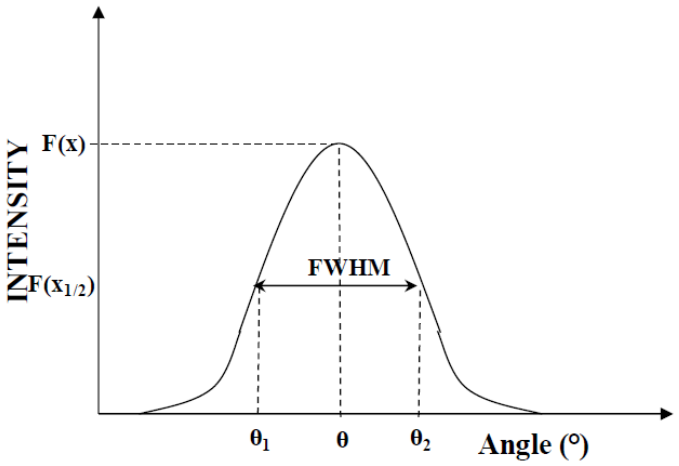

Figure 3. 8: Full-width half maximum schematic representation.

3.4.4.1 Operating principle of XRD:

An XRD instrument works by irradiating highly energetic, X-rays on a sample, penetrating it and hence diffraction will occur if the material is crystalline. The diffracted X-rays provide information about the internal structure of the catalyst particles on unit cell dimensions. Figure 3.9 below shows the schematic representation of the operating principle of an XRD.

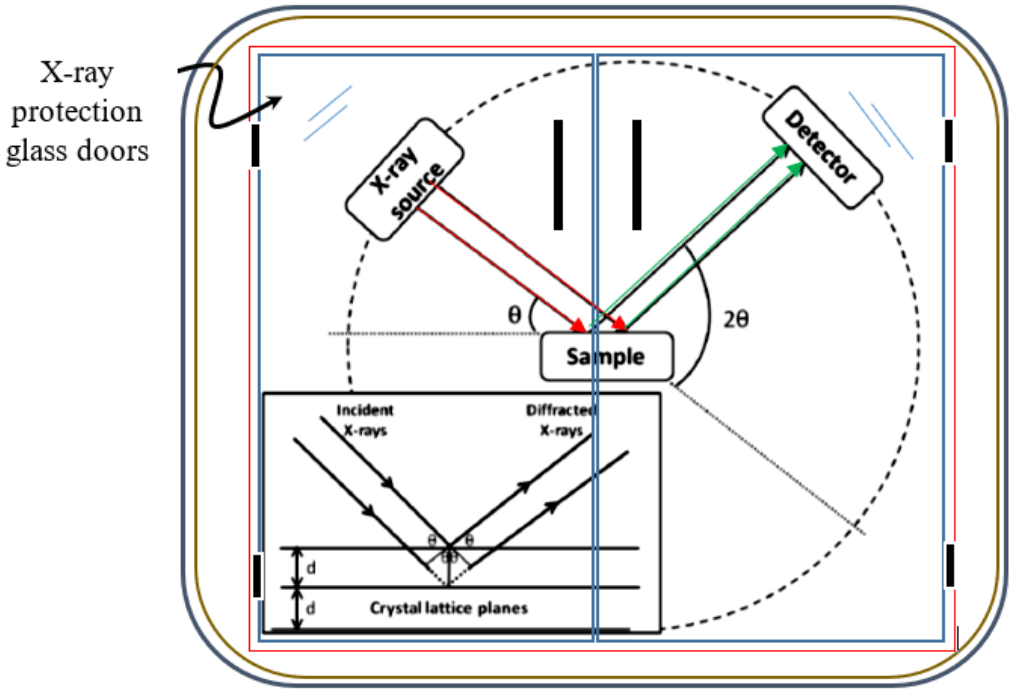

Figure 3. 9: Schematic representation depicting the operating principle of an XRD instrument.

The X-ray source emit photons which are scattered elastically by atoms in the lattice. When the lattice is ordered, as in a crystalline material, the scattered X-rays can interfere. To have constructive interference, the difference in distance that the radiation travels (dashed part in the insert in Fig.3.9) should be an integer times its wavelength. When the conditions for constructive interference are fulfilled, the diffracted X-rays are in phase. The intensity of these diffracted X-rays is recorded by a detector as peaks at a particular angle 2θ. The distance between two lattice planes can therefore be calculated from the angles where diffraction peaks are observed in the XRD diffractograms using Bragg's law:

$$2d.\sin\theta = n\lambda \text{ with } n = 1, 2 \ldots \qquad \text{Equation 3.2}$$

d is the spacing between crystal planes, θ is the angle of reflection, n is an integer called the order of the reflection, and λ is the wavelength of the X-rays. The wavelength of the X-rays depends on the type of target material that is used inside the cathode X-ray tube. The most common X-ray sources used for XRD uses copper and cobalt targets, which emits Cu or Co Kα X-rays. The set of diffraction peaks and corresponding d-spacings are characteristic for each crystallographic phase and are extensively

documented in databases, such as the Powder Diffraction Files (PDF) from the International Centre for Diffraction Data (ICDD). These reference spectra are used to identify crystalline material in a catalyst, such as metal nanoparticles, oxides such as magnetite and metal carbides. The ultimate use of all the catalysts characterisation results was to make sure that particles of the right particle size and phase were produced. Catalysts were then tested at relevant industrial conditions in a bench scale slurry phase Fischer-Tropsch reactor.

3.5 Fischer- Tropsch Synthesis Experiments:

In order to determine the optimum catalyst mixture composition for the production of higher C_{5+} hydrocarbons, the prepared catalysts were mixed in different proportions and tested for their performance in the slurry phase Fischer-Tropsch reaction. In these experiments, the measured response was the selectivity for different hydrocarbons produced when a particular catalyst mixture is used. The response was assumed to only depend on the relative proportions of the components (magnetite and cementite) in the mixture and not on the amount of the mixture as it was fixed at 4 grams. The data obtained was then used to relate the response data as functions of the mixture components and other factors such as particle size which were selected for the experiment. This experimental design was deemed sufficient and fit to test the proposed model of a mixture of catalysts for the slurry phase Fischer – Tropsch synthesis.

3.5.1 The Fischer –Tropsch experimental test unit

Catalysts performance testing was carried out in the experimental system shown in Figure 3.6. It consisted of a Parr slurry reactor that was connected using gas lines which were equipped with mass flow controllers, two hot and cold catch pots, and an accompanying back-pressure regulator. The test rig allowed for off-line GC (TCD and FID) analyses of both the tail gas and the unreacted synthesis gas during calibration and flow verification. It also enabled the analysis of the liquid products by collecting samples in the two separate catch pots. Hydrogen and CO gases were fed from gas cylinders (H_2: 99.99%; CO: 99.976%) both procured from Afrox. A H_2 to CO ratio of 2 for the synthesis gas was used for all experiments and argon was used for pressurizing the system as well as a coolant during shutdown. The Fischer-Tropsch synthesis reaction was conducted in a Parr reactor (CSTR). Both the reactor set-up and the sampling system configuration (off-line) had a significant impact on the integrity and interpretation of the experimental results and therefore will be discussed in detail.

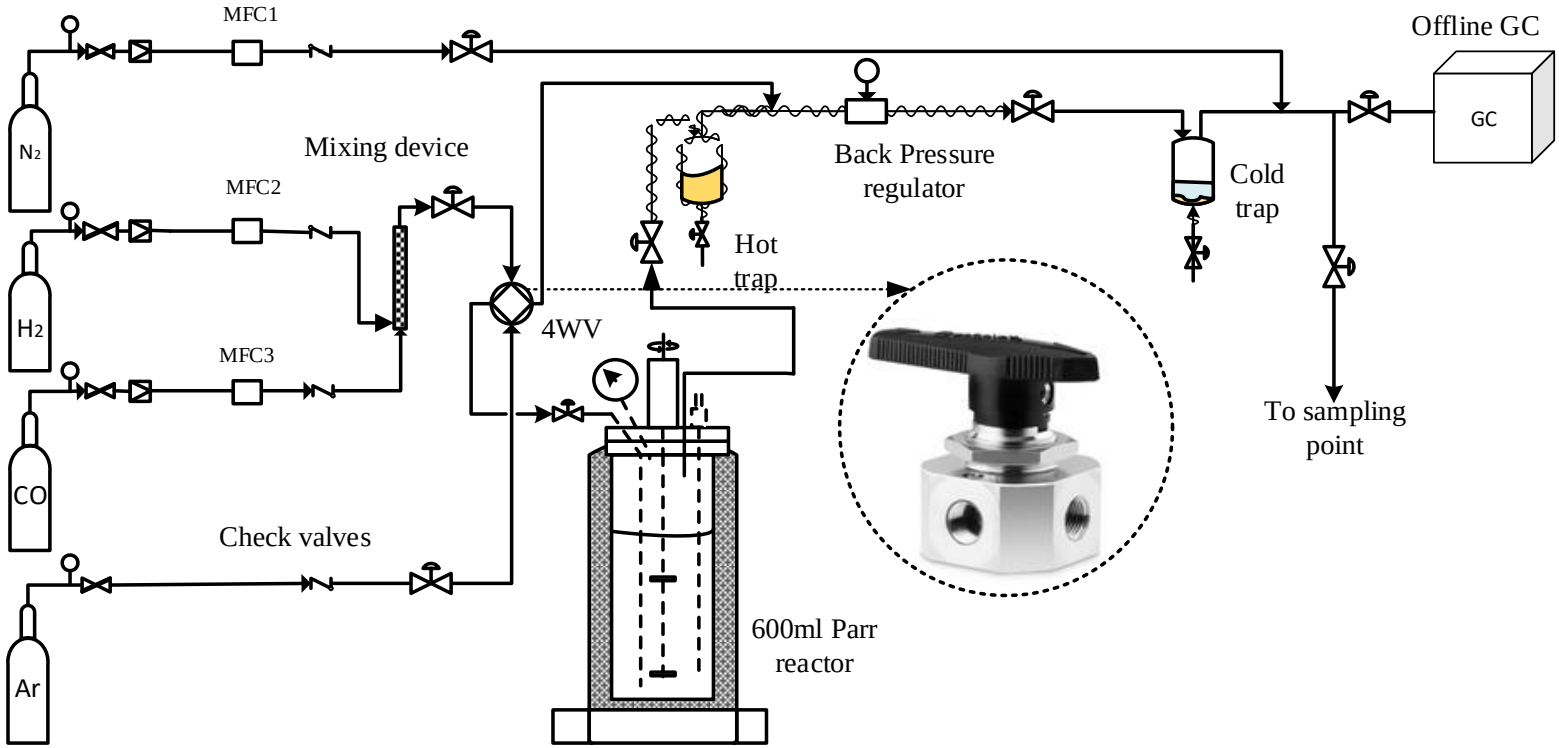

Figure 3. 10: Flow diagram of the designed experimental setup; some lines were heat traced to avoid blockages by condensing waxes.

3.5.1.1 Feed gas supply:

The feed supply and sampling system are illustrated in figure 3.11. The feed gas supplied to the reactor system comprised of a mixture of hydrogen (H_2: 99.999%) and carbon monoxide (CO: 99.97%) in a ratio of 2:1. Argon (Ar: 99.999%) by virtue of being inert was also fed to the reactor system at the beginning of each FTS run as it served as a pressurizing gas to the operating pressure of 20 bar. The feed gas cylinders were each equipped with an appropriately sized in-line pressure regulator set at a supply pressure slightly above 20bar to ensure that reactants continuously flow into the reactor. Spring loaded relief valves were provided for over pressure protection. The feed gas flowrates were monitored by employing Shanghai Cixi Mass Flow Controllers (MFCs). To protect the flow controllers from dust and other particulates in the gases, each gas supply line was equipped with an in-line filter element. H_2, CO and Ar were fed separately and were then premixed before directed into the slurry reactor using the four-way valve.

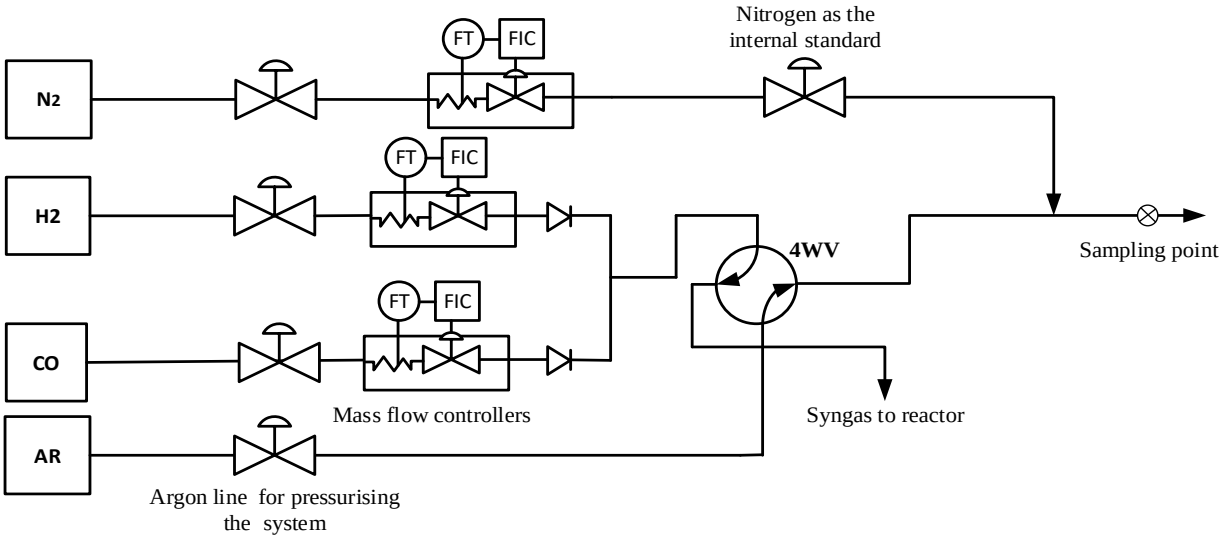

Figure 3. 11: Schematic representation of the feed gas supply including mass flow controllers.

The flow controllers are mass flow based and make use of heat capacity measurement to measure flow. Flow controllers were specifically calibrated for the three gases by the manufacturer before delivery. To prevent cross contamination of gasses and backflow of hot oil rich gases, the feed gas lines were each equipped with spring loaded non-return valves. The spring loaded non-return valves also prevented wax returning into the feed line and in the process protecting the delicate MFCs. A pressure gauge was connected to the top of the reactor to measure reactor pressure during synthesis conditions. An off-line gas sampling purge system branches off before the line gets into the reactor. This enabled the verification of the reactants composition before and during the process. Nitrogen gas was used as the internal standard in the quantification of all the hydrocarbons produced.

3.5.1.2 Reactor

The reactor used for all synthesis reactions is a slurry reactor from Parr instruments with a liquid volume of 670ml at 230 °C (78 mm ID). Figure 3.12 illustrates the reactor and its accompanying components as used in this study. Figure 3.13 illustrates the various internal elements which are within the reactor.

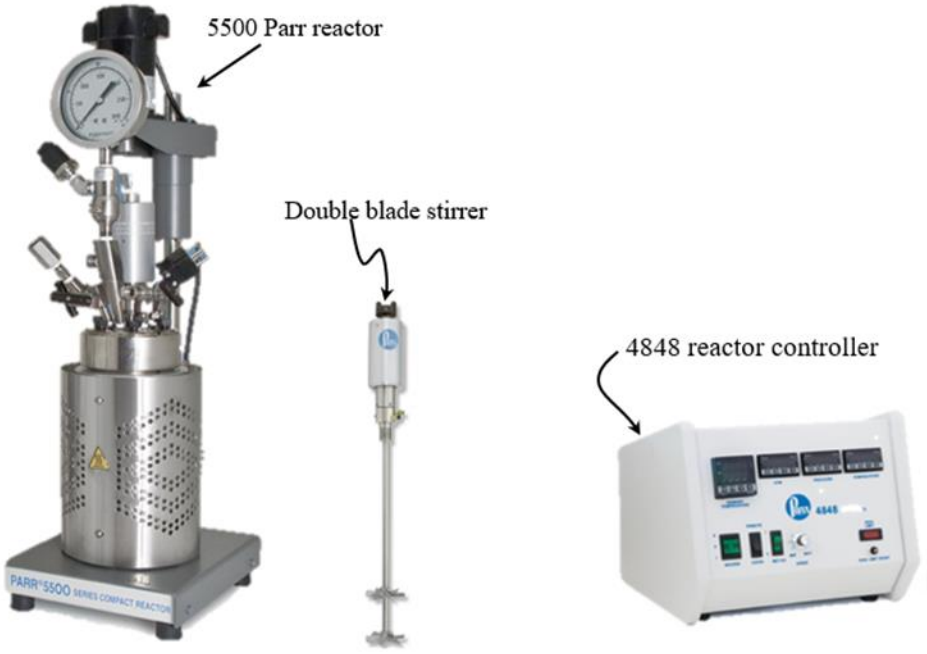

Figure 3. 12: Components of the Parr reactor system used for Fischer – Tropsch synthesis**.**

Good mixing of the three-phase mixture containing the catalysts and the slurry was accomplished using a double blade stirrer as shown in figure 3.13. There was a slight increase in the total volume of the slurry as a result of the additional volume of the other reactor components which included the cooling coil, the double blade stirrer as well as the feed gas line. These took some additional volume but what was important was the fact that the volume should always be below the outlet line. The stirrer is connected through a magnetically coupled and sealed connection on the vessel flange, to an external variable speed motor which has its speed controlled on the reactor controller. The mixing device ensures effective mixing of the liquid and gas in the reactor vessel. The first blade element (impeller) of the double-blade stirrer is located approximately halfway up the reactor height and it induces a downward forcing action sufficient for adequate mixing. The second flat blade element is located approximately 5 mm from the bottom of the reactor vessel providing additional mixing at the bottom of the reactor vessel as well as preventing catalysts from settling.

The gas inlet enters the reactor at the top of the reactor vessel through the flange and goes through the liquid to the bottom leaving a gap of approximately 5mm between the bottom and the tip. This maximizes gas dispersion and prevent gas from bypassing along the vessel walls. The formed liquid and gaseous products in their vapour phase escape through the outlet located at the top of the reactor. A filtering element was added to prevent catalysts from escaping. Reaction temperature was monitored by a Pt-100 thermocouple placed in the slurry as shown in figure 3.13 below. The vaporised product from the reactor leaves through the outlet pipe (**P**) and goes to the hot trap that is maintained at 180 degrees Celsius. This is where some of the heavy liquid and waxy products are recovered.

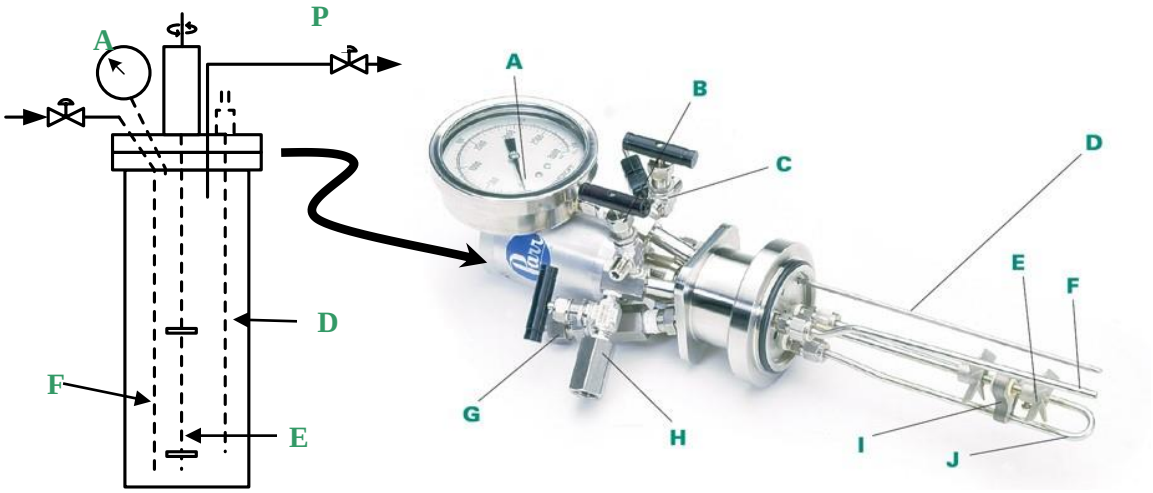

Figure 3. 13: Internal components including the stirrer and cooling coil of the Parr reactor from Parr instruments.

A – Pressure gauge**, B** – Liquid sampling valve**, C** – Gas release valve, **D** – Pt-100 thermocouple, **E** – Internal stirring system, **F** – Dip tube**, G** – Safety rupture disc**, H** – Gas inlet valve**, I** – Guide, **J** – Cooling coil.

The reactor vessel was equipped with a removable electrical heating jacket in the form of an aluminium block and a temperature control system. The temperature controller that comes with the reactor facilitated accurate temperature control during process changes and associated temperature variations resulting from the heat generated by the Fischer-Tropsch exothermic reaction. This was achieved by submerging the thermocouple into the reactor vessel and ensuring direct contact with the reaction media. By appropriately programming the required temperature conditions, the controller maintained the constant or ramping temperature profiles as required.

3.5.1.3 Pressure control:

A Swagelok back-pressure regulator (BPR) controlled the system pressure. Its set point was manually set using argon gas. Two pressure indicators were available on the system, one on the Parr reactor itself and the other one on the back-pressure regulator. A difference between these two readings will show a possible blocked line or a major leak in the system. Blockages may cause overpressure and will result in unstable operating conditions as they block the flow and hence alter the quantity of the resulting products. The system was therefore made up of ¼ inch stainless steel pipes for all streams to protect it from blockages and any other situations that might arise. Figure 3.14 shows the configuration of the back-pressure regulator that was used for this application.

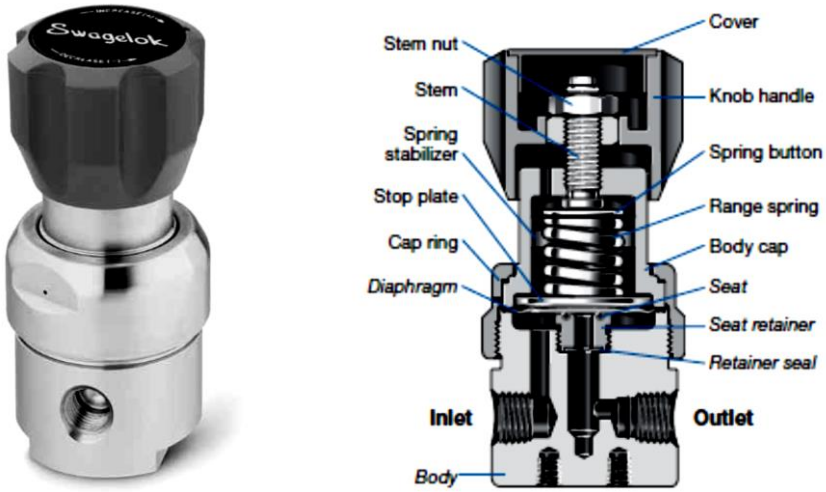

Figure 3. 14: KPB series back-pressure regulator configuration used for pressure control.

3.5.1.4 Liquid product recovery and sampling:

Figure 3.15 is an illustration of the liquid product recovery system. From the reactor outlet, a gaseous stream passes through a temperature-controlled product line (180°C) to a hot trap vessel. The hot trap vessel was also temperature controlled at 180°C and captured high molecular mass hydrocarbons (wax). From the hot trap the exit line feeds to a cold trap vessel. The cold trap was operated at room temperature and captured the lighter hydrocarbon products (oil) and reaction water. The hot and cold traps were drained manually on a regular basis, after every 48 hours and the products analysed soon after sampling using off-line gas chromatography (GC).

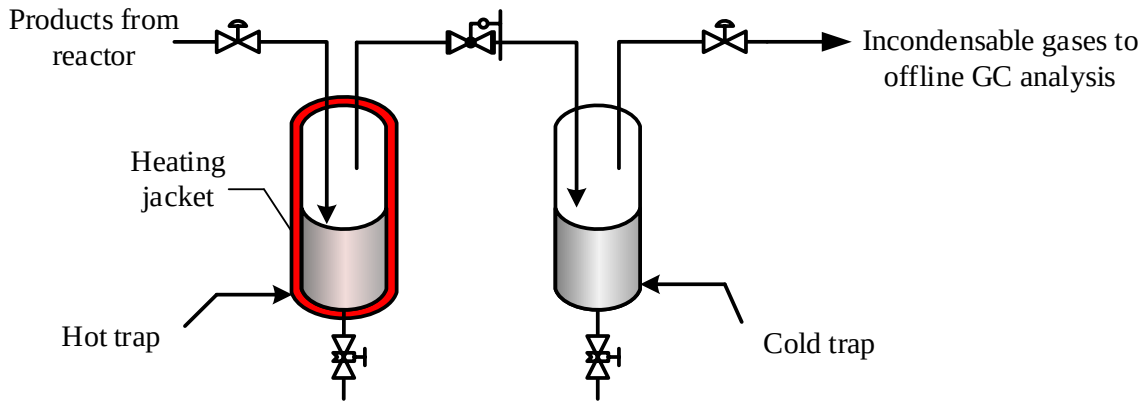

Figure 3. 15: The liquid product recovery system consisting of a hot and cold catch pots.

3.6 Reactor operation

3.6.1 Start-up

Prior to all the experiments, a leak test was performed to make sure that the system was pressure tight and ensure that the mass balances will be correct. This was done by setting the back – pressure regulator to 20 bar and feeding H_2 to test the reactor at pressures of 5, 10, 15 and 20 bar. For each test, the H_2 flow was stopped at the desired pressure and the pressure gauge was observed for about 24 hours. The test was considered successful if the reactor pressure did not drop by more than 0.5 bar during this time. If the pressure loss exceeded 0.5 bar, the joints were checked for leaks using SNOOP® (leak detector fluid), retightened and the pressure test repeated until a satisfactory pressure test was achieved. Upon achievement of a satisfactory pressure test, the reactor was depressurized to atmospheric pressure and at this stage the reactor system will be ready for experimental runs.

During reactor start-up the reactor vessel was loaded with 160 ml of Durasyn-164 Poly-Olefin solvent and 4.00 g of mixed magnetite and iron carbide catalysts to form a slurry medium. The reactor was then sealed and the outlet valve on the vessel opened. The stirrer was set to a speed of 450 rpm and temperature of the reactor noted. Activation gas was then introduced to the system and once all the set activation conditions were at the required set points the temperature was ramped up uniformly to 250 ºC at a rate of 2 ºC /minute.

3.6.2 Catalyst activation:

Before the commencement of every Fischer-Tropsch reaction run, the catalysts slurry was activated or reduced *in-situ* using a stream of carbon monoxide for 16hrs. A gas flow rate of 100 sccm (standard cubic centimeters per minute) was used for the entire 16 hours and a maximum temperature of 250 ºC was used for this activation step. Thereafter the reactor temperature, pressure and synthesis gas flow rate were

changed to Fischer-Tropsch reaction conditions. The whole temperature profile was controlled by the external Parr 4848 temperature controller (shown in figure 3.12 above) that comes with the reactor.

Table 3. 2: Catalysts activation conditions.

Activation / Reduction Conditions:	
Activation gas	Carbon monoxide
Mass of catalyst	4.00g
Pressure	Atmospheric, (1 bar)
Temperature	250 ºC
Flow rate	100 sccm

3.6.3 Fischer-Tropsch synthesis:

After catalyst activation, the controller was programmed to ramp down the temperature from the maximum activation temperature of 250 ºC to 220ºC as fast as possible. The reactor pressure was then manually adjusted upwards in small increments from atmospheric to 20 bar (abs) using argon gas. For this study these conditions were referred to as the standard synthesis conditions. All experimental runs were kept at the standard synthesis conditions for 48 hours to allow the system to stabilize and reach steady state. After this period, the reactor conditions were maintained as indicated on the experimental schedule below and samples were withdrawn for offline Gas Chromatography analysis (GC). Nitrogen gas at a constant rate of 9.70 sccm was added to the tail gas stream to serve as an internal standard for products quantification calculations. Fischer-Tropsch reaction was conducted for approximately five (5) days at these steady state conditions and samples were taken and quantified using a GC-TCD as well as FID for light gaseous hydrocarbons having up to four (4) carbon atoms (C_4).

Table 3. 3: Schedule of Experiments:

Experiment	**Mixture Composition (% magnetite)**	**Syngas ratio H_2/CO**	**Temperature (ºC)**	**Pressure (bar, abs.)**
1	100	2	220	20
2	90	2	220	20
3	70	2	220	20
4	60	2	220	20
5	50	2	220	20
6	30	2	220	20
7	20	2	220	20
8	0	2	220	20

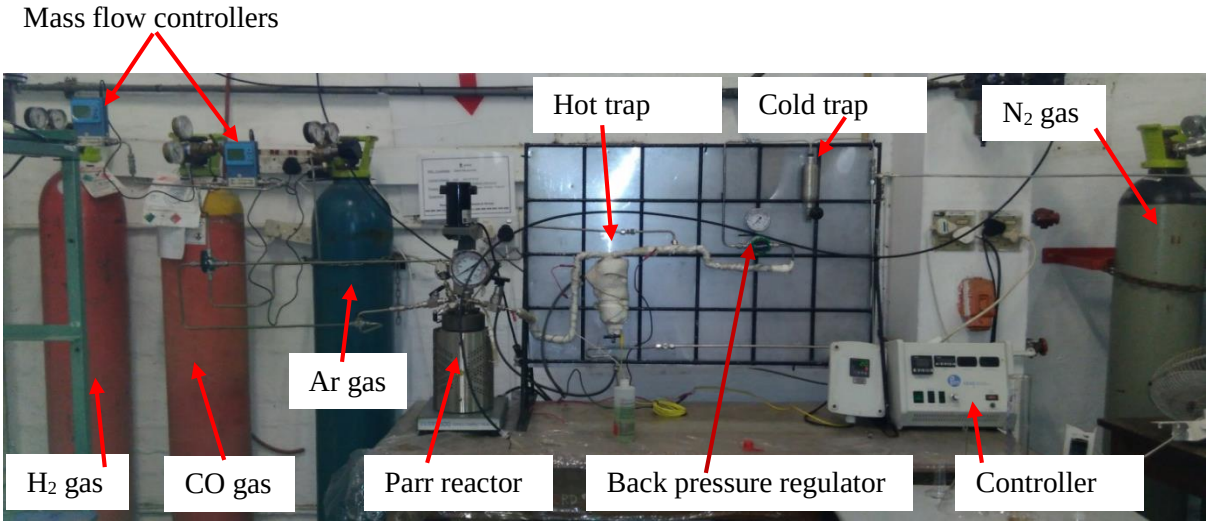

Figure 3. 16: Set-up of the Fischer-Tropsch testing rig.

3.7 Experimental procedure for synthesis runs:

Eight catalyst samples which were prepared by mixing magnetite and iron carbide nanocatalysts in different proportions as shown in table 3.3 above were each tested in a five-day Fischer-Tropsch synthesis run. Catalysts mixtures were identified based on the percentage of magnetite in the sample. For example, a catalyst mixture having a percentage composition of 100% had all the 4.00 grams comprised of magnetite and a 70 % mixture contained 2.80 grams of magnetite and 1.20 grams of iron carbide. Prior to the commencement of each FT reaction, the catalyst mixture was mixed with Durasyn-164 polyolefin solvent, to form a slurry phase and hence the name slurry phase Fischer-Tropsch synthesis.

The catalysts suspension was then activated *in situ* prior to the reaction. This was done at atmospheric pressure using CO (see Table 3.2). After activation the reactor was switched to bypass and cooled under argon to the reaction temperature of 220 °C. Once at reaction temperature, the reactor system was pressurized to 20 bar using argon gas. The Swagelok back-pressure regulator allowed the system to vent off excess pressure and exit the reactor system. Steady and accurate flow rates of reactant gases were cross checked by consecutive bypass analyses of synthesis gas (H_2, CO) relative to the reference gas (N_2). A synthesis gas stream at a total flow rate of 45 sccm with a H_2/CO ratio of 2 was introduced into the reactor and maintained for the entire course of the reaction and sampling procedure. The reaction temperature was kept at 220°C for all the synthesis runs.

3.7.1 Sampling and analysis of feed gas:

The actual composition of the combined stream of feed gas (CO and H_2) before the reaction was determined by sampling the bypass stream using a 1ml Hamilton gas tight syringe. The sample was analysed on an

offline Shimadzu 2010 *Plus* gas chromatograph system. Bypass samples were taken until the flow rates and the syngas feed ratio of two (2) was achieved. The ratio confirmation stage was done just after the catalysts activation process was completed. The four-way valve was then switched to flow through the reactor afterwards and a stop watch was used to mark the beginning of the Fischer-Tropsch reaction and measure the length of the experimental run and sampling intervals. The reaction was continuously monitored for consistency in H_2/CO ratio at regular intervals during the reaction.

3.7.2 Fischer Tropsch Product sampling and analysis:

Gas chromatography was used for the quantification and analysis of both the reactant gases and the Fischer-Tropsch products. The flow rate of gaseous products was also determined on the same GC-TCD and GC-FID which allowed the determination of the quantities of all the gaseous hydrocarbons. Liquid products were analysed using a GC-MS system which enabled the identification of the synthesised liquid hydrocarbons.

3.7.3 Inorganic gases sampling and analyses with TCD:

Inorganic gases such as hydrogen, CO and CO_2 from the reactor were analysed using an offline GC system. The flow rates were important in the calculation of reactant conversions. The instrument used for this analysis is a Shimadzu 2010 *Plus* GC and its detector temperature was set at 230°C. The relative errors for the TCD were usually ± 3% (Lokhat, 2012). The following table provides the conditions at which the off-line GC-TCD was operated. Argon was used as a carrier gas since it allowed the clear separation of N_2, H_2 and CO under these conditions. Use of helium resulted in the formation of one big peak of H_2, N_2 and Ar in the chromatogram.

Table 3. 4: Conditions for offline gas chromatographic analysis on a TCD:

Parameter settings	
Detector	Thermal conductivity detector (TCD)
Column type	Carboxen PLOT 1010 capillary
Column dimensions	30m x 0.53mm x 30 µm
Stationary phase	Carbon molecular sieve phase
Carrier gas	Argon
Column flow rate (ml/min)	2.06
Column temperature (^oC), isothermal	150
Detector temperature (^oC)	230
Filament temperature (^oC),	230
Injector temperature (^oC),	230

3.7.4 Organic gaseous products sampling and analyses:

The exit line from the cold trap is connected to a sampling port for off-line GC analyses. Figure 3.10 are illustrations of the gas sampling system. The organic products were collected using a gas tight 1 ml Hamilton syringe and manually injected into an offline Shimadzu (2010) *Plus* gas chromatograph equipped with a Flame Ionization Detector (FID). The methane produced in the reaction was utilized as the reference compound to link results obtained from both TCD to FID for quantification of all the other hydrocarbons with longer chains.

Table 3. 5: Conditions for offline gas chromatography analysis on FID.

Parameter settings	
Detector	Flame Ionization Detector (FID)
Column type	Carboxen PLOT 1010 capillary
Column dimensions	30m x 0.53mm x 30 µm
Stationary phase	Carbon molecular sieve phase
Carrier gas	Argon
Column flow rate (ml/min)	2.32
Column temperature (^{o}C), isothermal	200
Detector temperature (^{o}C)	250
Injector temperature (^{o}C),	230

3.7.5 Analysis of liquid phase products:

The analysis of the liquid samples was divided into 3 sections which included:

- sample from the cold trap,
- samples from the hot trap and
- waxy products from the reactor after separating the spent catalysts.

The liquid phase organic product samples were withdrawn from the cold trap that was maintained at ambient temperature as well as from the hot trap which was maintained at 180 ^{o}C. The sample withdrawn from the cold trap was comprised of two distinct layers, an aqueous layer and an organic layer. The sample was first allowed to settle for some time and then carefully separated into two separate phases which were analysed separately using an off-line gas chromatography system connected to a mass spectrometer as the detector.

3.7.5.1 Analysis of the aqueous fraction:

The aqueous fraction of the sample collected from the cold trap was analysed using a Shimadzu 2010 *Plus* GC-MS system with a split/splitless injector. The GC was equipped with a 50m Quadrex stainless steel ultra-alloy capillary column. The analyses of the aqueous fraction targeted carboxylic acids, alcohols and all carbonyl compounds. Summarised information on the details of this analysis is given in Table 3.6 below. All the oxygenated compounds (C_1 – C_7) in this fraction were targeted for identification (qualification) only.

3.7.5.2 Analysis of the organic fraction:

The organic hydrocarbons fraction was analysed using an off-line GC-MS system employing the same analysis method as with the aqueous fraction. This analysis was aimed at **identifying** all the paraffinic and olefinic hydrocarbons in the C_5 – C_{50} range. All the hydrocarbons that were detected in this range were not directly quantified individually but only identified. This is because the main thrust of this work was to determine the achievable C_{5+} selectivity of the slurry phase Fischer-Tropsch process using a mixture of magnetite and iron carbide nanocatalysts. In this regard, it means no external or internal standard was used for the quantification of the detected liquid hydrocarbons. The use of standards for all these hydrocarbons would have made the whole quantification procedure extremely expensive as some pure standard samples had to be bought. To avoid this cost, the C_1-C_4 hydrocarbons selectivities obtained from the FID were sufficient to calculate the C_{5+} selectivity.

Table 3. 6: Conditions for gas chromatographic analysis of the aqueous fraction using GC-MS.

Parameter settings	
Detector	Mass Spectrometer MS
Column type	Quadrex ultra-alloy fused silica capillary
Column dimensions	50m x 0.53mm x 30 µm
Stationary phase	Carbon molecular sieve phase
Carrier gas	Helium
Column flow rate (ml/min)	2.32
Column temperature program (°C),	50 °C – 250 @ 5 °C /min 250 °C – dwell 5 minutes 250 °C – 400 @ 2.5 °C /min
Detector temperature (°C)	250
Operation mode	Constant pressure

3.7.5.3 Reactor residue (wax/heavy product) analysis:

The wax product was collected from the reactor products after spent catalysts were separated from the slurry. The remaining slurry was allowed to settle, and a sample was then drawn and analysed using a

Shimadzu 2010 *Plus* GC-MS system using a stainless steel ultra-alloy column. The analysis was done in order to identify more long-chain hydrocarbons that were produced during the synthesis but remained in the reactor due to their high boiling point.

3.7.6 Shut down procedure

After five days of Fischer-Tropsch reaction, with one unique catalysts mixture, the reaction was stopped so that the reactor can be cleaned. A new sample of catalysts with a different composition was then added, and the process continued for another five days with the new conditions. The shutdown procedure began with the ramping down of the reactor temperature to ambient conditions. This was done as quickly as possible using the temperature controller program. The pressure was also brought down manually in small steps to atmospheric by opening the backpressure regulator slowly and at the same time switching gas flow through the reactor to 200ml/min argon. The flow of inert gas was continued until the reactor was cooled and ready to be opened. The stirrer was also stopped once the reactor temperature reached 34^{o}C. Catalyst slurry was then removed from the reactor and sealed in an air tight container for later separation and analysis.

3.8 Data evaluation and work-up:

The data that is extracted during a Fischer-Tropsch synthesis run has a lot of meaning if its processed into various quantities that give a clear information on the extent of the reaction and performance of the catalysts.

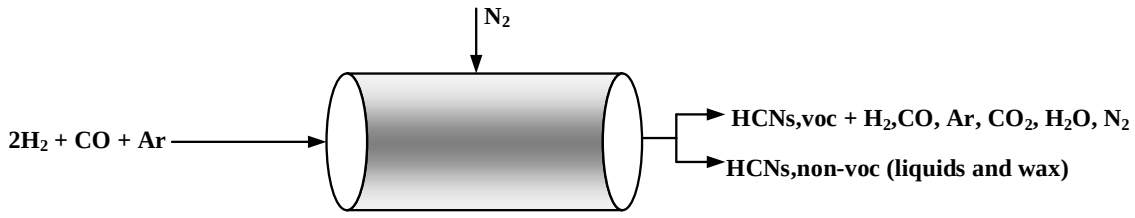

Figure 3. 17: Reactants, products and reference compound (N_2) required for mass balance calculations around a Fischer – Tropsch reactor.

(VOC: Volatile Organic Compounds; HCNs: Hydrocarbons.)

Amongst this data set, reaction conditions such as temperature, pressure, flow rates of feed gas and tail gas, mass of liquid and wax product collected were the most important pieces of information that was extracted for calculations. Quantities such as Fischer-Tropsch reaction rates, CO and H_2 conversions, and hydrocarbons selectivities are some of the typical parameters that were calculated from the data. The section

that follows, explains how the data was processed for system performance evaluation using iron carbide and magnetite nanocatalysts mixtures.

3.8.1 Calculation of flow rates of compounds:

Flow rates of compounds were determined from data obtained from gas chromatography equipped with both a thermal conductivity detector (TCD) and a flame ionization detector (FID). TCD was mainly used for the detection and quantification of permanent gases whereas FID was used for all the organic compounds. The TCD was calibrated regularly using a standard gas mixture of known composition. This gas was specifically prepared by Air products® for the calibration of the GC system. From the peak areas obtained in the analyses, calibration factors$\left(f_{TCD,i}\right)$, were calculated using nitrogen (N_2) as the reference gas. The mixture contained six (6) gases which were mixed in known proportions expressed as percentages as shown in table 3.7 below.

Table 3. 7: Standard calibration gas mixture composition from Air products:

Gas	Mole %
H_2	40.1
CO	20.0
CO_2	9.6
Ar	10.2
CH_4	14.9
N_2	5.2

The TCD calibration factors for each component *i*, were calculated using the following equation:

$$f_{TCD,i} = \left(\frac{A_{N_2}}{A_i}\right) \times \left(\frac{\dot{n}_i}{\dot{n}_{N_2}}\right) \qquad \text{Equation 3.3}$$

Where: $f_{TCD,i}$ = calibration factor of component i

A_{N_2} = integrated peak area of Nitrogen;

A_i = integrated peak area of species i;

$\dot{n}_i$ = molar flow rate of component i,

$\dot{n}_{N_2}$ = molar flow rate of Nitrogen.

And;

$$\dot{n}_{N_2} = x_{N_2} \frac{\dot{v}_{ref(NTP).}}{V_A} \qquad \text{Equation 3.4}$$

Where, x_{N_2} is the mole fraction of nitrogen in the reference gas;

$\dot{v}_{ref}$(NTP) is the volumetric flow rate of the reference gas and

V_A is the Avogadro volume (22.4 cm^3/mole) at NTP.

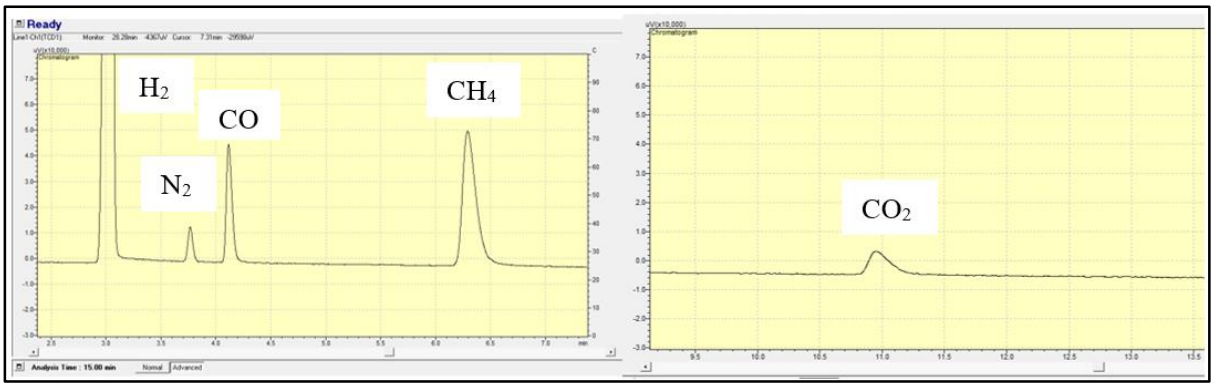

Figure 3. 18: Gas Chromatogram of the standard mixture using Ar as carrier gas at an isothermal analysis temperature of 150 ºC.

The molar flow rates of component gases were obtained from the following equation:

$$\dot{n}_i = f_{TCD,i} \times \left(\frac{A_i}{A_{N_2}}\right) \dot{n}_{N_2} \qquad \text{Equation 3.5}$$

Before every experimental run, the syngas ratio was measured in reactor bypass mode as being:

$$H_2/CO = \frac{A_{H_2} \times f_{TCD,H_2}}{A_{CO} \times f_{TCD,CO}} \qquad \text{Equation 3.6}$$

3.8.2 Calculation of reactants conversion:

Table 3. 8: Calibration factors for TCD.

Gas	Calibration factor ($f_{TCD,i}$)
H_2/ N_2	10.45
CO/ N_2	1.12
CO_2/ N_2	1.10
CH_4/ N_2	3.80
N_2/ N_2	1.00

The reactant gas conversions were calculated from the following equations:

$$\text{Hydrogen conversion: } X_{H_2} = \frac{\dot{n}_{H_2,IN} - \dot{n}_{H_2,OUT}}{\dot{n}_{H_2,IN}} \qquad \text{Equation 3.7}$$

$$\text{Carbon monoxide conversion: } X_{CO} = \frac{\dot{n}_{CO,IN} - \dot{n}_{CO,OUT}}{\dot{n}_{CO,IN}} \qquad \text{Equation 3.8}$$

3.8.3 Calculation of yield and selectivity of hydrocarbons:

Once the product flow rates are calculated, the selectivities and yields of all the hydrocarbons on a carbon basis were obtained utilizing equations. The yield of a component *i* in the product stream was determined using equation 6 below:

$$Y_{i,C} = \frac{\dot{n}_{i,out}}{\dot{n}_{CO,in}} \qquad \text{Equation 3.9}$$

The selectivity of a component i was computed using equation 7 below:

$$S_{i,C} = \frac{Y_{i,C}}{X_{CO} - Y_{CO_2}} \qquad \text{Equation 3.10}$$

Formation rates of individual gaseous organic products (C_2-C_4) were quantified and analysed using a flame ionization detector as well as a mass spectrometer (MS). The MS was used to identify all the hydrocarbons, and this enabled the determination of the C_{5+} selectivity. The molar flow rates of these individual organic compounds in the C_2-C_4 carbon number range were determined as follows:

$$\dot{n}_i = \left(\frac{f_i \times A_i}{f_{CH_4} \times A_{CH_4}}\right) \times \left(\frac{CN_{CH_4}}{CN_i}\right) \times \dot{n}_{CH_4} \qquad \text{Equation 3.11}$$

Where:

f_i = response factor of substance i (Equation 8);

A_i = the peak area of substance i obtained from the FID chromatogram;

CN_i = is the carbon number of substance i;

$\dot{n}_{CH_4}$ = is the molar flow rate of methane obtained from the TCD.

And $f_i = \frac{N_{C,i}}{N_{c,no(O)} + 0.55\,(N_{C,C-O})}$ Equation 3.12

Where:

$N_{C,i}$, = total number of carbon atoms in the substance;

$N_{c,no(O)}$ = number of carbon atoms not bonded to an oxygen atom (≈ 1);

$N_{C,C-O}$ = number of carbon atoms bonded to an oxygen atom (≈ 0.55) and

A carbon atom attached with a double bond to oxygen has no response $N_{C,C=O}$ (Kaiser, 1969). The response factors of most hydrocarbons are tabulated in table 3.9 below as predicted by Kaiser, (1969). This method

of calculating response factors has a lot of cost savings attached to it as it makes it easier to predict the hydrocarbons response factors instead of measuring all of them separately.

Table 3. 9: Hydrocarbon notations and calculated FID response factors (Kaiser, 1969).

Compound	Code	Carbon No.	FID Observed Carbon No.	Response Factor
Methane	**100**	**1**	**1**	**1.00**
Methanol	110	1	0.55	1.82
Ethane	**200**	**2**	**2**	**1.00**
Ethene	201	2	2	1.00
Ethanol	210	2	1.55	1.29
Ethanal	207	2	1	2.00
Propane	**300**	**3**	**1**	**1.00**
Propene	301	3	3	1.00
Propanol (-1)	310	3	2.55	1.18
Propanal	307	3	2	1.50
Propanol(-2)	315	3	2.55	1.18
Propanone	317	3	2	1.50
Butane	**400**	**4**	**4**	**1.00**
Butene-(1)	401	4	4	1.00
tr.-Butene-(2)	402	4	4	1.00
cis-Butene-(2)	422	4	4	1.00
Butanol(-1)	410	4	3.55	1.13
Butanal	407	4	3	1.33
Butanone(2)	417	4	3	1.33

Chapter 4

Results and Discussion:

4 Introduction:

This chapter aims to present the results, observation and discussions pertaining the experimental work performed on magnetite and iron carbide nanocatalysts. It lays out all the results from the preparation of the catalysts to their performance testing in slurry phase Fischer-Tropsch synthesis. Scanning Electron microscopy (SEM), Transmission Electron Microscopy (TEM), Energy Dispersive X-ray Spectroscopy (EDX) and Powder X-ray Diffraction (PXRD) were used as particle characterisation techniques. These results are presented, discussed and their interpretation given therein. Results for both the magnetite and iron carbide nanocatalysts as well as comparative calculations on particle size and size distribution as determined from TEM micrographs and Scherrer equation are also presented. Fischer-Tropsch catalyst performance testing results including a quantitative measure of reactants conversion, yield of products and catalysts selectivity are presented and discussed. The chapter then closes by presenting a discussion on the product selectivity and hydrocarbon product distribution and finally on the characterisation of spent catalysts to assess the extent of phase and particle size change due to exposure to Fischer-Tropsch reaction conditions.

4.1 Results of the preparation of catalysts:

Highly crystalline and magnetic nanocrystals of magnetite were prepared, and samples were oven dried before characterisation. Iron carbide nanocatalysts were calcined in a box furnace as this was the last step in their preparation. The nanocatalysts required a thermal degradation step to facilitate the transformation from iron hydroxides to iron carbide. The preparation of a sample of magnetite nanocatalysts took about two (2) days while for iron carbides the period was around three (3) days because of the very slow drying rate of the hydroxide gels. The following results gives more information on the preparation of each type of catalysts.

4.1.1 Results of the preparation of magnetite nanocatalysts:

Catalysts particles with size ranging from 7-15 nm were prepared using a modified solvothermal synthesis route and catalysts yields of greater than 50% were obtained. Smaller batches of catalysts were synthesised

so as to monitor particle size growth and hence size distribution of the nanocatalysts. The time taken to synthesize a solution of the particles was approximately three (3) hours and the resulting black colloidal solution containing highly magnetic nanocatalysts was allowed to cool, settle and sediment. This took 5-6 hours after which the top layer containing a mixture of benzyl alcohol and benzaldehyde was then carefully decanted out. It is the remaining concentrated sample which was then centrifuged, washed using dichloromethane and ethanol. It was then dried for 24 hours to give brownish black magnetite nanocatalysts samples of as shown in figure 4.1 below.

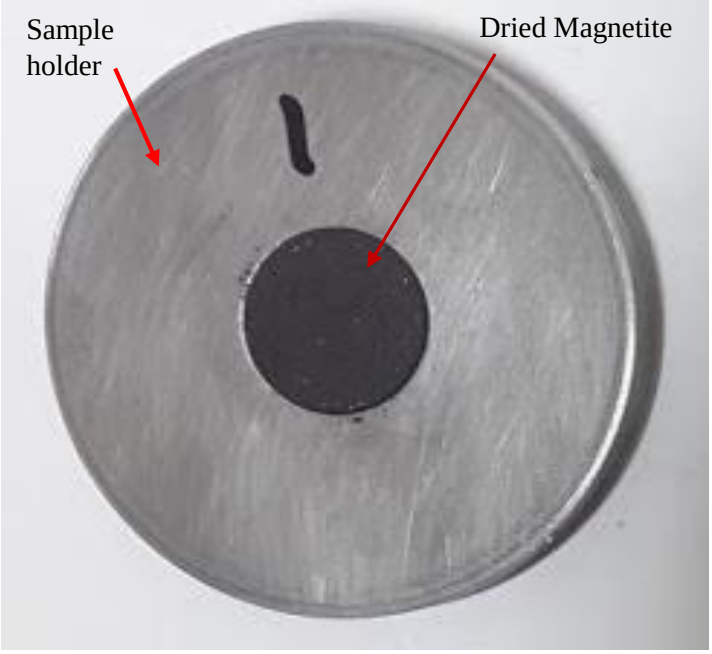

Figure 4. 1: Magnetite sample after drying at 50 ^{0}C for 24 hours.

Several batches of magnetite nanocatalysts were synthesized, and the amount of benzaldehyde was varied from 12 ml to 20 ml in each synthesis run. Table 4.1 provides a summary of the average mass of catalyst that was recovered in each run for four synthesis runs. The benzaldehyde (BD) was used as a capping agent in controlling the catalysts particle growth during synthesis.

Table 4. 1: Catalysts recovery using different amounts of benzaldehyde.

Mass of acetonate (g)	Amount of BD added/ml	Yield (g)	%recovered
4.00	12	2.43	60.8
4.00	14	2.40	60.0
4.00	16	2.37	59.3
4.00	18	2.33	58.3
4.00	20	2.34	58.5

It can be observed that the extent of recovery was decreasing with an increase in the amount of benzaldehyde added to the mixture. This was attributed to the fact that the increased amount of BD reduced the size of the particles to around 5nm and under. The separation of these particles using centrifugation was very difficult since particles remained in suspension and even stuck to the walls of the tubes. It was therefore easier to recover larger particles as compared to smaller particles when centrifugation was used as a final step to get the highly crystalline magnetite nanoparticles from solution. This is because the smaller catalyst particles were lighter and remained suspended in the ethanol/dichloromethane washing solvents.

4.1.2 Results of the preparation of iron carbide nanocatalysts:

Iron carbide, (cementite, Fe_3C) catalysts were successfully prepared using all the three (3) biopolymer routes followed by a thermal degradation step which ensured that all the hydroxides were transformed to the carbide phase. It was noted that the iron carbide nanocatalysts prepared from gelatine had slightly larger particle sizes as confirmed by Transmission electron microscopy (TEM) images shown in **section 4.3.2**. The reason for these bigger particle sizes was assumed to have been due to the more viscous gelatine solution compared to the other two prepared biopolymers. The solution seemed to have a much greater grip on the nanoparticles compared to the other biopolymers. The yield of particles obtained after the calcination stage was however more for the gelatine route than for ammonium alginate or chitosan routes. This was due to the fact that chitosan and ammonium alginate decompose more than gelatine when exposed to very high temperatures of above 600 ^{0}C. The thin brown films/gels that were obtained after the drying stage were not magnetic as they were still iron hydroxides. Figure 4.2 below shows a photograph of the dried film before calcination.

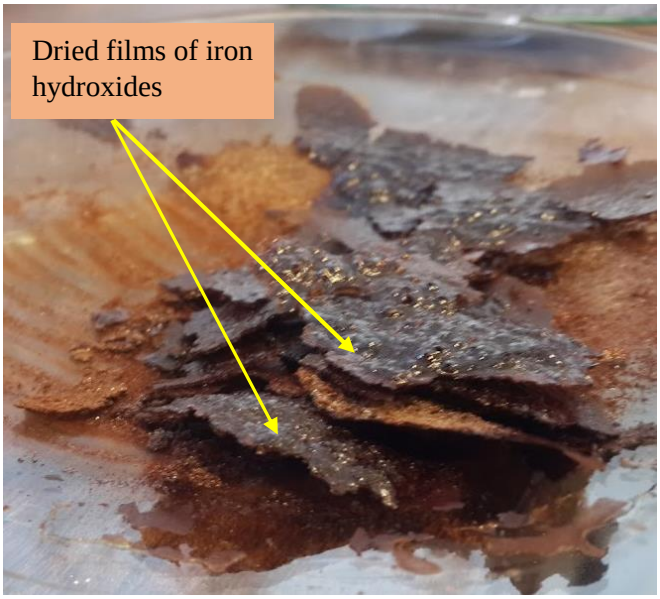

Figure 4. 2: Picture of Iron hydroxide films obtained after drying for 24 hours at 50 ^{0}C.

As expected, it was only after calcination that all the iron hydroxide samples started to depict magnetic behaviour (Schnepp et al., 2010) as they were converted to cementite and other carbides which were confirmed by PXRD measurements. Magnetic properties of the nanocatalysts are very important since they help in the separation of the particles from the slurry after the reaction. To closely control the particle size distribution of the particles, small batches were also synthesised.

4.2 SEM results:

After a few batches of both the magnetite and iron carbide nanocatalysts were prepared, samples were characterised to better understand their morphology, particle size and phases of the nanoparticles. Particles were initially exposed to Scanning electron microscopy which provided comprehensive 2 – dimensional information of the catalysts.

4.2.1 SEM results for magnetite nanocatalysts:

The dry synthesised nanosized magnetite catalysts were viewed under a scanning electron microscope (SEM) to ascertain the structure, surface topography and morphology of the particles. Figure 4.3 below shows images of the particles as viewed under high resolutions.

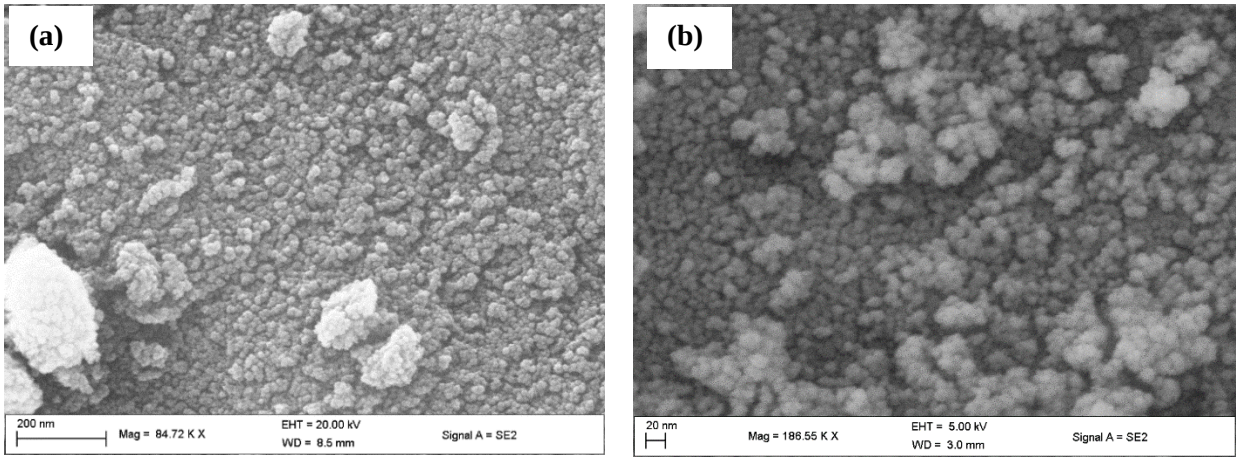

Figure 4. 3: Scanning Electron Microscopy (SEM) images of magnetite catalysts at magnifications of (a) - 84.72KX and (b) - 188.55KX.

From the images shown above it is clear that most of the particles were discrete and spherical, but there were also lumps of nanocatalysts as can be observed on image (a) on the left. Results from transmission electron microscopy (TEM) also proved that particles were spherical with particle sizes ranging from 7-15nm. Some of the particles seem to be agglomerated owing to the fact that they were not calcined to remove all residual solvents and hence traces of the solvents were still present in the samples. Calcination was avoided to prevent phase changes on the as-synthesised nanocatalysts.

4.2.2 SEM results for iron carbide nanocatalysts:

Iron carbide (Fe_3C) samples were also viewed under the same scanning electron microscope using the same conditions. Nanocatalysts were clearly observed to be imbedded in a carbon-nitrogen biopolymer matrix as shown by the micrographs in figure 4.4 below. The gelatin matrix seemed to hold the particles more closely than the other 2 biopolymers, namely chitosan and ammonium alginate. This can be attributed to the molecular interactions in these different biopolymers as well as their thermal stability under inert environments. Chitosan is known to remain thermally stable up to a temperature of 329 ^{0}C (Schnepp et al., 2010). Iron carbide particles from ammonium alginate and chitosan seemed to be held to almost the same degree by the biopolymer matrix. This further confirms why these two polymers have similar thermal decomposition patterns as reported by (Schnepp et al., 2010) from their stability tests using Thermal Gravimetric Analysis (TGA).

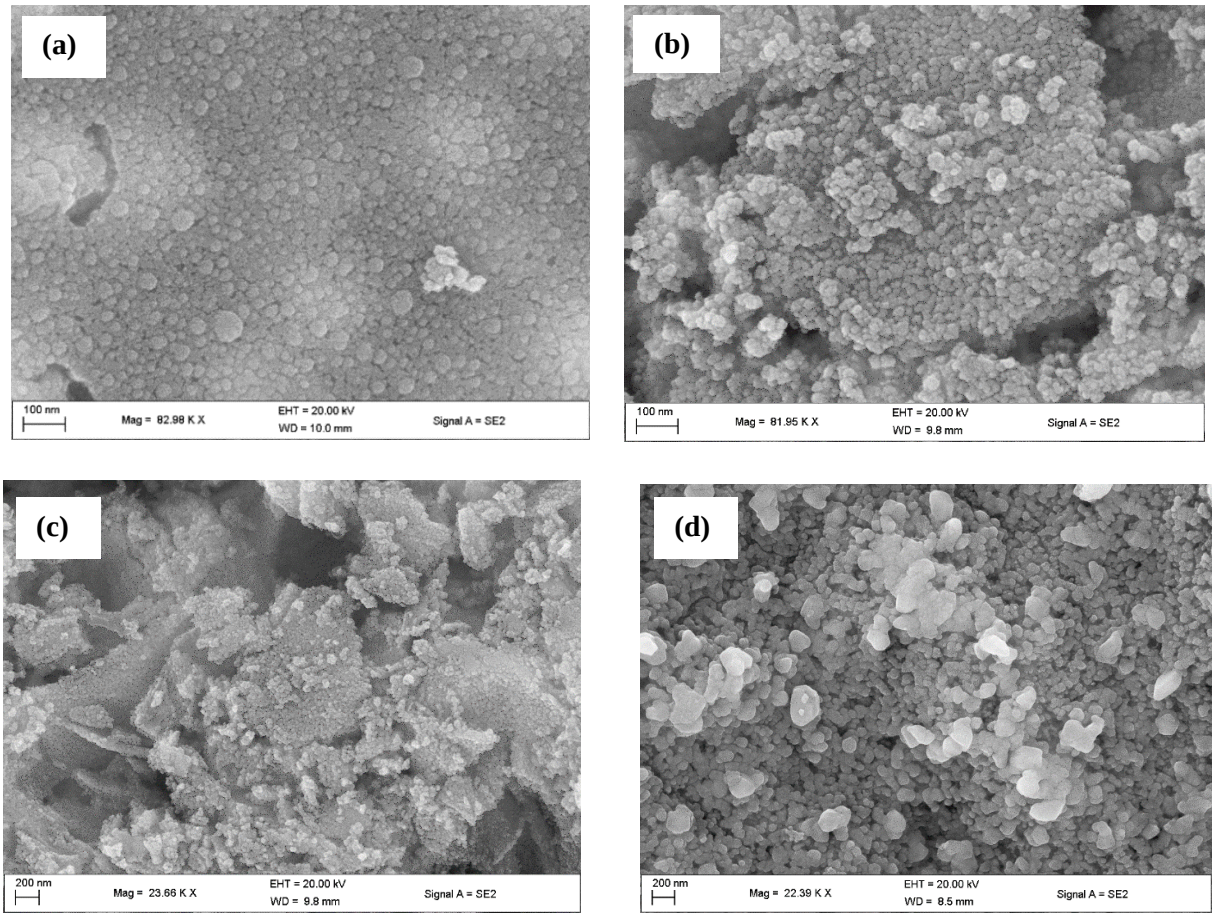

Figure 4. 4: SEM micrographs of iron carbide nanocatalysts prepared using using the three (3) biopolymer routes. **(a)** – Gelatine route, **(b)** – Ammonium alginate route, **(c)** and **(d)** – Ammonium alginate and chitosan routes respectively but at a lower magnification.

It was important that the particle size distribution of these iron carbide nanocatalysts resemble that of the magnetite nanocatalysts since mixtures must have almost the same sizes of catalysts. It was therefore imperative to study and compare the particle sizes and morphology of the iron carbides and magnetite nanocatalysts. Figure 4.5 below shows the side by side micrographs of magnetite **(a)** and iron carbide **(b)** both at nearly the same level of magnification as shown by the scale bar. The two micrographs show that particles were of a similar particle size, having those iron carbide based on alginate route being slightly larger than the magnetite nanocatalysts. This was also confirmed by TEM analysis results and discussed in section 4.3.2 below.

It was also essential that the iron carbide nanoparticles obtained from the three (3) biopolymer routes be of almost the same particle size and size distributions.

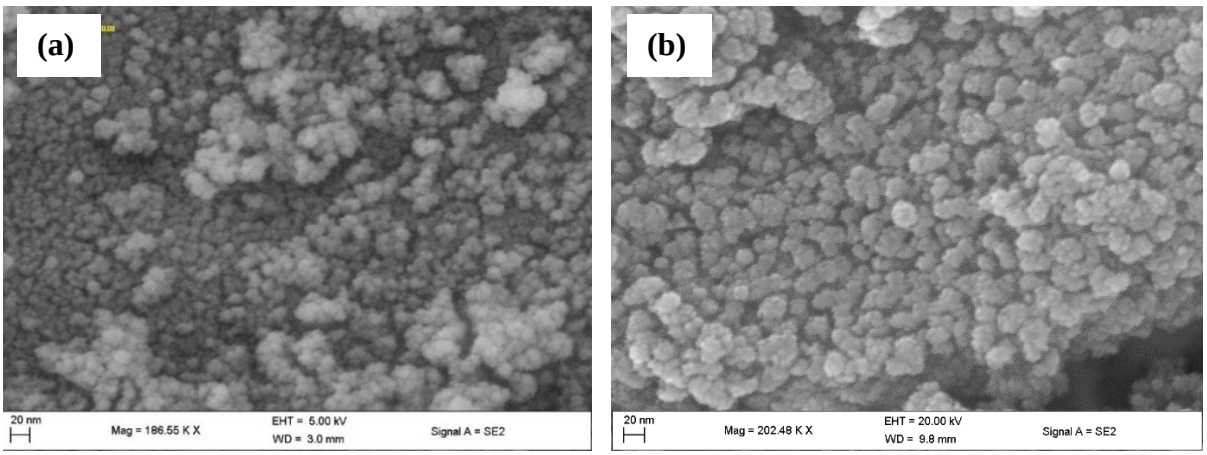

Figure 4. 5: Magnetite and iron carbide nanocatalysts nanoparticles compared: **(a)** – Magnetite micrograph, **(b)** – Iron carbide micrograph.

The morphology and particle shape was expected to be similar since all of them were to be mixed to form one (1) catalysts mixture. It was therefore important that they have the same sphericity as it is an important parameter if particles are to form an almost homogeneous mixture for use in slurry phase FTS. Figure 4.6 shows a side by side comparison of two (2) micrographs for iron carbide nanocatalysts prepared by: **(a)** – the ammonium alginate route and **(b)** – the chitosan route. It can be observed that the nanoparticles were almost of the same size with the chitosan based only slightly larger possibly due to agglomeration. Their biopolymer matrices can be seen surrounding the nanoparticles as expected. These observations were also confirmed by TEM results as discussed in section 4.3.2.

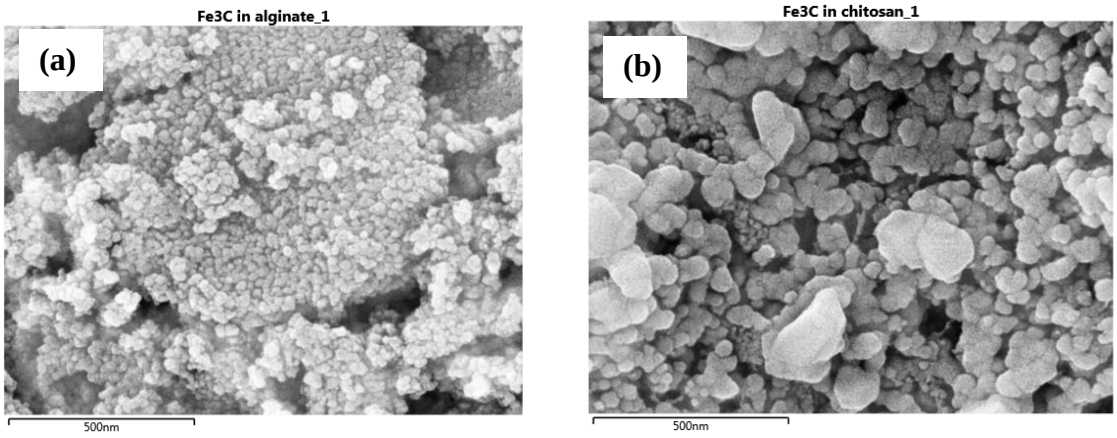

Figure 4. 6: iron carbide nanocatalysts micrographs for samples prepared by: **(a)** – Ammonium alginate route, **(b)** – chitosan routes.

4.2.3 SEM-EDX results for magnetite:

After the morphology and surface topography of the particles was ascertained, the elemental distribution of the constituent elements in the nanocatalysts was analysed. Elemental composition of all the samples of magnetite catalysts was done using Energy Dispersive X-ray spectroscopy analysis (EDX). The technique was used here only as a qualitative tool to identify and confirm the presence of the elements that were expected in the chemical makeup of the particles. The percentage composition of these elements when measured by EDX analysis is sometimes not as accurate as the actual catalyst compositions and hence phase composition was confirmed by PXRD analyses. Figure 4.7 below shows the approximate iron and oxygen concentrations in the analysed samples of magnetite. Elemental mapping showed that the samples were composed of mainly Fe and O in the dried magnetite catalyst samples. The results agree to a larger extent with Powder X-ray Diffraction (PXRD) results as presented in section 4.4.1. The given spectra in **figure 4.7** shows the percentage compositions of the two (2) elements which give an overall molar composition of three (3) moles of iron to four (4) moles of oxygen. This gives a formula of Fe_3O_4 which is magnetite.

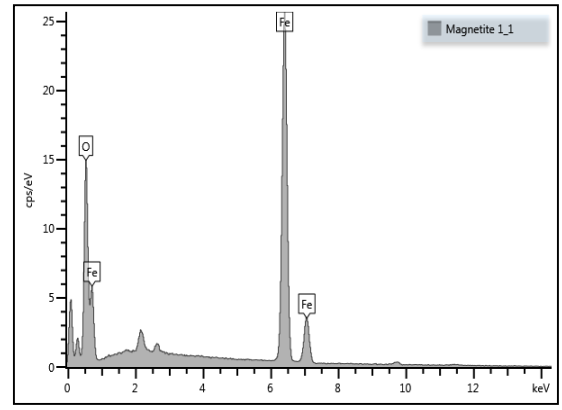

Magnetite 1_1	Wt.%	Wt.% Sigma
O	27.58	0.24
Fe	72.42	0.24
Total	100.00	

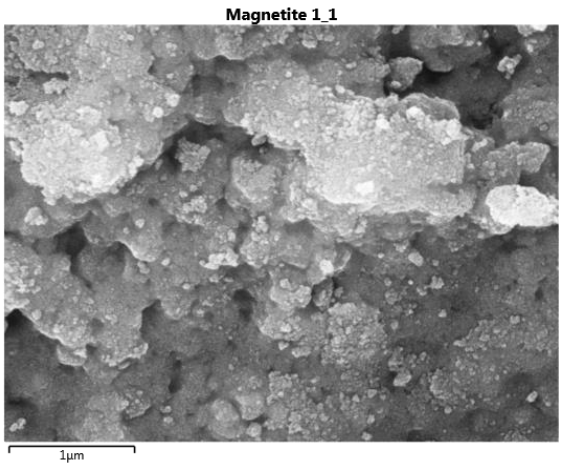

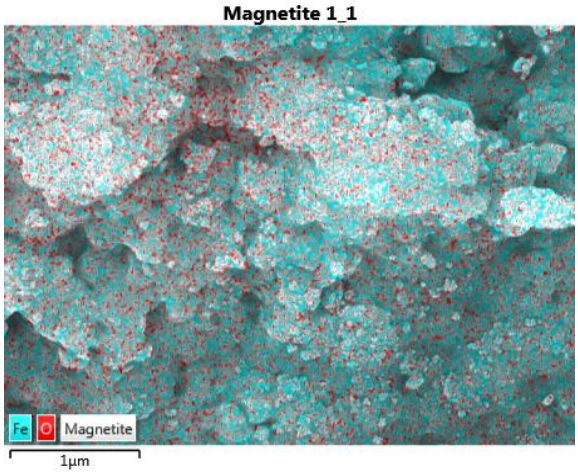

Figure 4. 7: SEM – EDX mapping of a magnetite sample showing the distribution of iron and oxygen.

Though the accuracy in quantification of elemental composition using EXD technique is highly questionable, the quantities of iron and oxygen obtained provided an insight about the presence of these main elements in the sample. Some small unlabelled peaks of gold were detected and are shown on the spectra as well. These were due to the small amount of gold that was sprayed on top of all the samples to make them conductive. The composition of all magnetite samples that were analysed showed an almost equal composition in terms of the amount of iron and oxygen. **Figure 4.8** shows an EDX sample mapping that is almost similar in terms of composition of elements. The micrographs are however at half the magnification of the above magnetite sample to ascertain the uniformity of the samples.

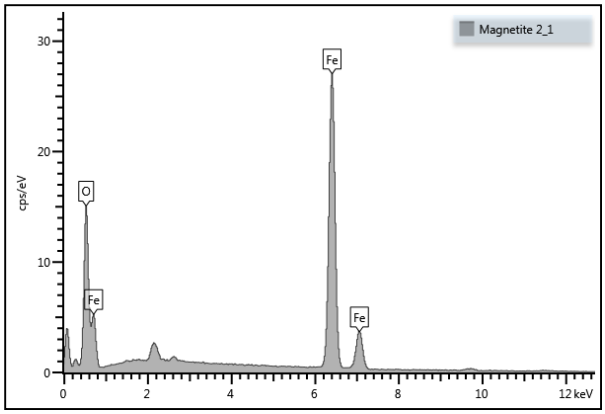

Magnetite 1_2	Wt.%	Wt.% Sigma
O	26.39	0.23
Fe	73.61	0.23
Total	100.00	

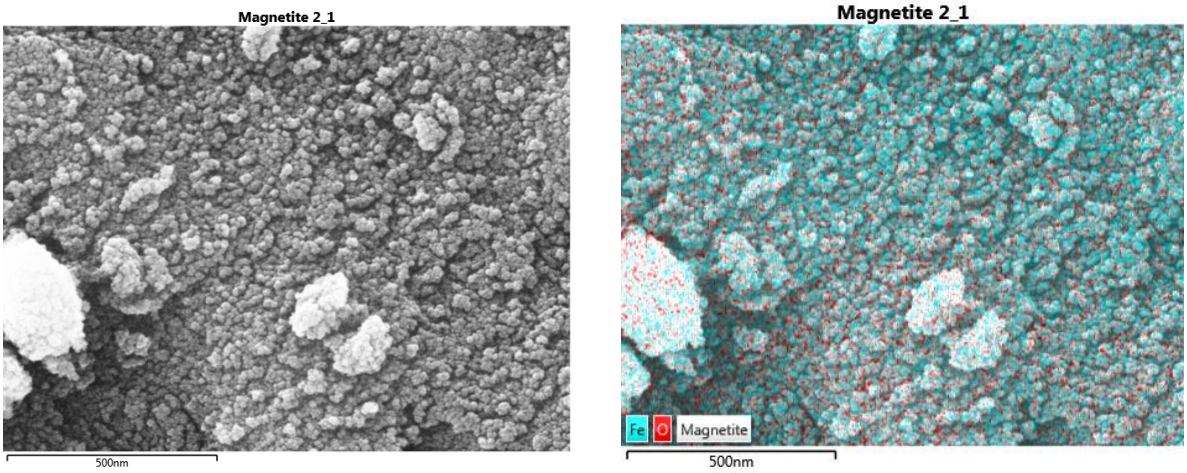

Figure 4. 8: SEM – EDX mapping of another magnetite sample showing the elemental distribution of iron and oxygen in prepared catalysts.

4.2.4 SEM EDX results for iron carbides:

Iron carbide nanoparticles were also analysed using EDX elemental analysis and the average levels of the detected carbon was about (17 – 26) wt. % for most of the samples. This did not tally with any of the iron carbide phases that are so far known to be thermally stable at ambient conditions. It also suggested that besides the main elements, carbon and iron, there were also traces of some elements such as nitrogen which remained entrapped after the thermal degradation of the biopolymers. When (Schnepp et al., 2010) synthesised iron carbide nanoparticles using this same method, they observed that some amorphous carbon constituted a significant part of the total carbon content. It was left in the sample as a side product and the rest was carbon that was encapsulated in the cementite lattice. Stoichiometrically pure Fe_3C should contain about 6.7% of carbon by mass. This meant that the actual content of pure Fe_3C was estimated to be around 78% (Schnepp et al., 2010) by mass of the whole sample. The scanning electron microscopy (SEM) images shown in figure 4.4 shows the structure of the dried and calcined iron carbide film as being composed of a homogeneous network of nanocatalysts particles interspaced in the thermally decomposed biopolymer. This

nanoparticulate structure was further confirmed using transmission electron microscopy (TEM) as shown in **figure 4.13** below.

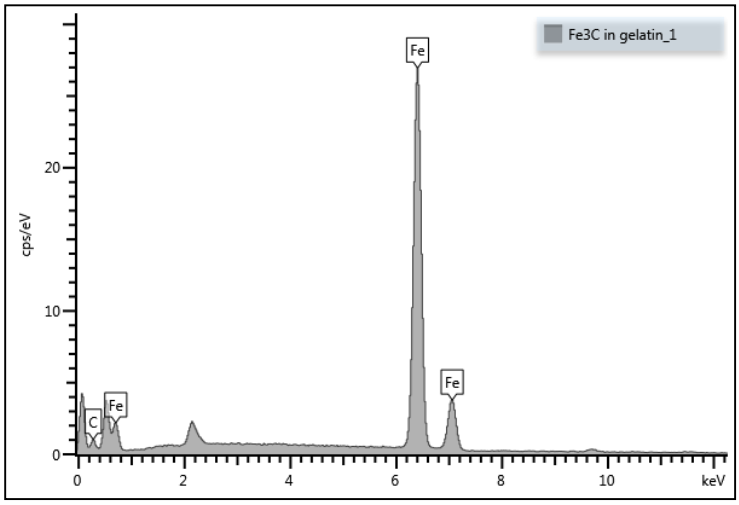

Fe_3C in gelatin	Wt.%	Wt.% Sigma
C	17.38	0.75
Fe	82.62	0.75
Total	100.00	

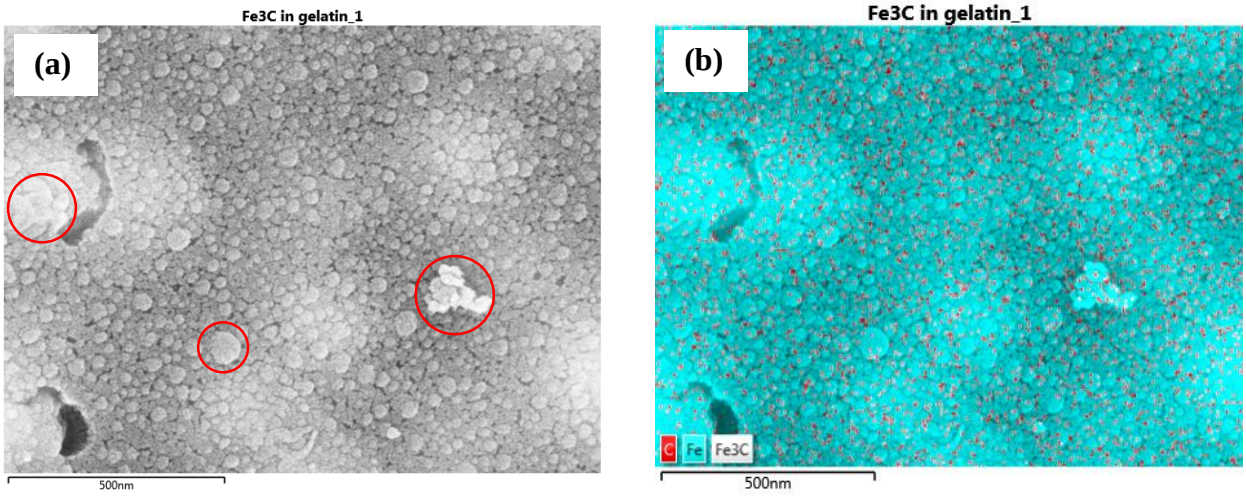

Figure 4. 9: SEM – EDX mapping for iron carbide nanocatalysts prepared via the gelatin route showing the elemental composition and distribution of iron and carbon.

The structural morphology depicted on figure 4.9 **(a)** shows that the iron carbide nanoparticles were smooth spherical particles well dispersed in the carbon network. Particles looked almost of the same size except for a few particles which were somehow agglomerated. On the spectrum, notably no large peaks of nitrogen were observed at almost all the magnifications that were used. This also confirmed that the carbide particles were uniformly distributed in the matrix in agreement with the XRD data. The EDX mapping image (a) shown on the right also shows an even dispersion of both iron (green) and carbon (red) in the sample. Even those particles which were agglomerated showed that they were composed of an even distribution of carbon and iron. The agglomerated particles are shown circled in **figure 4.9** above. The cause of this agglomeration could be as a result of bulk iron carbide forming in the decomposing matrix during the calcination. Some

iron carbide nanocatalysts had a little bit more carbon content at 26.97% and this can be attributed to the differences in the nature of the biopolymers used. Looking at the whole sample scan of the iron carbide catalyst synthesised using alginate as the biopolymer, the average composition of iron and carbon is almost uniform throughout the sample as shown in **figure 4.10** below. The uniformly dispersed red spots represent carbon. Although this technique does not give us an absolute percentage of the elements present, the relative composition for this catalyst was however approximated.

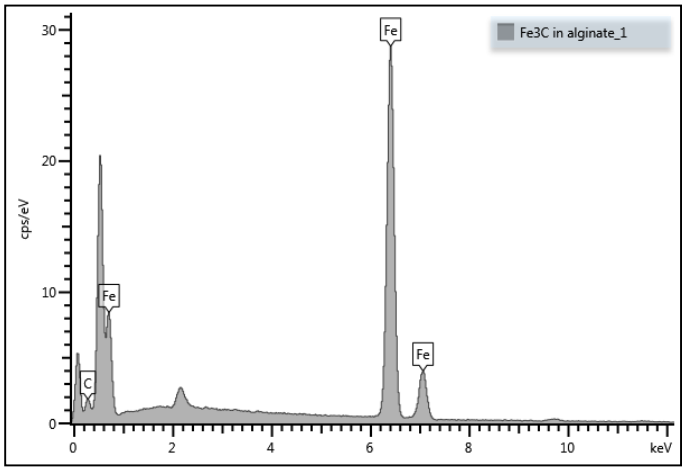

Fe_3C in alginate_1	**Wt%**	**Wt% Sigma**
C	26.97	0.74
Fe	73.03	0.74
Total	100.00	

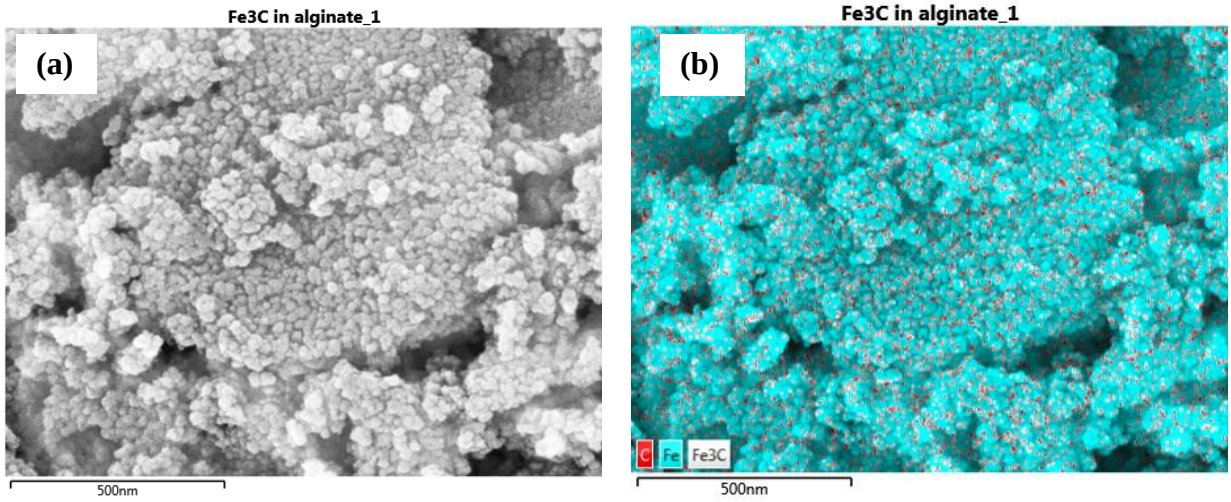

Figure 4. 10: EDX mapping for iron carbide nanocatalysts synthesized using ammonium alginate, showing the elemental distribution of iron (green) and carbon (red) on image **(b)**. Image **(a)** show the morphological structure of the nanocatalysts at a lower magnification.

4.3 TEM results:

Results obtained from transmission electron microscopy were of utmost importance since they were used to calculate the particle size and hence the particle size distribution (PSD). The technique gave clear two-dimensional images of the particles as black spots for both magnetite and iron carbide nanoparticles. The images show that the particles were evenly dispersed in the biopolymer media and that the particle size range was so narrow. Particle sizes were also in the nanosized range as also confirmed by the broad XRD peaks that were observed in powder X-ray diffraction measurements.

4.3.1 TEM results for magnetite nanocatalysts:

Transmission electron microscopy (TEM) images show that most of the magnetite (Fe_3O_4) nanocatalysts were well dispersed with a smooth spherical shape and near-uniform sizes ranging from ca. 2.5 nm to 10 nm and a few with sizes up to 16nm. This can be explained in terms of agglomerated nanoparticles which were formed during the time catalysts were drying. It was noticed that the particle size distribution (PSD) becomes broader with the reduced amounts of benzaldehyde. By using a physical magnet, particles were observed to be highly magnetic. **Figure 4.11 (a)** below shows the particles with 20ml of benzaldehyde (BD) in the mixture with benzyl alcohol and **(b)** shows the micrograph of a sample that had 12ml of benzaldehyde.

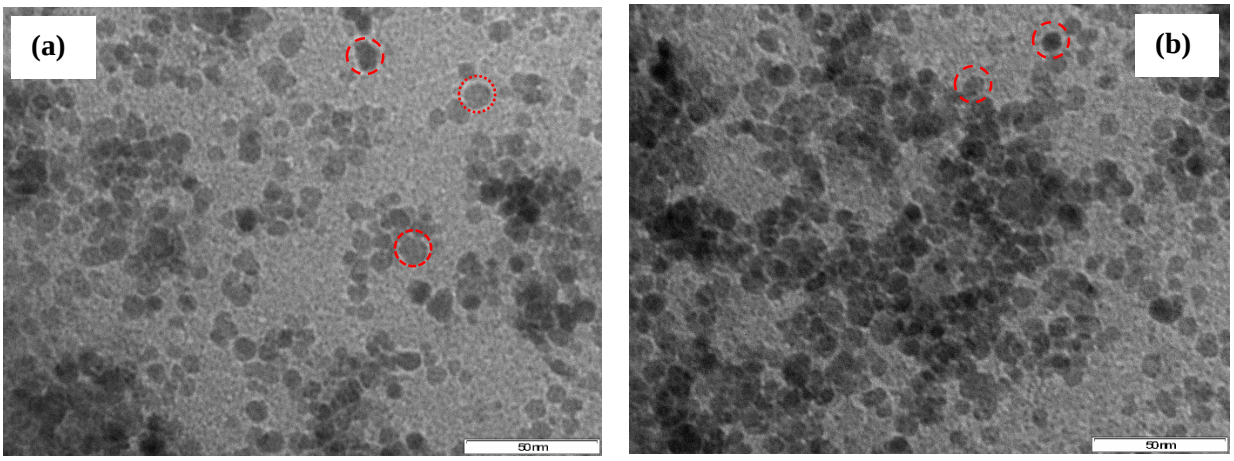

Figure 4. 11: TEM images of two magnetite nanocatalysts samples prepared via the solvothermal synthesis route showing the **(a)** sample prepared using 20ml of benzaldehyde and **(b)** sample prepared using 12ml of benzaldehyde.

The particles that were synthesised using 12 ml of BD can clearly be seen to be slightly larger than those obtained when 20 ml of BD was used. This confirms that benzaldehyde is a good capping agent in the modified solvothermal synthesis route for preparing highly crystalline magnetite nanocatalysts. The particle

size distribution shown in **figure 4.12** below depict the variation of the particle size diameters as determined by measurements using iTEM® image processing software. The mean particle sizes are almost similar for both samples. A mean particle size of 7.58 nm was obtained for sample **(a)** and 7.54 nm for sample **(b)**.

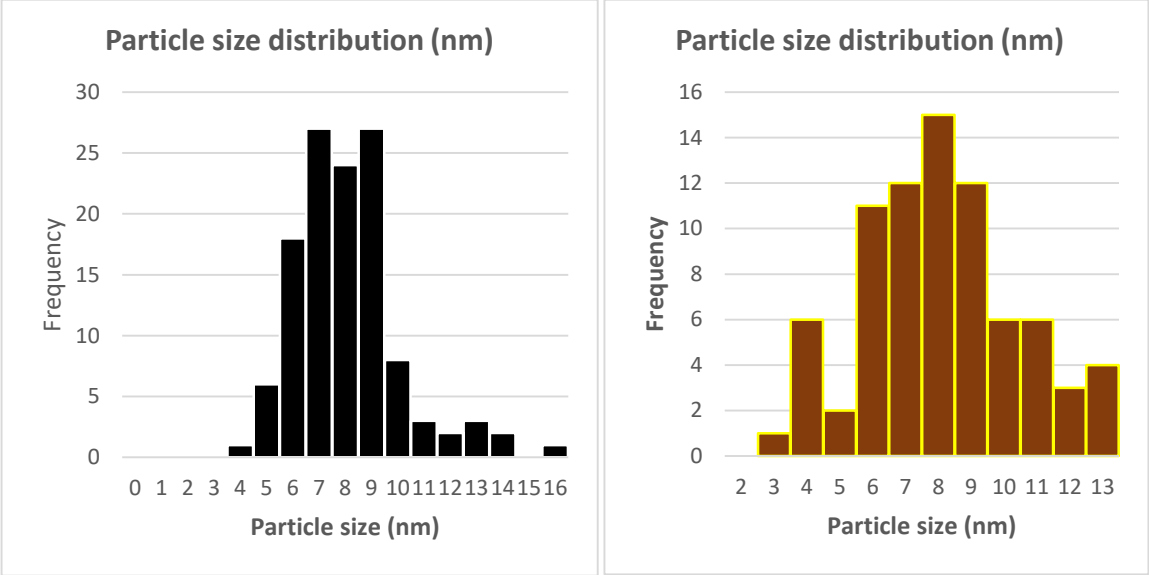

Figure 4. 12: Particle size distribution of crystalline magnetite nanoparticles prepared using a modified solvothermal synthesis route.

4.3.2 TEM results for Iron carbide nanocatalysts:

Iron carbide nanoparticles were also characterised using transmission electron microscopy and the images shown in figure 4.13 show the micrographs for the samples analysed.

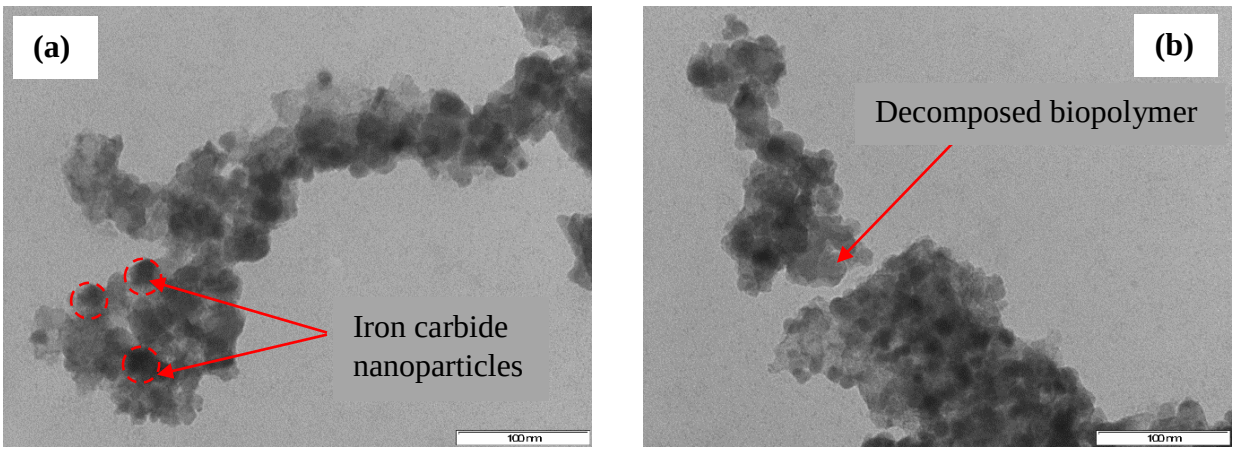

Figure 4. 13: TEM micrographs of iron carbide nanoparticles prepared using the Ammonium alginate biopolymer route.

All the nanoparticles that were prepared using the three (3) biopolymer routes were analysed using transmission electron microscopy (TEM) to understand their shape also measure their particle size diameters.

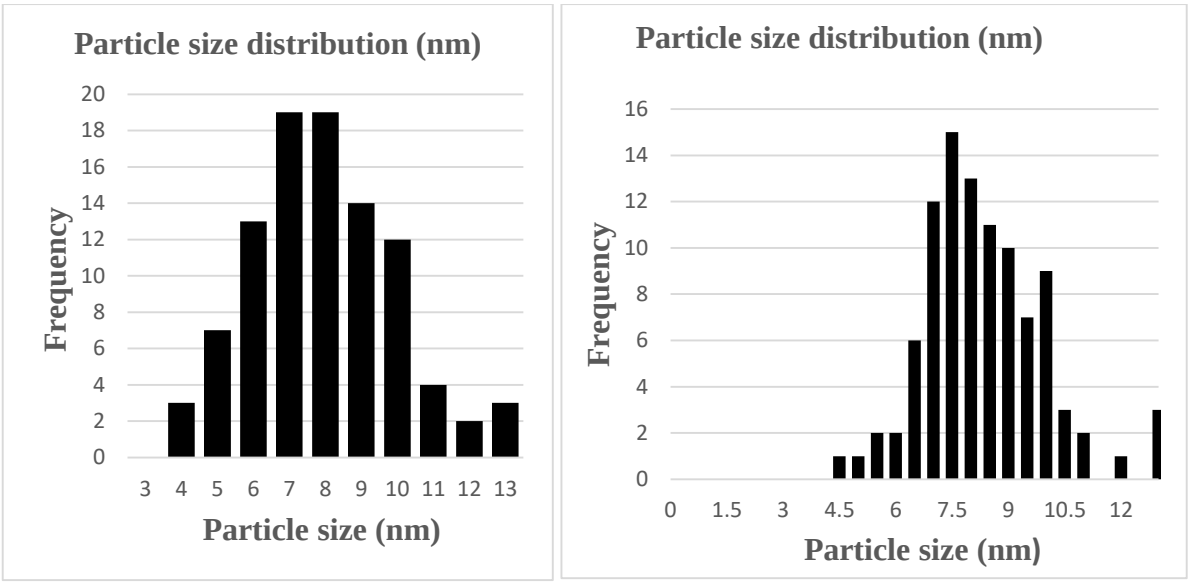

Figure 4. 14: Particle size distribution of iron carbide nanoparticles prepared using the ammonium alginate biopolymer route.

Figures 4.15 to 4.18 show the TEM micrographs of the various samples of iron carbide nanoparticles prepared via the gelatine and chitosan biopolymer routes. The corresponding histograms for the particle size distribution of the nanoparticles are also presented.

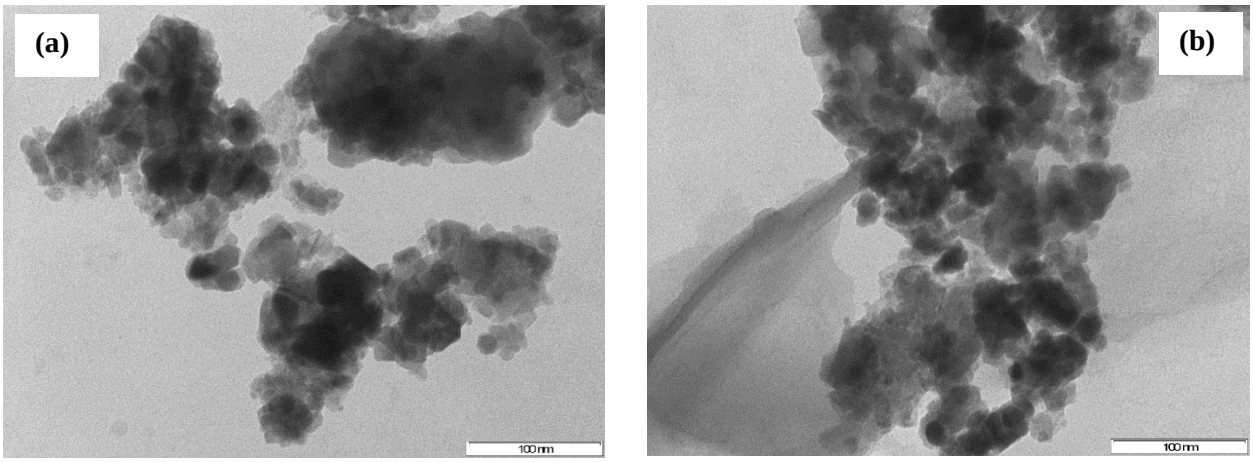

Figure 4. 15: TEM micrographs of iron carbide nanoparticles prepared using the gelatin biopolymer route.

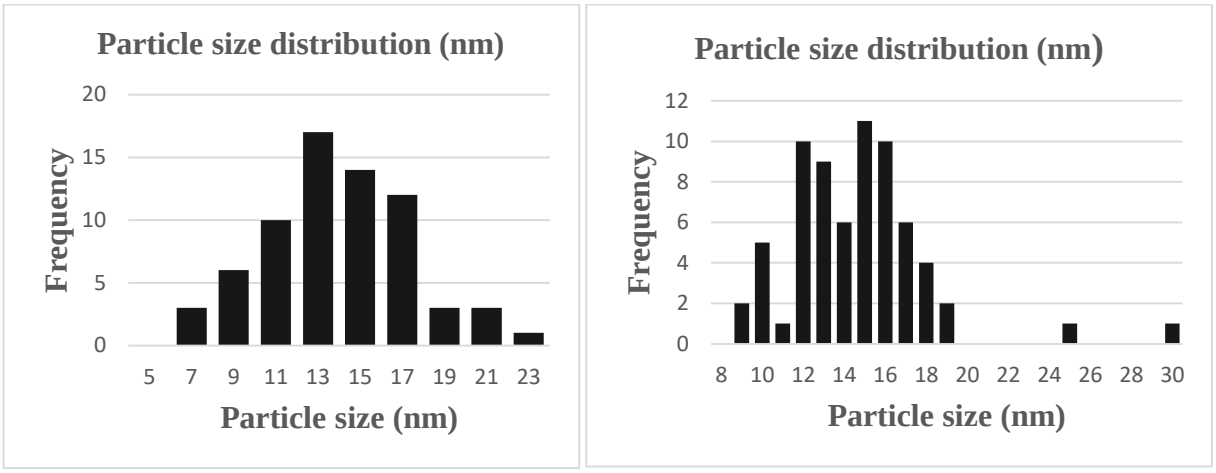

Figure 4. 16: Particle size distribution of iron carbide nanoparticles prepared using the gelatin biopolymer route.

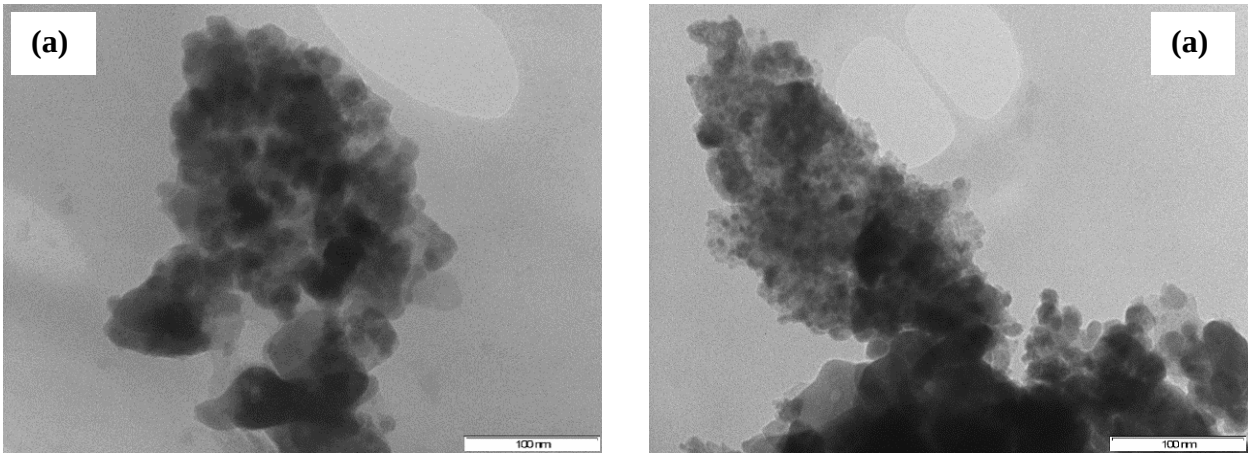

Figure 4. 17: TEM micrographs of iron carbide nanoparticles prepared using the chitosan biopolymer route.

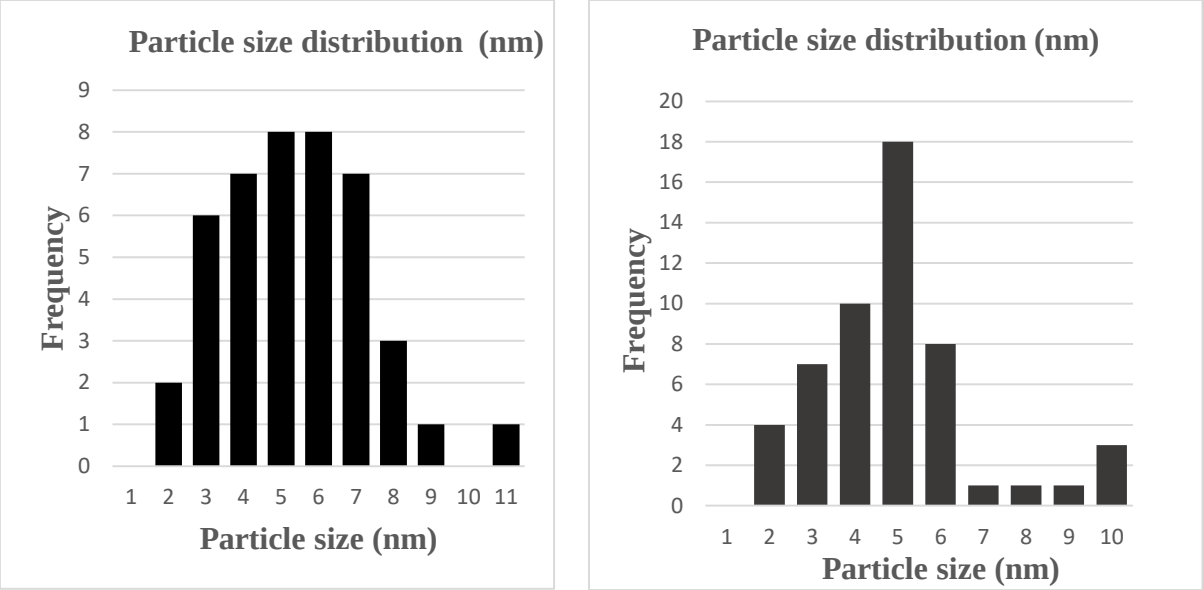

Figure 4. 18: Particle size distribution of iron carbide nanoparticles prepared using the chitosan biopolymer route.

TEM images of the iron carbide nanocatalysts are shown in **figures 4.13** through **4.17** above. Images revealed that nanoparticles were evenly distributed and were almost perfectly spherical. The iron and carbon distribution in the samples was almost uniform for all the three (3) types of catalysts prepared through the different biopolymers routes as confirmed by the EDX mapping. Iron carbide clusters in the TEM images are the dark, dense particles as illustrated on **figure 4.13** above. In electron microscopy the heavier elements appear as dark spots and the surrounding decomposed carbon matrix which is made of lighter elements can be seen surrounding the iron carbide nanoparticles. This observation was supported by SEM analyses (discussed in section 4.2.2 above), which indicated that the decomposed matrix stayed intact around the as-synthesised nanocatalysts. This allowed the particle size and hence the size distribution to be evaluated using these TEM images. The particle size distributions, presented in **figure 4.14, 4.16 and 4.18** above were determined by measuring about fifty (50) or more iron carbide crystallites using the iTEM® image analysis software. The size of the gelatine produced iron carbide nanocatalysts were the largest as they were between 6 and 17 nm and some few were as large as 30 nm. It is however interesting to note that almost 85% of the particles were in the range of 6 to 17 nm. The size of the iron carbide nanoparticles prepared via the chitosan biopolymer were between 2 and 11 nm with 95% of the particles in the range of 2 to 9 nm. The average particle size for the chitosan and ammonium alginate-based iron carbide nanocatalysts were estimated to be 13.71 nm and 12.72 nm respectively. The larger iron carbide particles were ultimately mixed with the other catalyst particles in the Fisher-Tropsch reaction experiments. The addition of iron carbide

nanoparticles drastically increased the production of C_{5+} hydrocarbon, thus improving the chain growth probability factor.

4.4 XRD results:

After the morphology of the particles and their corresponding particle sizes and size distribution was ascertained, the determination of the catalysts phases was essential. This was achieved with Powder X-ray diffraction on a on a Malvern Panalytical's X-ray Diffractometer with a Co-Kα radiation source. Samples were analysed separately before mixing.

4.4.1 XRD results for magnetite nanocatalysts:

The PXRD results presented in **Figure 4.19** and **Table 4.2** gives representative spectra and peak table respectively for the magnetite catalysts samples for all the different catalysts samples that were analysed. The XRD analyses show the broadness and intensity of the main peaks of the magnetite nanoparticles. The magnetite peaks were all identified using Xpert Highscore and they were refined and matched using Rietveld refinement. Particles were highly crystalline as deduced from the sharpness and clarity of the peaks produced as shown in figure 4.19 below.

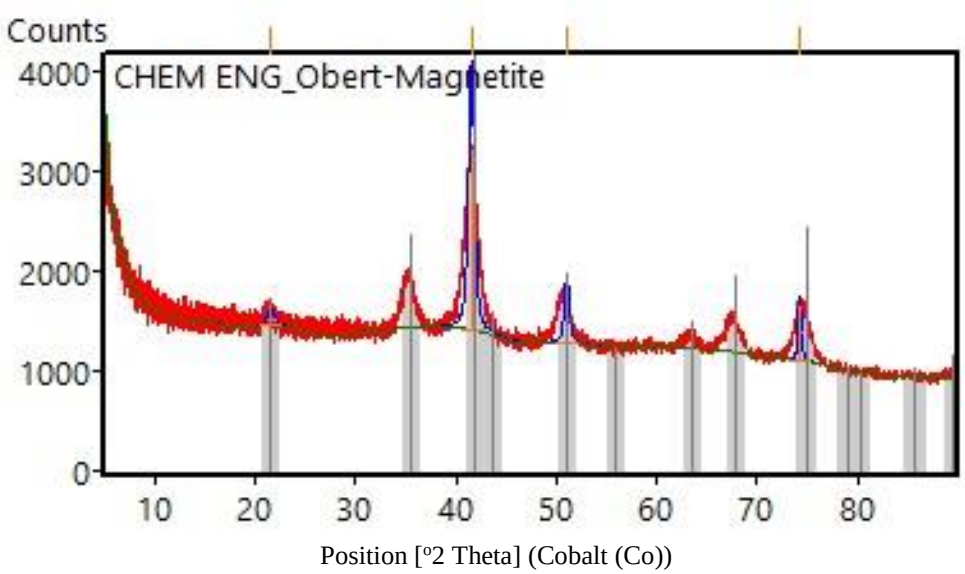

Figure 4. 19: PXRD spectra of highly crystalline magnetite nanoparticles prepared through the modified solvothermal synthesis route.

Table 4. 2: Magnetite XRD peak list.

Peak List

Pos.[°2Th.]	Height [cts]	FWHMLeft[°2Th.]	d-spacing [Å]	Rel. Int. [%]
21.5118	118.38	0.8817	4.79652	6.37
41.5028	1858.24	0.6927	2.52644	100.00
50.9968	490.63	0.5038	2.07940	26.40

The peak structure on the magnetite spectra was not similar to that of iron carbide nanoparticles as these had some amorphous biopolymer remains from the thermal degradation step. Broader peaks were observed on magnetite spectra suggesting that magnetite particles were slightly smaller than the iron carbide nanoparticles. This agrees well with data obtained from both SEM and TEM analyses as shown in the calculated particle size distributions for all the nanoparticles (Figures 4.14 – 4.16). This suggests that the presence of biopolymers in the synthesis of iron carbide nanoparticles resulted in the successful control of catalysts particle sizes. It resulted in the particles being ideal for making catalysts mixtures as intended in this work. Particles are not supposed to have a wide particle size range for them to work as effective catalysts.

4.4.2 XRD results for iron carbide nanocatalysts:

The crystallinity of iron carbide nanocatalysts prepared using alginate was more defined as compared to those particles prepared using gelatine or chitosan as the biopolymer.

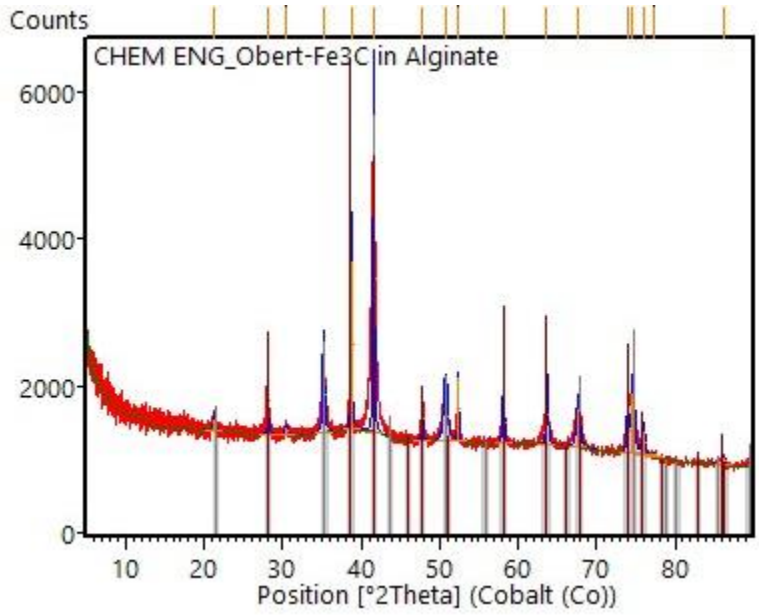

Figure 4. 20: XRD spectra of Iron carbide nanoparticles prepared via the Ammonium alginate biopolymer route.

The XRD spectra for iron carbide nanoparticles prepared using this biopolymer has well defined peaks as shown in **figure 4.20** above. This resulted in the use of ammonium alginate more often as the polymer of choice in the preparation of iron carbide nanoparticles which were used in the preparation of catalysts mixtures tested in this work.

The peaks that were observed from powder X-ray diffraction spectra (XRD) analyses for the magnetite show peaks at positions with Miller indices (h k l) given to the 111, 113, 004 and 044 crystal planes of Magnetite. Prominent peaks due to iron carbide were noticed at 2θ values of 28.1°, 35.3°, 38.6°, 41.6°, 44.1° and 53° for all the samples synthesised using biopolymers. Interesting to note was the fact that the magnetite had a major peak at almost the same value as with the iron carbide nanocatalysts. Initially it was not clear whether this peak at a 2θ value of 41.6^{o} in carbides was a magnetite peak or was common to both cementite and magnetite. With the first batch of prepared samples, it was assumed that some of the iron carbide nanoparticles were oxidised to magnetite during or soon after the calcination stage. This was considered possible since the calcined samples were removed from the oven whilst still very hot. Hot catalysts particles were transferred from the furnace tube to glass flasks which were immediately sealed. This was however done in an air environment and hence making room for aerial oxidation. The handling of the second batch of catalysts and all the other syntheses that followed made use of an inert atmosphere soon after calcination. An inert nitrogen environment around the furnace to prevent further particle oxidation was utilized.

Figure 4. 21: Closed flask for storing freshly calcined iron carbide nanocatalysts films soon after calcination up to 650 ^{o}C in a nitrogen environment.

After this was done, it was noticed that the appearance of the peak at 41.6^{o} persisted and using Xpert Highscore coupled with Rietveld refinement, it was identified to be largely as a result of cementite (Fe_3C) and a few other carbides in the samples. This agreed well with data obtained by (Schnepp et al., 2010). The stacked 2-Dimensional XRD spectra shown in figure 4.22 below illustrates the major peaks that were observed using magnetite and three (3) samples of iron carbide nanocatalysts. What is clear on these spectra is that the peak broadness of the iron carbide samples decreased when compared to that of magnetite. This implied a slightly increase in particle size on the iron carbide nanocatalysts. This is in agreement with what was observed in TEM particle size analyses using iTEM®. Calculated volume weighed diameters using the Scherrer equation also confirmed this increased particle sizes in carbides. However, particle size results obtained from the Scherrer equation were not in agreement with this and were not reliable as they were not constant.

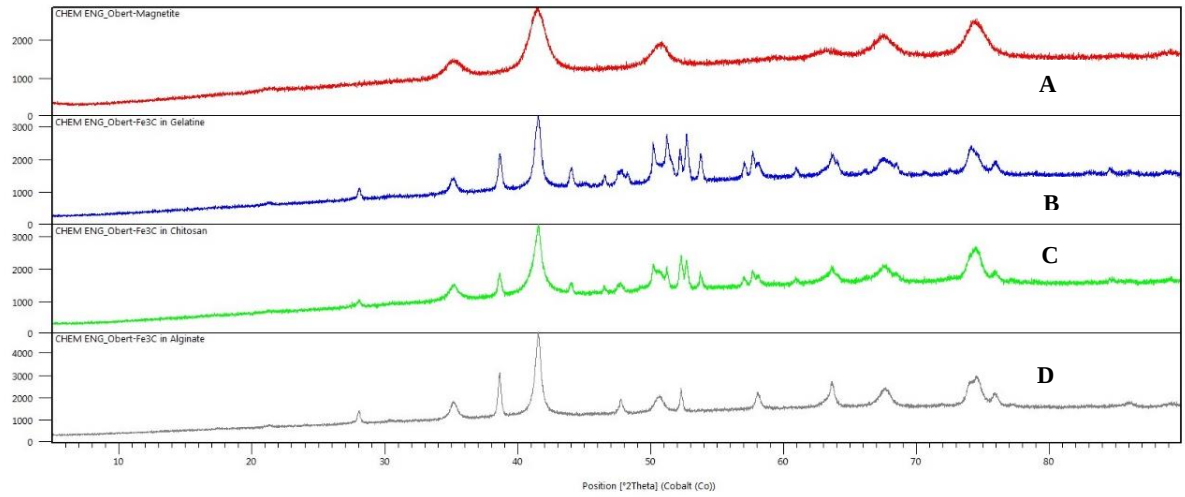

Figure 4. 22: Stacked 2 – dimensional spectra of for magnetite and iron carbide nanocatalysts samples analysed with a Co-Kα radiation source: **A** – Magnetite, **B** – Iron carbide in gelatine, **C** – iron carbide in chitosan and **D** – iron carbide in ammonium alginate.

The superimposition of peaks in **figure 4.23** below depicts clearly that there were mainly two (2) dominant phases that were present in these four samples of nanocatalysts. Magnetite (Fe_3O_4) and iron carbide (Fe_3C) which was identified as cohenite in other samples were the 2 mostly abundant phases in the nanoparticles.

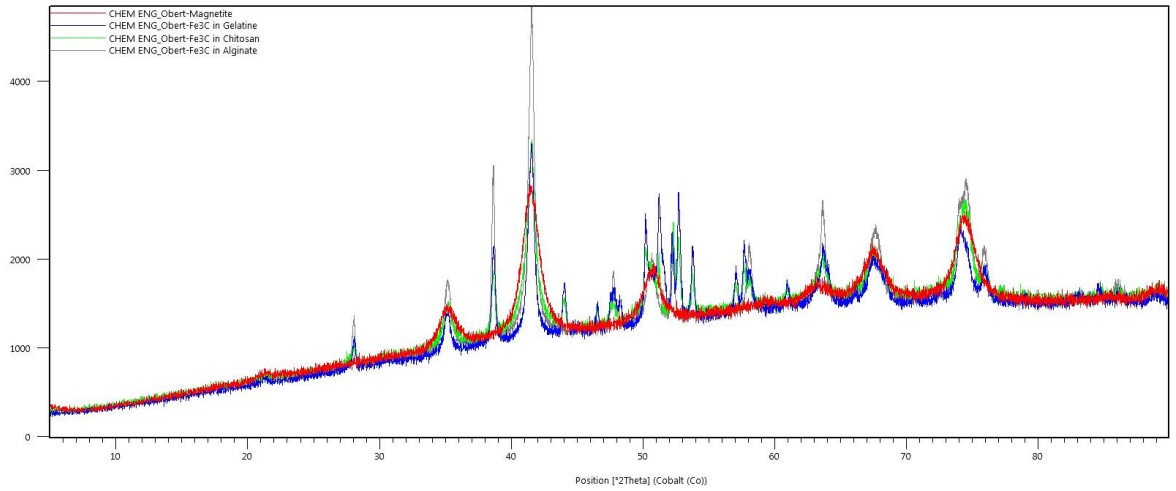

Figure 4. 23: Superimposed magnetite and three (3) iron carbides (cementite) XRD spectra prepared through three different biopolymer routes.

Rietveld refinement showed that some of the samples of iron carbide had also been partially oxidised to magnetite and hematite as shown by the intensities of the peaks at 41.6º in the **figures 4.24 and 4.25 below.**

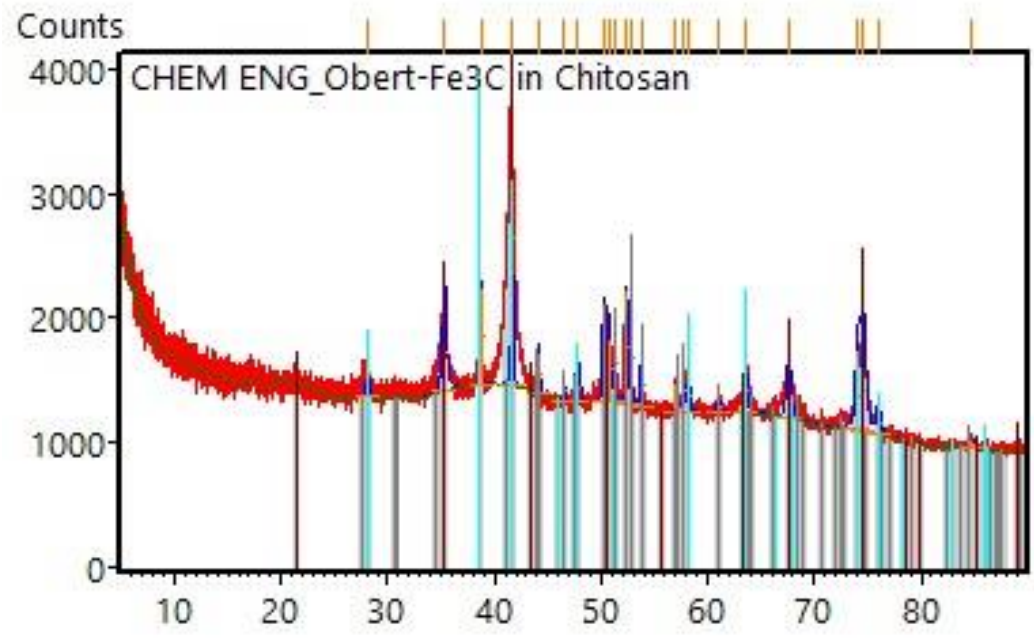

Figure 4. 24: Rietveld refined XRD spectra of samples of iron carbide in chitosan nanoparticles that were prepared without using an inert nitrogen environment.

The extent of oxidation was above 60% for the nanocatalysts that were prepared without preventing aerial oxidation. **Table 4.3** below shows the percentage composition of the three (3) major phases that were detected.

Table 4. 3: Fresh iron carbide nanoparticle phase composition after exposure to air.

Date: 2018/05/23 Time: 11:15:21 File: CHEM ENG_Obert-Fe3C in Chitosan User: 216076162

No.	Visi...	Ref. Code	Compound Name	Chemical Formula	Score	SemiQuant [%]	Display Color
1	☑	98-003-8308	Cohenite	C1 Fe3	62	31	Gray
2	☑	98-015-8743	Magnetite	Fe3 O4	63	34	Maroon
3	☑	98-008-2134	Hematite	Fe2 O3	66	35	Aqua

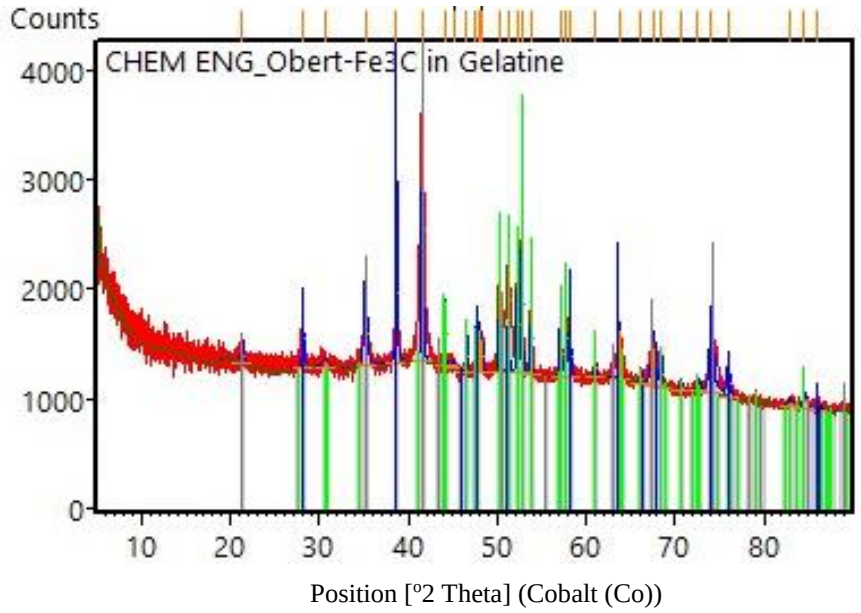

Figure 4. 25: Rietveld refined XRD spectra of samples of iron carbide in chitosan nanoparticles that were prepared without using an inert nitrogen environment.

4.4.3 Particle size comparison:

In order to come to a modest conclusion with regards to the particle size and size distribution of both the magnetite and iron carbide nanocatalysts, comparison of size characterization techniques was done. Particle sizes obtained from TEM imaging were compared with results obtained from XRD full width at half maximum (FWHM) values as calculated using the Scherrer equation. The main reason for the comparison of particle size characterization tools was to obtain the discrepancies and agreements from these two different characterization techniques and hence decide as to whether the desired particle sizes have been

synthesized or not. This was achieved through assessing the level of agreement in the two values calculated using the different methods.

Table 4. 4: Comparison of the different characterisation techniques XRD FWHM (nm).

Type of catalyst	TEM (nm)	FWHM (nm)
Magnetite	7.56	20.27
Iron carbide by Gelatin route	13.54	34.31
Iron carbide by Chitosan route	13.22	40.12
Iron carbide by Alginate route	7.75	28.59

Table 4.4 shows the correlation in the average volume-based catalysts crystallite sizes obtained from the two different characterization techniques. It is clear that the level of agreement in the resulting values from these techniques was not what was expected, and it implies that the average sizes obtained from the TEM calculations had to be considered feasible and hence represent the crystallite sizes and size distribution reasonably. The abundances of the larger crystallites were very minimal and therefore did not form the majority of the particles making up the catalysts mixtures. This was expected since during drying and calcination, the likelihood of particles agglomerating is high as observed in the TEM and SEM micrographs. The iTEM® particle size results were likely to be the most accurate and reliable because the background noise encountered in XRD analysis could have interfered with particle size calculations. As a result, the conclusion was that since particles had distinct size distributions and that the narrowness of these distributions reflected the desired crystallite sizes closely, it can be stated categorically that the synthesis of four (4) narrowly distributed crystallite sizes has been established. The crystallite sizes obtained by (Schnepp et al., 2010) using the TEM characterization technique, however depicted that (Schnepp et al., synthesized larger crystallites with sizes ranging from (15 – 20 nm) compared to the ones prepared in this work. This similar observation can be made for the magnetite nanocatalysts which were synthesized by (Zheng et al., 2015) which had a minimum particle size diameter of 7 nm as compare to 7.56 nm for this work.

After successfully preparing several batches of both magnetite and iron carbide nanocatalysts, the catalysts were tested for their performance in slurry phase FTS. The hypothesis was that, a mixture of catalysts containing both magnetite and iron carbide nanocatalysts would improve the FT activity and product distribution and selectivity towards long chain compounds.

4.5 Catalyst performance results

The effect of adding Iron carbide nanocatalysts to magnetite on the FTS activity was investigated in a 600ml stainless steel compact slurry phase reactor. The reaction was carried out in the low temperature slurry phase Fischer Tropsch regime at 493K (220 ^{o}C) and a pressure of 20 bar. The iron carbide nanoparticles prepared via the biopolymer route were used to make some of the eight (8) catalysts mixtures that were tested. Mixtures had a constant mass of 4.00 grams containing fresh catalysts ready for testing under industrial FTS conditions. The activity of these catalysts samples was measured by the carbon monoxide conversion that was determined after a period of 48 hours time on stream (TOS). This was done since it was determined through preliminary experiments that the process would have reached steady state conditions and hence ideal for sampling. Before sampling was done, calibration of the thermal conductivity detector was done to ensure correct quantification of the reactants and Fischer-Tropsch products.

4.5.1 Results on GC-TCD calibration:

The thermal conductivity detector calibration was carried out regularly using a standard gas mixture to ensure that the detector response was constantly monitored in the entire quantification process. Table 4.5 below summarises some of the results that were obtained on a particular calibration run. The standard mixture was prepared by Air Products® specifically for this project. The mixture contained six (6) gases with known compositions.

Table 4. 5: Gas chromatography peak table for TCD calibration**.**

Compound name	Area 1	Area 2	Area 3	Ave. Area	Composition
H_2	2219747	2802894	3233725	2752122	41.6
N_2	27490.8	32356.9	40545	33464.2	5.3
CO	102583.7	130892.2	156002.3	129826.1	18.3
CH_4	280763.1	352034.2	417459.2	350085.5	14.6
CO_2	61878.3	68551.4	89900	73443.2	10.6

In table 4.5 above, it should be noted that only five (5) gases were detected since argon was used as a carrier gas in these analyses. The above peak areas and composition were used to calculate the TCD calibration factors for all the five (5) gases using equation 3.3 and **table 4.6** summarises all the calculated calibration factors. Note that since N_2 was used as the internal standard (reference), its calibration factor is 1.

Table 4. 6: Calculated TCD calibration factors for the gases used in gas chromatography.

Gas	Calibration factor ($f_{TCD,i}$)
H_2/ N_2	0.095
CO/ N_2	0.890
CO_2/ N_2	0.911
CH_4/ N_2	0.263
N_2/ N_2	1.000

With these results on TCD calibration, the per pass carbon monoxide conversions for each of the 8 catalysts mixtures was evaluated after a time of stream of 48 hours. Carbon monoxide is consumed in the iron-catalysed Fischer-Tropsch reaction forming various hydrocarbons and chemicals which include alcohols, carbonyls and carboxylic acids. Figure 4.26 shows the CO-conversion as a function of the different catalysts mixtures. At the beginning of the chart, 100% magnetite was used as the base case catalyst mixture. The fresh feed ratio of hydrogen to carbon monoxide was maintained at two (2) for all the experiments and a constant temperature of 220 ^{0}C and a pressure of 20 bars was used.

4.5.2 Carbon monoxide conversion results:

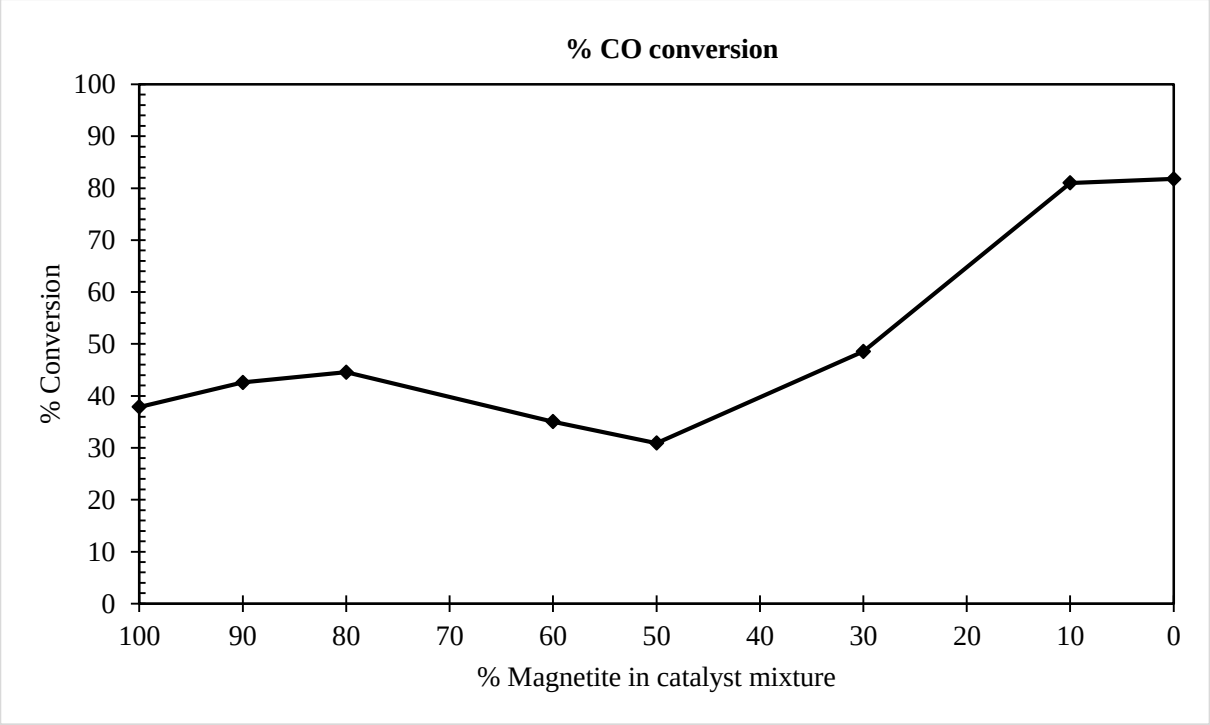

Figure 4. 26: Overall per pass conversion of carbon monoxide as a function of catalysts composition.

As explained earlier in the previous chapter, the analyses were offline, and samples were withdrawn from the FTS testing rig and injected into a Shimadzu 2010 *Plus* gas chromatograph.

A gradual increase of per pass CO-conversion was initially noticed from the 100% pure magnetite catalyst mixture. An increase in conversion from 37.9 % to 42.6% was recorded with the introduction of 10% iron carbide (cementite) in the catalysts mixture. The per-pass CO conversion did not change considerably when the amount of iron carbide was increased to 20%. This can be attributed to the fact that the amount of the carbide phase relative to the bulk magnetite phase was still not significant enough to cause an observable change in the CO conversion. The only observation that was worth noting was the fact that CO conversion had increased in agreement with the initial hypothesis. It was therefore promising to observe that a catalysts mixture that has more iron carbide phase could likely improve the activity of the Fischer-Tropsch catalysts. Beyond this iron carbide composition, a gradual decrease in catalyst activity was noticed with the rise in the cementite composition. This was in contradiction with previous results as observed by Gnanamani et al. (2013), (Dragomir B. Bukur et al., 1995a) who reported in their work that CO conversions generally increase with the increase in the amount of iron carbide phases present in the catalysts after activation. Their studies however used iron carbides that were generated during the activation stage using carbon monoxide as the activation gas. They also varied the reaction temperature which was kept constant in this work. An increase in the reaction temperature strongly improves the FTS activity when there is smaller percentage of carbides in the samples. The only disadvantage with this will be the increase in the methane selectivity as more methane is formed at higher temperatures. This will consequently result in reduced chain growth probability factors and hence minimising C_{5+} selectivities.

There was a decrease of about 9.5% in the CO conversion after 80% magnetite content. Many researchers have worked on projects to study the effect of in-situ synthesised iron carbides and there has not been a convincing proposal on the exact FT activity response to variations in catalysts composition when using unsupported and unpromoted iron based Fischer-Tropsch catalysts. A minimum catalyst activity was observed at 50% magnetite content and this low activity was not expected since activity was believed to be directly proportional to the amount of carbides present in the catalysts mixture. The low activity was however thought to be as a result of an increased deactivation rate from the amorphous and graphitic carbon deposited on active catalyst sites. This carbon was believed to have emanated from the remains of the decomposed biopolymer matrices from the gelatine, ammonium alginate and chitosan. FT activity however increased when the amount of iron carbide catalysts was increased to 70% since a CO conversion of 48 % was recorded under these conditions. This increase was attributed to the increase in the amount of iron carbides since all the other conditions were kept constant at their original values. This was further supported by the fact that the other two (2) reactions with 90% and 100% iron carbides lead to a further improvement

in per pass CO conversion. A maximum conversion of 81.8% CO conversion was recorded using pure iron carbide nanocatalysts under the same conditions.

Studies that were done by (Bo et al., 2012) on the presence of Hägg carbides which form in iron based catalysts observed that the 2.6 and 5.3 wt.% iron carbide initially depicted high catalytic activity which then dropped considerably as the reaction proceeded for a longer time. The level of activity that it then displayed was almost the same as that of pure magnetite and they made a conclusion suggesting that carbon deposition was increased due to the presence of carbides and hence accelerating catalysts deactivation. Subramanian et al. (2016) was of the view that the reduced catalysts which contained iron carbides accelerated the FTS activity because they had a higher concentration of active sites than that of unsupported magnetite catalysts.

They also noticed that with some reaction runs with a rise in iron carbides composition, deactivation of active sites by amorphous and graphitic carbon may start, hence decreasing the catalytic ability of catalysts. This means that the addition of iron carbides requires proper control and monitoring since the addition of carbon containing species might favour the surface deposition of carbon. This will give rise to a carbon layer forming at the surface of active sites and the result will be the subsequent decrease in FTS (Moodley et al., 2009, Wei Chen et al., 2008). The effect of having iron carbides on the rate and FTS activity that was noticed in this work is comparable to a larger extent to observation that were made by (B.H. Davis and Occelli, 2016) in their recent studies. Moskovits and Miller proposed the idea of a dissociative and competitive CO chemisorption versus H_2 adsorption on the surface of catalysts, which they said resulted in maximum conversions as a function of carbides content.

With lower carbides content, it is assumed that H_2 chemisorption is stronger than CO adsorption and hence the amount of active methyl species that is accessible for the formation of hydrocarbons is lower, and therefore a decreased FTS activity due to reduced uptake of carbon sources on surface species. This situation is reversed when the carbides content increases. The presence of iron carbides will increase CO dissociative adsorption, reduce H_2 chemisorption and hence the FTS activity is increased. For this work, at low levels of carbides, for example (10-20) % carbides, CO chemisorption was moderately improved, and simultaneously H_2 chemisorption was not noticeably decreased, and therefore an averagely lower activity was observed. The abnormally low activity that happened at the 50% carbides level can also be explained using this principle.

4.5.3 Results on gaseous phase analyses:

During the Fischer-Tropsch reaction, different hydrocarbons are produced which include mostly straight chain paraffins, olefins and oxygenates. Depending on the type of catalysts and operating regime selected

for the process, different product cuts with varying selectivities are produced. This wide spectrum of products give rise to what is termed the Fischer – Tropsch product hydrocarbons distribution.

4.5.4 Hydrocarbon distribution

This variation of product selectivity in the Fischer-Tropsch synthesis is dependent on the chain growth which is predicted by the chain growth probability factor alpha (α). Hydrocarbons distribution in Fischer-Tropsch products was articulated by Anderson, Schulz and Flory in their well-known work which gave rise to the popular Anderson, Schulz Flory product distribution shown earlier in **Figure 2.2** of **chapter 2** in this work. When low values of α are prevalent, shorter chain hydrocarbons such as methane are produced and at high values of α, more long chain hydrocarbons are produced. Waxes are also produced under condition of high values of α reported by Dry, 1996. Since the objective of this work was to come up with a catalyst composition that produces long chain hydrocarbons with five (5) or more carbon atoms, it was important to evaluate the C_{5+} selectivity for each of the eight catalysts mixtures. This fraction of products is important because it constitutes all the liquid fuels and the more valuable hydrocarbons that are essential for the petrochemical industry.

Table 4. 7: The Fischer-Tropsch nanocatalysts mixtures activity and hydrocarbons selectivities[a].

	Magnetite Content (wt. %)							
	100	**90**	**80**	**60**	**50**	**30**	**10**	**0**
Temperature (K)	493	493	493	493	493	493	493	493
CO Conversion (%)	37.9	42.6	44.5	35.0	30.9	48.6	81.0	82.8
H_2 Conversion (%)	17.7	32.2	17.7	72.2	88.6	53.9	88.2	87.3
Hydrocarbon selectivities (%)								
CH_4	20.6	19.5	20.1	10.3	6.9	16.1	13.9	11.9
C_2	0.6	0.2	0.7	8.4	5.7	13.2	11.4	9.8
C_3	5.4	4.8	3.5	8.4	3.1	7.2	6.2	5.3
C_4	0.51	1.9	2.7	3.4	2.3	5.4	4.6	4.0
C_{5+}	72.9	73.6	73.0	69.5	82.0	58.1	63.9	68.9

[a]Reaction conditions: 220 ^{0}C; 20 bar; H2/CO = 2.0; syngas flow rate = 45 sccm.

Table 4.7 shows the effect of iron carbide addition to magnetite on the distribution of hydrocarbons under the same reaction conditions of temperature and pressure. It was observed that the average molecular weight of FTS products increases with the increase in the amount of cementite added to that catalyst mixture. This suggests that iron carbides specifically cementite (Fe_3C) in this work is an effective FT catalyst that enhances the performance of magnetite nanocatalysts in the Fischer-Tropsch reaction. It is also eminent from the results obtained that the addition of iron carbide to the catalysts system restrained the formation

of methane and other lighter hydrocarbons. The shift in selectivity to higher molecular weight hydrocarbons observed in the present study was attributed to the presence of more carbide catalyst sites provided by these nanocatalysts as their inclusion in the catalysts mixture resulted in a higher reaction rate.

The effect of iron carbides on the hydrocarbon distribution is not deviating with a greater margin from observations made in numerous earlier studies which used iron-based FTS catalysts and in-situ produced iron carbides (Dragomir B. Bukur et al., 1999, Amelse et al., 1978, Cano et al., 2017). The increase in hydrocarbon chain lengths in the products is thought to be as a result of the fact that the H_2/CO ratio on catalyst surface can be improved by the existence of carbide species on the surface of the catalysts particles. There are also additional carbides that are believed to have been formed because of the catalyst activation stage that made use of CO gas and hence increasing the amount of carbides present in the mixture. In this regard, it means the presence of iron carbides increases the probability of the continuous growth of the hydrocarbon chain. This had a net effect of producing higher molecular weight hydrocarbons as observed by the higher C_{5+} selectivity on a carbon basis. Several earlier studies of Kölbel, (1972) and Dragomir B. Bukur et al. (1999) also reported an improvement in the formation of long chain products using iron based catalysts which had iron carbide catalysts included in the catalyst composition.

4.5.5 Product selectivity:

This study not only focused on the effect of iron carbide addition to magnetite nanocatalysts on C_{5+} selectivity but it also focused on the formation of methane, C_2-C_4 gaseous hydrocarbons and oxygenates. Oxygenated hydrocarbons were part of the product mix in the liquid products which were in significant amounts. Carbide content effects on catalyst selectivity to alkenes, carboxylic acids and aldehydes was also observed as illustrated in the sample chromatogram from GC-MS analysis in **figure 4.27** below. With different composition of iron carbide in the catalysts mixture, it was noticed that varying amounts of these products were detected. Of particular interests was the increasing quantities of alcohols in the liquid product which were in significant amounts. These products were not quantified in this analysis since their analysis would have required standards. Olefins also formed a significant part in the product mix and these included both linear and branched chains. The GC-MS spectrum below shows a sample chromatogram from the aqueous phase fraction of the liquid products.

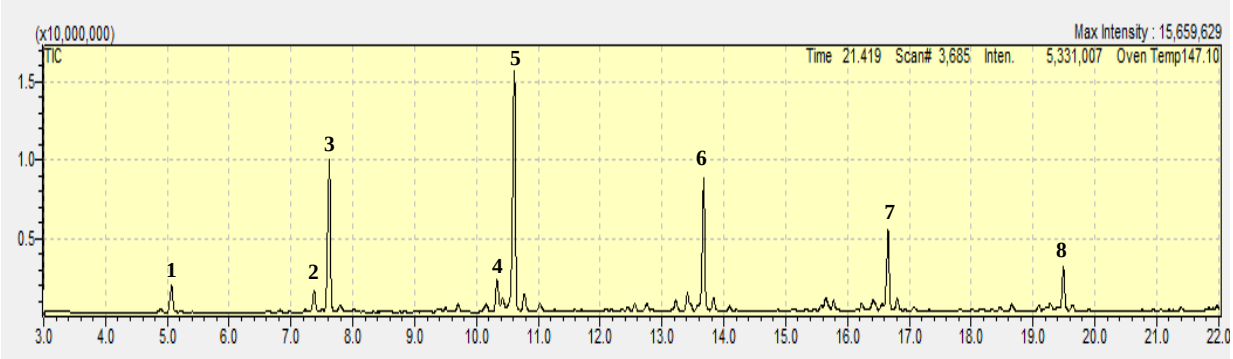

Compound number	Retention time/min	Compound Name
1	5.085	Octane
2	7.405	1-Nonene
3	7.63	2,4-dimethyl- Hexane,
4	10.44	cis-4-Decene
5	10.61	4,8-dimethyl- Tridecane,
6	13.67	2-Undecene, (Z)-
7	16.67	2-methyl- Decane.
8	19.54	3-Tetradecene, (Z)-

Figure 4. 27: GC-MS spectrum and peak table of hydrocarbons analysis of the aqueous phase fraction of the liquid products produced during slurry phase Fischer-Tropsch synthesis.

From the GC-MS analyses it was also observed that the olefins content in the liquids products cut increased remarkably with a rise in the percentage of iron carbide loaded in the catalyst mixture. However, the olefin to paraffin ratios were not quantified as the objective of the study was limited to identification and not quantification of the individual hydrocarbon products in the liquid products. Carboxylic acids and carbonyl compounds were also identified in the product mixture, but their quantities were lower than that of olefins. Thus, an increase in the iron carbide content under low temperature Fischer-Tropsch reaction conditions improves the overall C_{5+} selectivity and liquids production and maintains CO conversion. It was therefore observed that the effect of iron carbides in this current study on the catalysts selectivity to olefins are in tandem with other reported observations (Yi Liu et al., 2015, Xing-Wu Liu et al., 2017, Qiangu Yan et al., 2013). These researchers reported that the influence of cementite (Fe_3C) on olefins selectivity is explained in terms of its effect on the strength of carbon monoxide and hydrogen chemisorption (Yi Liu et al., 2015). In their work, iron carbide was suggested to increase the strength of CO chemisorption thus suppressing the addition H_2 atoms at the surface and hence controlling the amount of adsorbed H_2. This will in turn promote the production of more olefins than paraffins as shown in figure 4.28 below (B.H. Davis and Occelli, 2016).

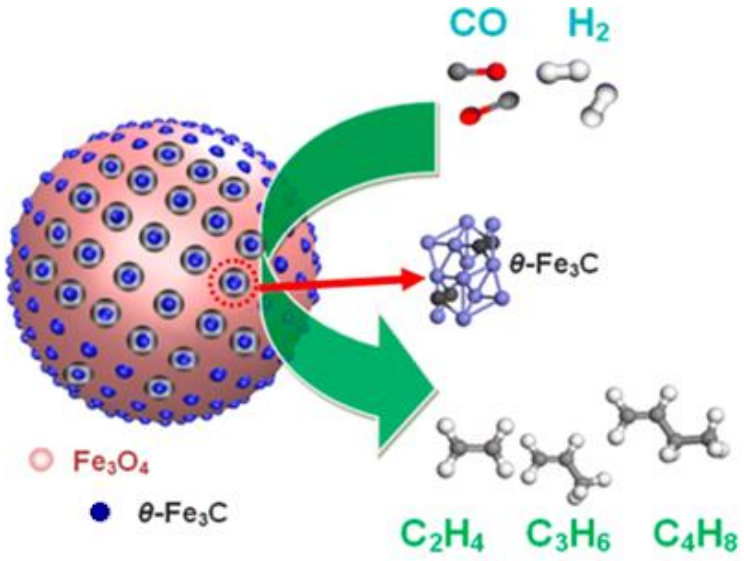

Figure 4. 28: Iron carbide sites responsible for the production of olefins, adapted from Xing-Wu Liu et al., 2017.

In this illustration, the blue catalyst sites containing θ- Fe_3C are assumed to be the ones that are responsible for the higher selectivity to olefins which were mainly detected in the liquid products. These sites were believed to have increased the catalysts selectivity to long chain hydrocarbons. It was also noted that the C_2-C_4 fraction improved as well signifying a growth in chain length. To better understand the Fischer-Tropsch product selectivity, the methane selectivity for all the eight (8) experimental runs was evaluated.

4.5.6 Methane Selectivity:

The methane production in any Fischer -Tropsch process is undesirable since its commercial value is lower compared to longer chain hydrocarbons. On the other hand, thermodynamically methane is actually the most favoured stable Fischer-Tropsch synthesis product. It is therefore not part of the desired products. This is the reason why the production of methane should be kept as low as possible for any economic benefit to be realised in the process. Methane is formed when surface hydrogen combines associatively with a methyl species and on the surface of a catalyst. This step is thought to be the one that can aid in the formation of longer chains hydrocarbons since these methyl species are believed to alternatively be responsible for initiating the grown of hydrocarbons chains as shown below.

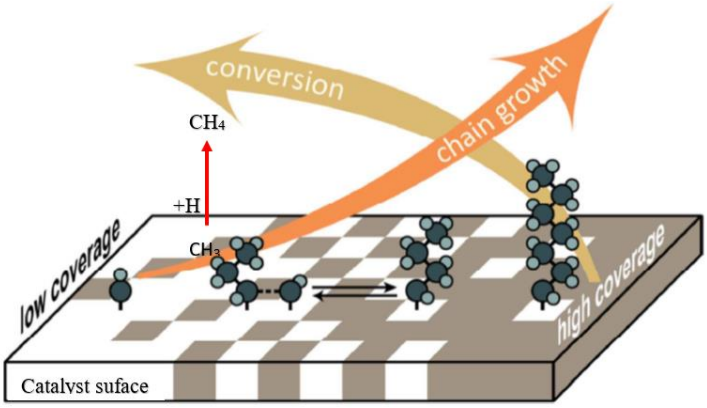

Figure 4. 29: Chain growth and early chain termination on catalyst surface sites to producing methane.

The methane selectivity is usually dependent on whether the carbon containing monomer (intermediate) is likely to desorb from the catalysts surface or not. When the surface methyl species prematurely desorbs by hydrogen addition, the Fischer-Tropsch reaction favours the formation of methane and consequently a higher methane selectivity is likely observed. In this work, the quantity of methane that was produced was detected and analysed using a TCD connected to a Shimadzu 2010 *Plus* Gas Chromatograph and a sample trace of the chromatogram is shown in **figure B4** in the Appendix. In this work, the methane selectivities that were obtained in C-% started at an unusually high value of 20% for the 100% magnetite catalyst mixture. The value was observed to reach a minimum value of 6.9% for the catalysts mixture that contained 50% magnetite and 50% iron carbide nanocatalysts. These values are considered too high since methane selectivities of around 4 - 6% are generally expected for the low temperature slurry phase Fischer Tropsch reaction. Figure 4.30 below shows the variation of methane selectivity as observed from the eight (8) catalyst mixtures.

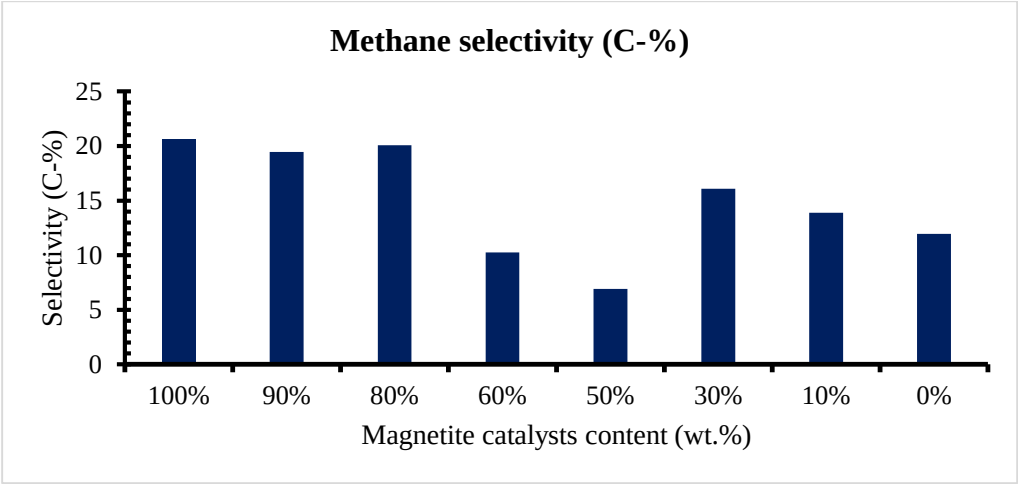

Figure 4. 30: The effect of iron carbide addition to magnetite on methane selectivity (TOS = 48 hours).

It can be observed that the methane selectivity is generally lower for the catalysts mixtures containing iron carbide catalysts as shown in **figure 4.30** above. As observed earlier, these catalysts also showed a higher activity as shown by their CO conversions. In all the reactions, it was however noted that the selectivity to CO_2 was very low since no detectable amounts of CO_2 were identified in TCD analyses. The observed decrease in the methane selectivity can be explained in terms of the reduction of the CO partial pressure after exposure to syngas. This reduction in CO partial pressure is assumed to reduce the inhibition of the Fischer-Tropsch reaction through adsorbed CO. Since iron carbide containing catalysts had a higher conversion and activity, the amount of carbon monoxide on the catalysts surface was reduced. As reported by van Santen et al. (2011), a high CO coverage of the catalytically active surfaces will yield methane.

4.5.7 Results on liquid phase analyses:

To have a quantitative measure of the amount of long chain hydrocarbons being produced during the Fischer – Tropsch reaction, it is very important to evaluate the C_{5+} selectivity of the process. This parameter gives an indication of the extent of chain growth and the likelihood of producing heavier hydrocarbons. The C_{5+} selectivity was indirectly determined from the selectivities of the short chain hydrocarbons but the information it depicts tells us more about what constituted the liquid products that were produced. As explained from the previous chapter,

4.5.7.1 C_{5+} selectivity:

The C_{5+} selectivity is greatly influenced by the chain growth probability factor (α) which provides information about adsorptive chain growth of organic products. In this regard, a high chain growth probability points to the production of long chain hydrocarbon. The C_{5+} selectivity is an important parameter that provides an indication of the economic viability of the process since it gives a measure of the amount of valuable liquid hydrocarbon products being produced. In this work, this quantity was evaluated using the selectivities of gaseous hydrocarbons starting from methane which is a C_1 alkane and individual selectivities of C_2 to C_4 hydrocarbons were also evaluated and used for the ultimate calculation of the C_{5+} selectivity. From the gaseous phase GC analysis which employed both the thermal and Flame ionisation detectors (TCD and FID), these light hydrocarbons were quantified and their selectivities were then summed up to yield the total C_1-C_4 hydrocarbons selectivities. The C_{5+} selectivity of the process expressed as a percentage was calculated as the difference from 100 % of the sum C_2-C_4 selectivities as shown below:

$$S_{C5+}(\%) = 100 - (S_{C1} + S_{C2} + S_{C3} + S_{C4}) \qquad \text{equation 4.1}$$

The C_{5+} selectivity was expressed as a percentage and it represents that fraction of products that were mainly in the liquid Fischer – Tropsch products. Most of the long chain hydrocarbons five (5) or more carbon atoms are liquids and waxes at room temperature and therefore were collected either in the hot catch pot, cold catch pot or they remained in the reactor. **Figure 4.31** below shows a sample of the liquid products that were collected from the catch pot after 48 hours of Fischer Tropsch reaction.

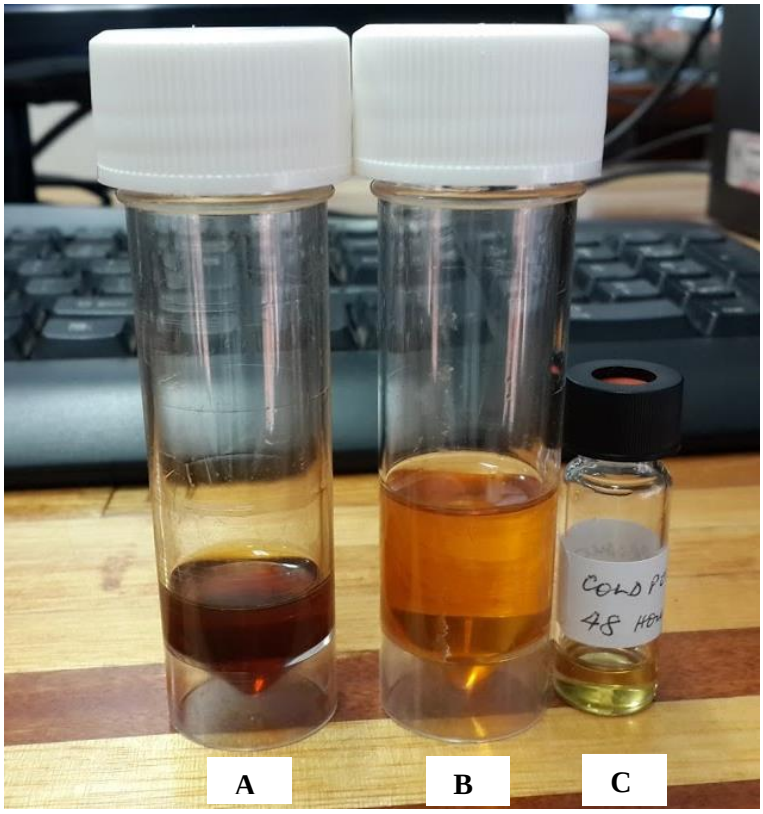

Figure 4. 31: Samples of the Fischer-Tropsch liquid products obtained after 48 hours of activity. **A-** First samples from hot pot, **B -** sample from hot pot after several runs, **C-** sample from cold pot.

The first samples of liquid products which were tapped out from the hot catch pot had some entrained nanocatalysts and this explains why the sample was a bit dark in colour as seen in sample A. These samples and one from the reactor after separation from catalysts were then analysed using GC-MS for the identification of all the hydrocarbons that were produced from the reaction.

Figure 4.32 shows a chart depicting the calculated C_{5+} selectivities for mixed magnetite and iron carbide nanocatalysts. The chart shows that, initially there was a slight increase in C_{5+} selectivity from an initial value of 72.8% to 73.6%. This was achieved using 100% magnetite and 90 % magnetite nanocatalysts mixtures respectively. The value then slightly decreased when the amount of iron carbide was increased but peaked to 82% C_{5+} selectivity with a catalysts mixture which had 50% magnetite (a 1:1 ratio of the two

(2) catalysts). The minimum C_{5+} selectivity recorded in this work was 58% which was realised when using a catalyst mixture containing 30% magnetite as shown in figure 4.32 below. The chart also shows clearly how the C_{5+} selectivity was varying with catalyst mixture composition along with the methane selectivity as more iron carbide was being added to the magnetite nanocatalysts. To bring into perspective how the C_{5+} selectivity was varying, the CH_4 selectivity is included in the chart.

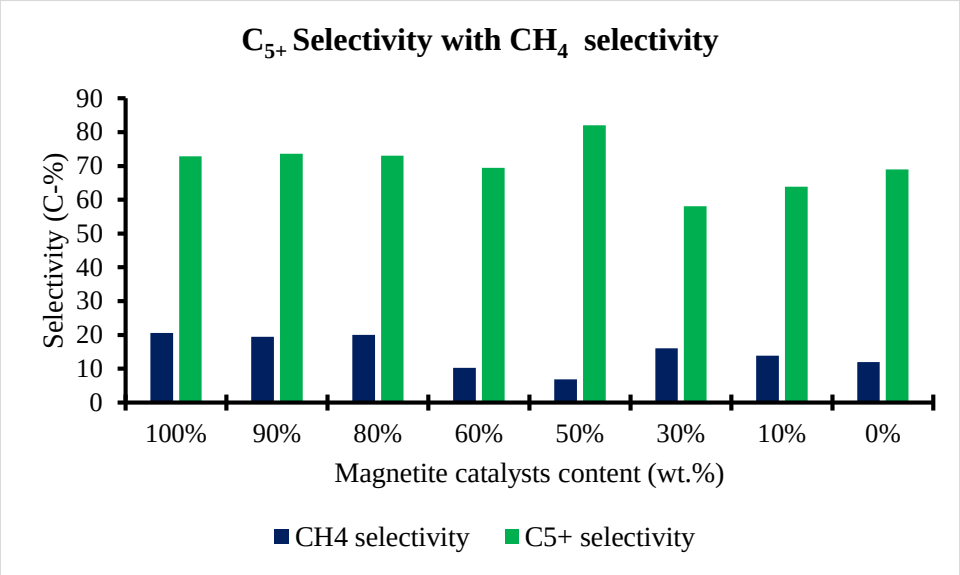

Figure 4. 32: Effects of iron carbide content on the C_4 and C_{5+}, selectivities.

It can be noted that the highest C_{5+} selectivity of 82% that was observed with a catalyst mixture containing 50% magnetite was also accompanied by minute quantities of undesirable products, such as methane at a selectivity of 6.9% and other short-chain gaseous hydrocarbons (C_2-C_4). This selectivity for long chain hydrocarbons was encouraging considering that it can be optimised to produce better yields if the behaviour of the catalyst surface is understood and modified. The only worrying fact with this catalyst mixture was the unexpectedly low CO conversion since it was the lowest at this composition. There was generally a compelling C_{5+} selectivity for all the eight (8) catalysts mixtures owing to their high ability to competitively adsorb CO and hence promoting chain growth. This was particularly motivating since it was the first time iron carbide catalysts prepared through this way were used in slurry phase FTS. The gradual decrease in C_{5+} selectivity as the amount of iron carbide increased from (50 -100) % could be due to slight increases in the amount of surface hydrogen that promotes desorption of products at the surface resulting in poor chain α – values. Catalyst selectivity for the pure magnetite was also good and even higher than that observed with some catalyst mixtures. The methane selectivity for this reaction was a bit worrisome. A methane selectivity of 20.6% is not desirable as it is not economic to carry out the Fischer-Tropsch process under such conditions. The selectivity should lean more towards longer chains hydrocarbons from which liquid

transportation fuels and more valuable products are produced. This was more favourable with catalysts that contained iron carbide in them. There was also an advantage of producing short chain olefins which are important raw material in the plastics and petrochemicals industry. A maximum of 25.8% of short chain C_2-C_4 hydrocarbons was observed with a catalysts mixture that contained 30% magnetite. A process that produces a sizeable amount of C_2-C_4 hydrocarbons and mostly C_{5+} products is more favourable since it reaps economic benefits from the sale or conversion of these short chain olefins. The summarised results of the relative quantities of CH_4, C_2-C_4 and hydrocarbons that were produced is given in figure 4.33 below.

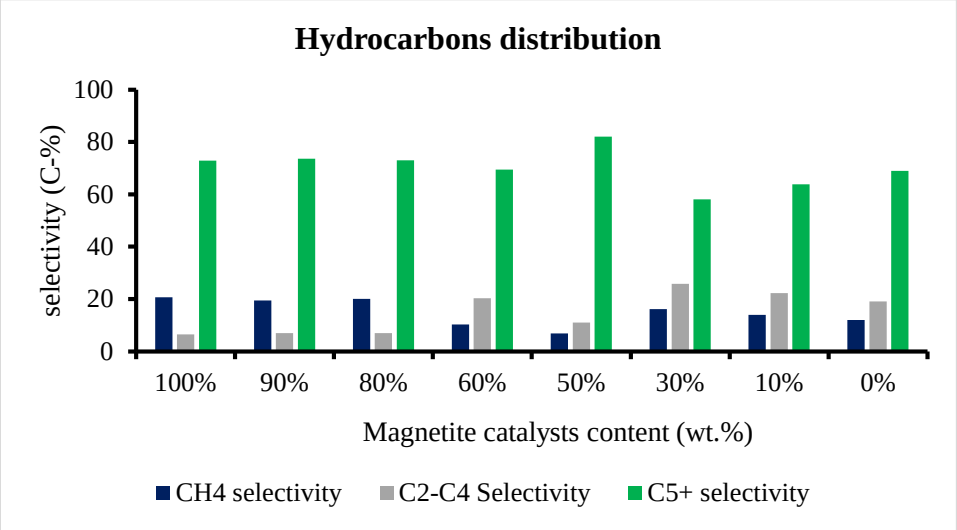

Figure 4. 33: Effects of iron carbide content in catalysts mixture on CH_4, C_2-C_4 and C_{5+} selectivities.

Figure. 4.33 shows that there is a marked difference in the trend shown for C_2-C_4 and C_{5+} hydrocarbons selectivities for low iron carbide to high iron carbide content. Observation from earlier studies (Dragomir B. Bukur et al., 1999, Dragomir B. Bukur et al., 1995a, Amelse et al., 1978) using in-situ prepared iron carbide catalysts mixed with various iron oxides catalysts resemble the observations found in this work. In the product mixture analysed using GC-MS it was noticed that long chain hydrocarbons up to C_{45} paraffins were produced. Most of the produced oxygenates were mainly composed of alcohols, esters and carbonyl compounds represented by the smaller peaks on the chromatogram shown in **figure 4.35**. The product spectrum was therefore mainly dominated by straight chain alkanes which are also shown on the chromatogram. It was observed however that in this C_{5+} product cut, the quantities of oxygenated hydrocarbons were more pronounced in the analysis of the aqueous fraction of the liquids hydrocarbons since they were separated into two (2) fraction after settling.

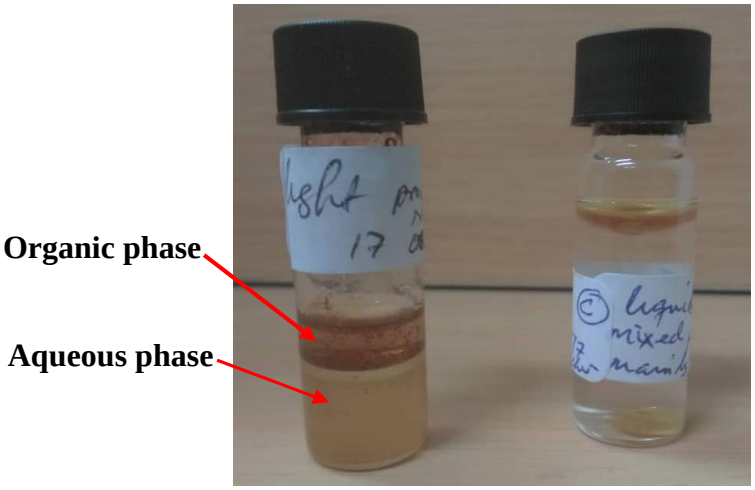

Figure 4. 34: Sample liquid products of the samples from the aqueous phase containing oxygenated compounds and olefins.

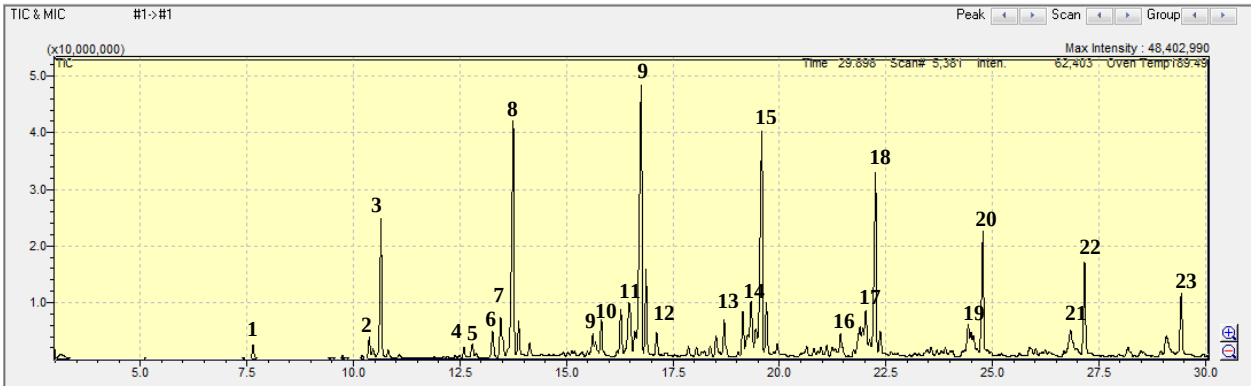

Figure 4. 35: Sample chromatogram from GC-MS analysis of the sample from the aqueous phase showing the presence of oxygenated compounds and olefins.

Table 4. 8: Some of the Fischer – Tropsch products identified from the aqueous phase analysis

Compound number	Retention time/min	Compound Name
1	7.63	Hexane, 2,4-dimethyl-
2	10.36	2-Decene, (Z)-
3	10.61	Tridecane, 4,8-dimethyl-
4	12.16	Decane, 3-methyl-
5	12.48	1-Octanol
6	13.26	2-Butyl-1-decene
7	13.68	1-Undecene
8	13.87	4-Undecene, (Z)-
9	15.70	1-Nonanol
10	15.74	Oxacyclododecan-2-one

The aqueous phase analysis of the liquid products as depicted in **figure 4.35** showed a greater proportion of oxygenated compounds than the sample that was obtained from the reactor residue. Products in the reactor residue are usually long chain paraffins and olefins. These usually have high boiling points and normally do not mix well with products such as alcohols, aldehydes, ketones and carboxylic acids. They form distinct separate layers. Figure 4.36 shows a sample chromatogram that was produced from the GC-MS analysis of heavy hydrocarbon products from the reactor residue.

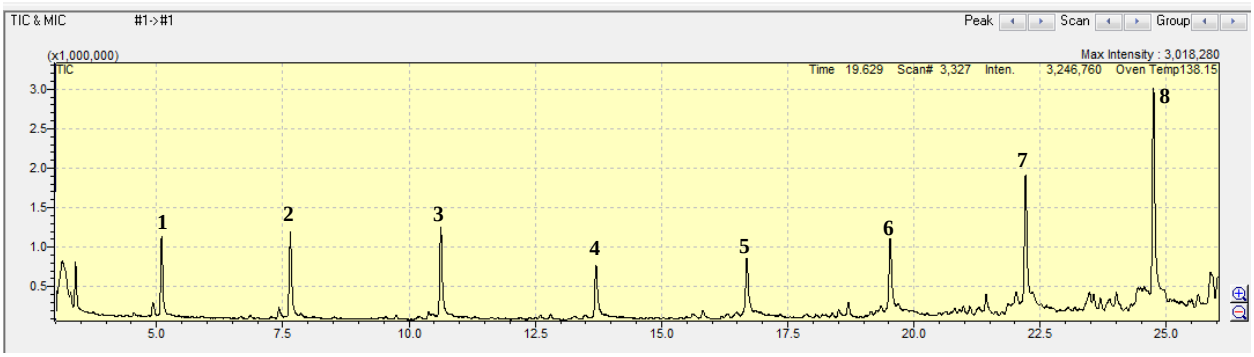

Figure 4. 36: Sample GC-MS chromatogram from analysis of the residual reactor product after catalysts separation.

Table 4. 9: Some of the Fischer – Tropsch products identified from the analysis of heavy products.

Compound number	Retention time/min	Compound Name
1	5.09	Octane
2	7.63	Hexane, 2,4-dimethyl-
3	10.61	Tridecane, 4,8-dimethyl-
4	13.69	Tridecane, 4,8-dimethyl-
5	16.33	Dodecane
6	19.51	Decane, 2-methyl-
7	22.21	Octadecane
8	24.73	Pentadecane

The production of oxygenated compounds agrees with the propositions given by Bileon and Sachtler in which they said the formation of oxygenates is favoured by oxidic surface sites on catalysts. In this work this assertion seems to be true because the spent catalysts that were analysed after the reaction showed that a larger proportion of the catalysts phases to be magnetite, haematite or even iron. The presence of these oxides is believed to be a contributing factor to increased production of oxygenates. The XRD analyses of

the spent catalysts in this study showed that the selectivity of oxygenates varies in proportion to the amount of iron oxide (magnetite) present and inversely proportional to that of iron carbides in the mixture. This was largely true when analysing samples after TOS greater than 4 days. To a greater extent, results of spent catalysts characterization agrees well with the explanations given by Bileon and Sachtler, 1986 and Yang et al., 2017.

The difference between the analyses of liquid samples that were extracted from the reactor residue after catalysts separation and cold pot products can be observed by comparing chromatograms shown in **figure 4.36** and that of **figure 4.35**. The majority of products formed were mainly long straight chain paraffins since peak intensities/height were increasing with increasing retention times.

4.6 Spent Catalysts Characterisation:

After every reaction run, catalysts were isolated from the mixture which contained heavy liquid products and the initial solvent (Durasyn® 164 polyalphaolefin). This characterisation was important since it allows conclusions to be made about the active phase changes that were occurring during Fischer–Tropsch reaction for the entire period in which catalysts were exposed to reactants. The other important aspect was the particle size of the crystallites after the reaction which needed to be evaluated to get information about the extent of catalysts deactivation.

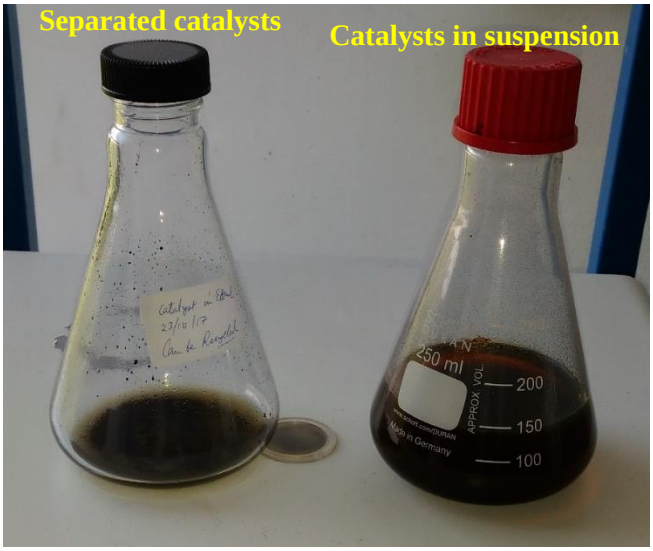

Figure 4. 37: Residual Fischer – Tropsch products from the reactor during spent catalysts separation using centrifugation.

Separation was achieved through the use of centrifugation at 5000 rpm for seven (7) minutes and then magnetic separation was used to separate the catalysts from the remaining solvent. The catalysts were subsequently washed alternately using dichloromethane and ethanol then dried for analysis. Since all the

catalysts were mixed to form mixtures before every Fischer-Tropsch reaction, the post reaction analysis experiments were meant to determine the resulting catalysts phases after the reaction. The effects of adding different proportions of iron carbides to magnetite nanocatalysts were observed since the selectivity and hydrocarbon distribution were determined. The 100% pure magnetite sample and all the other catalysts mixture after the reaction were all submitted for characterisation. Scanning and Transmission electron microscopy techniques were used to determine the morphology and particle sizes respectively. Catalysts phases were ascertained using Powder X-ray diffraction (PXRD).

4.6.1 Microscopy results of spent catalysts:

Sample preparation for the spent nanocatalysts was similar the one for fresh samples but these were not as dry since some of the solvent and waxy products from the reaction remained entrapped within the catalysts. This compromised the proper particle characterisation since particles were somehow agglomerated as can be shown below:

4.6.1.1 TEM, SEM and EDX results of spent catalysts:

To asses that change in particle morphology the following results were obtained with regards to topography of the nanoparticles after the reaction. The EDX spectrum also indicates the approximate composition of these catalysts. From the SEM images shown, the catalysts particles were observed to be highly agglomerated and some particle sintering and fouling were suspected to be the reason for this observation. It was however known that there was still a certain amount of the initial starting solvent and hydrocarbon products that were part of the sample as they were not 100% dry.

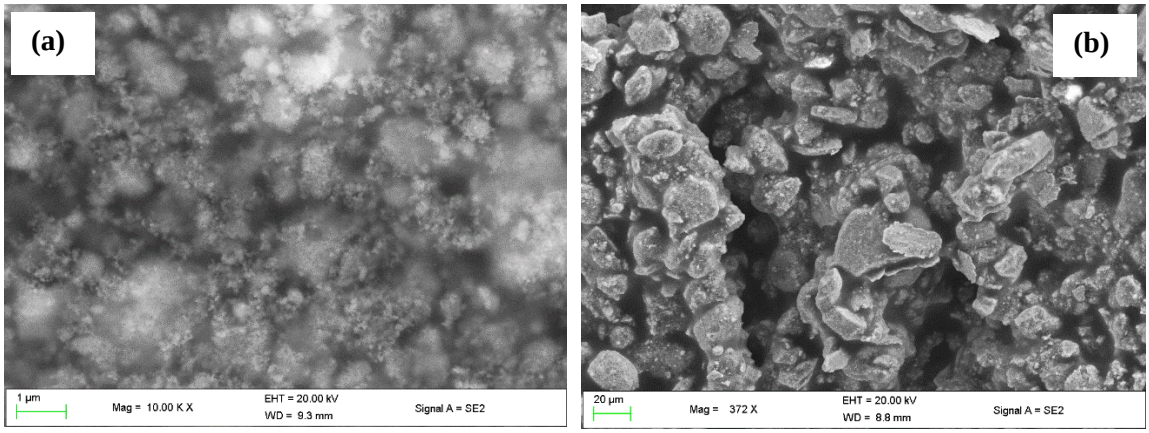

Figure 4. 38: SEM micrographs of spent catalysts samples after a TOS of 120 hours.

It was also clear that the particles had slightly increased in particle size mostly due to fouling and particle sintering as can be confirmed from the TEM images shown in figure 4.39. Image (d) at a lower

magnification clearly shows the clustering of the particles. The EDX spectrum provided the approximate composition of these spent catalysts.

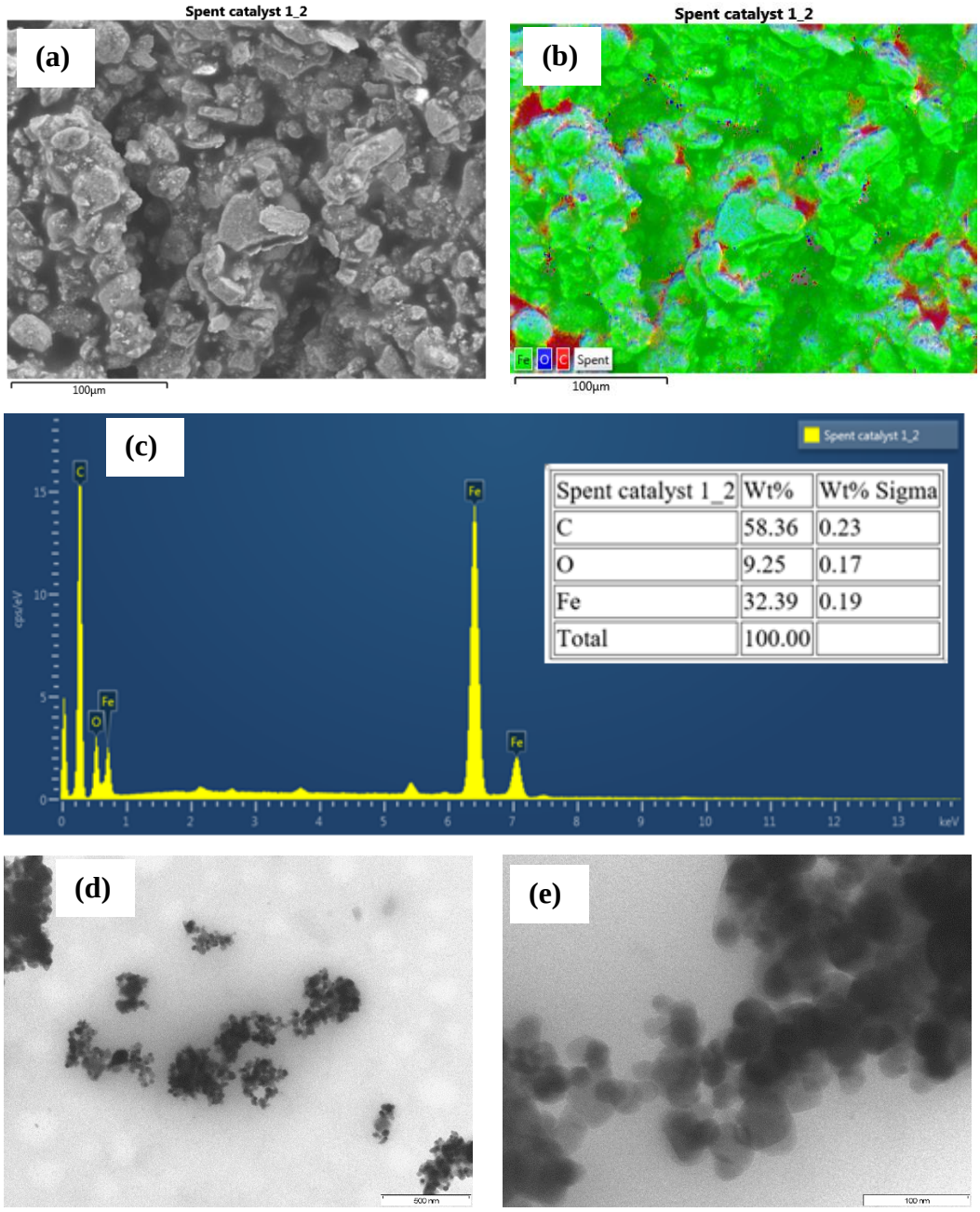

Figure 4. 39: SEM, TEM and EDX results for spent nanocatalysts, showing morphological and particle size changes.

The bright areas shown in image figure 4.38 **(a)** are as a result of the presents of the hydrocarbons on the surface of the catalysts. The particles were clustered, and it was difficult to take high magnification images

due to the reflection that was being emitted by the hydrocarbon compounds. The particle size distribution and more images obtained from these spent nanoparticles are given in **Appendix C.**

From the EDX spectra shown in figure 4.39 **(c)**, it can be observed that an increase in the amount of carbon content (58.36%) was detected in the catalysts. It was however not easy to differentiate whether the amounts given were as a result of amorphous, graphitic or carbon from the Fischer – Tropsch products that were still stuck to the surfaces of the catalysts. This information could only be clearly understood from the PXRD data which provided the catalysts phases that were detected in the analyses. It was however clear that there was a lot of oxidation that was happening in the catalysts since most of the carbide phase was changed into mostly oxides. Powder X-ray diffraction results showed that the dominant phase was magnetite.

4.6.2 XRD results for spent catalysts:

Powder X-ray diffraction analyses for the spent catalysts was carried out soon after the separation of the nanocatalysts from the solvent and drying of the samples in an air free environment to avoid further oxidation of nanocatalysts on exposure to atmospheric conditions. Heating of the sample was limited to 60 ^{0}C to limit phase changes during drying. **Figure 4.40** below shows the XRD spectrum that was obtained from the sample that contained 100% magnetite fresh catalysts. The sample was mainly composed of the magnetite phase as confirmed by Rietveld refinement of the XRD spectrum. Major peaks for the crystal planes at angles equal to 21.5^{o}, 35^{o}, 41.5^{o}, 50^{o} and 74^{o} were assigned to magnetite. As observed, 88.7% of the sample was magnetite and this means that magnetite was fairly stable in the 120 hours of exposure to Fischer – Tropsch reaction conditions.

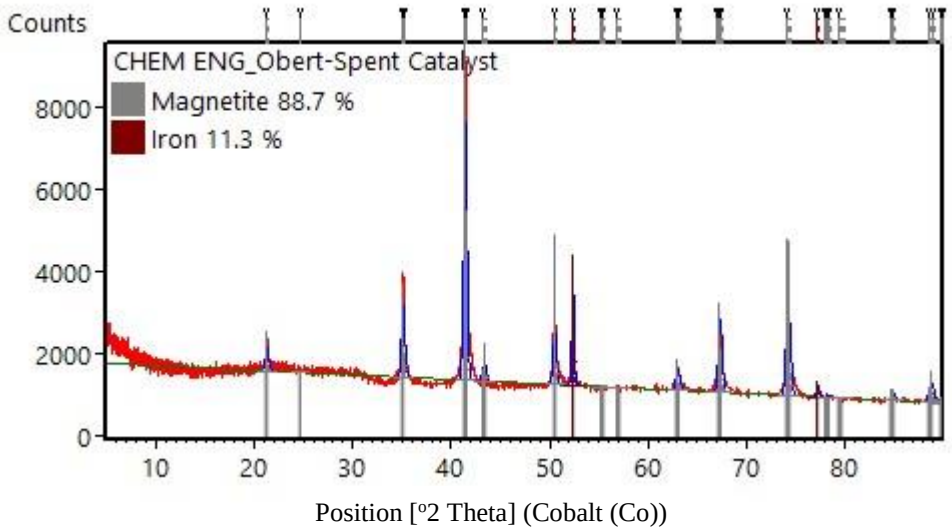

Figure 4. 40: PXRD spectrum of spent magnetite nanoparticles after 120 hours TOS.

The Fischer – Tropsch reaction is a complicated set of reactions and explaining why the other fraction of the catalyst was reduced to iron after the reaction can be sometimes challenging. The reduction of the catalysts can be due to the continued exposure to reducing agents. Both CO and H_2 are strong reducing agents and when they interact with the catalysts, a reduction of the metal oxide usually accompanies this process. The level of initial reduction that was accomplished during catalysts activation was thought to be high to the extent that when the reactions progressed, some of the catalysts might have remained in the reduced state.

The PXRD characterisation of some of the spent catalyst mixtures that contained iron carbide showed an unnamed spinel that was detected as a dominant phase in the spent catalysts. This spinel which has a formula of $Fe_{2.91}O_4Si_{0.09}$ was believed to be also active in the Fischer – Tropsch reaction. It has been reported that spinels are more stable under FTS conditions. Khoang et al., 1984 studied the presents of these spinels in cobalt based F-T catalysts and they reported that their presence resulted in an increased yield of hydrocarbons in the slurry phase FTS. Figure 4. 41 below shows the Rietveld refined XRD specturm produced from the analysis of spent catalysts.

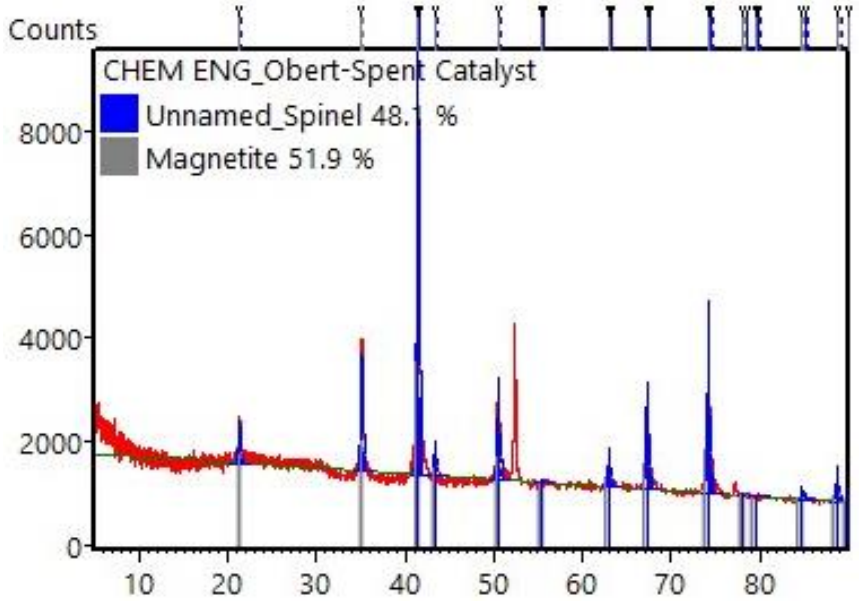

Figure 4. 41: XRD specturm produced from the analysis of spent catalysts that initially contained 60% magnetite and 40% iron carbide.

Table 4. 10: Major spent catalysts phases that were detected from the PXRD analysis.

Date: 2018/05/23 Time: 11:19:07 File: CHEM ENG_Obert-Spent Catalyst User: 216076162

No.	Visi...	Ref. Code	Compound Name	Chemical Formula	Score	SemiQuant [%]	Display Color
1	☑	98-015-8584	Unnamed_Spinel	Fe2.91 O4 Si0.09	75	79	Blue
2	☑	98-008-2444	Magnetite	Fe2.937 O4	25	21	Gray

Analysis of more samples of spent catalysts that initially contained a mixture of of both magnetite and iron carbides showed that the resulting catalysts had five (5) dominant phases. Magnetite, the unnamed spinel, Cohenite, maghemite and hematite were detected in these samoples.The presence of cohenite (C_1Fe_3) confirmed that iron carbides were still present in the catalysts mixture after 120 hours of exposure to reactants. **Figure 4.42** shows the XRD spectra of some of the spent catalyst that were analysed and refined using Reitveld.

Nanosized iron carbide crystallites are believed to have a much higher active surface energy and assumptions have been made that their oxidation is more feasible than catalytic oxidation of bulk iron carbides. Mabaso, (2005) reported this phenomenon using iron carbide nanocrystallites and it was also shown theoretically by van Steen, 2005 using nanosized cobalt crystallites.

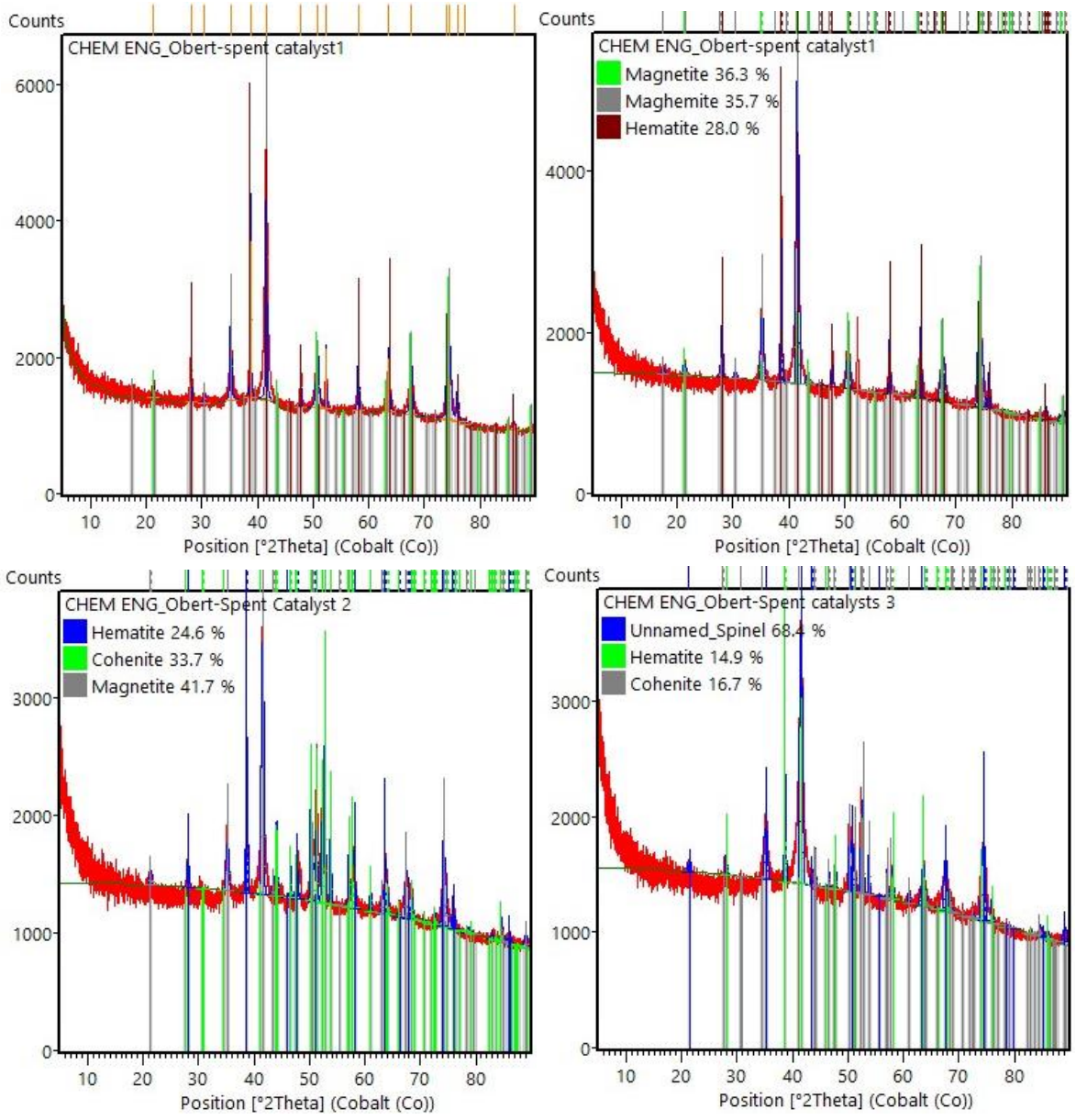

Figure 4. 42: Reitveld refined XRD spectra of spent catalysts after 120 hours TOS.

The reason for the presence of the various iron oxides in the spent catalysts can be explained using the "Oxidation Theory." This theory suggests that the lower C_{5+} selectivity and activity of the mixed magnetite and iron carbide catalysts which was observed might be because of the straightforward transformation of iron carbides to magnetite. It should however be noted that not all the carbides were converted to magnetite and other oxides, but some remained stable and hence the observed average activity and C_{5+} selectivity. The presence of a lot of reaction water especially during the first few hours of activity was a serious concern on the stability of the carbides in the catalysts mixtures since too much water is known to oxidise carbides to

various iron oxides. This phenomenon was however not the case for all the experimental runs. Van Steen, (2008) reported the possible reaction pathway that leads to the oxidation of some carbides to magnetite. In the mechanism that was postulated, catalysts sintering especially magnetite nanocatalysts were also believed to be deactivated in the process as was observed in this work. Whilst using precipitated iron catalysts, reductive carburisation coupled with crystallite breakup is also observed to be possible as illustrated in figure 4.43 below.

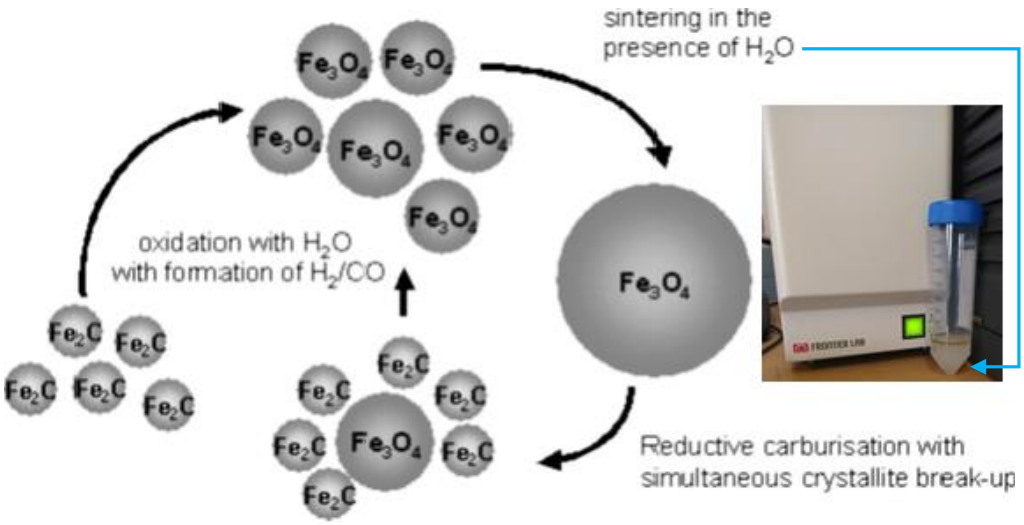

Figure 4. 43: Dynamic phase transitions in precipitated iron-based Fischer-Tropsch catalysts adapted from Van Steen and Claeys (2008).

This explanation gives some insights into the observed Fischer – Tropsch activity and C_{5+} selectivities trends that were observed in these eight experiments. However, it is not conclusive that this is the only possible phenomenon that explains the observations made. There is need for more research on the characterisation of fresh and spent catalysts using other advanced techniques like Mössbauer spectroscopy and in-situ XRD to study phase transitions.

Chapter 5

Conclusions and Recommendations:

Iron carbides have been known to be involved in Fischer – Tropsch activity but the nature of the active phase under reaction conditions remains a debatable subject. This research effort sought to interrogate this aspect and to investigate whether the catalysts' selectivity to C_{5+} hydrocarbons could be enhanced by the addition of separately prepared iron carbides to magnetite nanocatalysts. Magnetite and iron carbide nanocatalysts were synthesized, characterised and tested for performance in slurry phase Fischer – Tropsch synthesis. Iron carbide nanocatalysts addition to magnetite were found to considerably enhance the F-T catalytic activity of magnetite nanocatalysts. A 43.9% increase in catalysts activity was observed from an initial pure magnetite activity of 37.9%. The enhanced activity also resulted in improved C_{5+} selectivity and production of olefins and oxygenated hydrocarbons. A C_{5+} selectivity of 82% was obtained and it was accompanied by an increase in the production of olefins which were favoured by catalysts mixtures that contained more than 50% iron carbide nanocatalysts. Instead of the products being mainly straight chain paraffins and light olefins, it was observed that there was an increase in liquid products distribution due to the fact that more oxygenated compounds were detected in the aqueous fraction of the liquid F-T products.

The increased product quality and diversity was attributed to the increased weight fraction of iron carbides in the catalysts mixture. It was also assumed that the amount of oxygenated hydrocarbons was directly related to the catalysts' time-on-stream (TOS) as more of these compounds, particularly alcohols were detected mainly after 100 – 120 hours time-on-stream. Spent catalysts characterisation also revealed that a significant quantity of the catalysts was transformed to mainly iron oxides, chief of which being magnetite. Experimental data from one spent catalysts sample revealed a 51.9% magnetite from XRD Rietveld refinement and this was an 11.9% increase from the fresh catalysts. This occurrence can be due to oxidation of mostly carbides under reaction conditions. The oxidation is thought to be mainly due to water which was produced in significant amounts during the reaction, particularly towards the end of experimental runs. The increased production of oxygenated hydrocarbon compounds which are preferred by oxidic catalytic sites are also thought to be the reason phase changes occurred and favoured the formation of hematite and maghemite in some catalysts mixtures. Substantial experimental proof is however still required to support these claims because we can also speculate that CO dissociation was competitively reacting with metallic iron to form these oxide phases. Normally, during Fischer – Tropsch synthesis, oxygen from the carbon

monoxide should react to form water, oxygenated compounds or carbon dioxide but we can however not rule out this possible route.

The increase in particle sizes that was observed was attributed to catalysts sintering and carbon deposition. Experimental measurements from TEM, SEM and EDX provided information about the increased particle sizes and carbon content of up to 58.4% in the spent catalysts. It was however not clear whether this carbon was amorphous, graphitic or chemically bonded carbon within the iron carbide structures. This would require some further research using techniques such as TGA to assess the loss on heating, Mossbauer Spectroscopy to determine the stoichiometry or Electron Energy Loss Spectroscopy to measure the carbon shell thickness if it is amorphous.

Overall, it can be concluded that the inclusion of separately prepared iron carbides in magnetite nanocatalysts has the ability to change the Fischer – Tropsch catalytic activity as high conversions and heavy products selectivity were obtained. The catalysts were relatively stable and resulted in an increased product distribution as more products were produced at a faster rate than with only magnetite catalysts. It is however recommended that calcinations of the iron carbide nanocatalysts prepared via the biopolymer route should be done in an inert environment. These catalysts tend to be oxidised by air very readily especially when they are still hot. It is also advised that increasing batch sizes during synthesis from the 5 grams in three days to around 10 grams will reduce the amount of time taken during catalysts preparation, but a balance should be reached as this will also affect the particle size distribution of the synthesized catalysts.

The stoichiometry of the fresh magnetite and iron carbide nanocatalysts is also important to be known as supporting information in addition to experimental PXRD phases detected. For future work, it is recommended that Mossbauer Spectroscopy be used as an additional tool to extract this information.

The Gas Chromatography analysis system needs some improvement as well. Preferably an online system will be more reliable due to the fact that the offline GC sampling technique is affected by several factors. The products concentrations in the tail gas stream can be dependent on the rate at which the back pressure regulator vents off excess pressure. An online system would therefore ensure that the average product composition will be sampled over time.

References:

Abu Mukh-Qasem, R. & Gedanken, A. 2005. Sonochemical synthesis of stable hydrosol of Fe3O4 nanoparticles. *Journal of Colloid and Interface Science,* 284**,** 489-494.

Adesina, A. A. 1996. Hydrocarbon synthesis via Fischer-Tropsch reaction: travails and triumphs. *Applied Catalysis A: General,* 138**,** 345-367.

Alivisatos, A. P. 1996. Perspectives on the Physical Chemistry of Semiconductor Nanocrystals. *The Journal of Physical Chemistry,* 100**,** 13226-13239.

Amelse, J. A., Butt, J. B. & Schwartz, L. H. 1978. Carburization of supported iron synthesis catalysts. *The Journal of Physical Chemistry,* 82**,** 558-563.

Arakawa, H. & Bell, A. T. 1983. Effects of potassium promotion on the activity and selectivity of iron Fischer-Tropsch catalysts. *Industrial & Engineering Chemistry Process Design and Development,* 22**,** 97-103.

Bartholomew, C. H. 1990. Recent technological developments in Fischer-Tropsch catalysis. *Catalysis Letters,* 7**,** 303-315.

Blanchard, F., Reymond, J. P., Pommier, B. & Teichner, S. J. 1982. On the mechanism of the Fischer-Tropsch synthesis involving unreduced iron catalyst. *Journal of Molecular Catalysis,* 17**,** 171-181.

Bo, S., Ke, X., Luan, N., Minghua, Q., *et al.* 2012. Preparation and Catalysis of Carbon-Supported Iron Catalysts for Fischer–Tropsch Synthesis. *ChemCatChem,* 4**,** 1498-1511.

Bukur, D. B., Koranne, M., Lang, X., Rao, K. R. P. M., *et al.* 1995a. Pretreatment effect studies with a precipitated iron Fischer-Tropsch catalyst. *Applied Catalysis A: General,* 126**,** 85-113.

Bukur, D. B., Lang, X. & Ding, Y. 1999. Pretreatment effect studies with a precipitated iron Fischer–Tropsch catalyst in a slurry reactor. *Applied Catalysis A: General,* 186**,** 255-275.

Bukur, D. B., Lang, X., Mukesh, D., Zimmerman, W. H., *et al.* 1990. Binder/support effects on the activity and selectivity of iron catalysts in the Fischer-Tropsch synthesis. *Industrial & Engineering Chemistry Research,* 29**,** 1588-1599.

Bukur, D. B., Lang, X., Rossin, J. A., Zimmerman, W. H., *et al.* 1989. Activation studies with a promoted precipitated iron Fischer-Tropsch catalyst. *Industrial & Engineering Chemistry Research,* 28**,** 1130-1140.

Bukur, D. B., Nowicki, L., Manne, R. K. & Lang, X. S. 1995b. Activation Studies with a Precipitated Iron Catalyst for Fischer-Tropsch Synthesis: II. Reaction Studies. *Journal of Catalysis,* 155**,** 366-375.

Burda, C., Chen, X., Narayanan, R. & El-Sayed, M. A. 2005. Chemistry and Properties of Nanocrystals of Different Shapes. *Chemical Reviews,* 105**,** 1025-1102.

Cano, L. A., Garcia Blanco, A. A., Lener, G., Marchetti, S. G., *et al.* 2017. Effect of the support and promoters in Fischer-Tropsch synthesis using supported Fe catalysts. *Catalysis Today,* 282, Part 2**,** 204-213.

Chen, D. & Xu, R. 1998. Hydrothermal synthesis and characterization of nanocrystalline Fe3O4 powders. *Materials Research Bulletin,* 33**,** 1015-1021.

Chen, W., Fan, Z., Pan, X. & Bao, X. 2008. Effect of Confinement in Carbon Nanotubes on the Activity of Fischer−Tropsch Iron Catalyst. *Journal of the American Chemical Society,* 130**,** 9414-9419.

Claeys, M. & Van Steen, E. 2004. Chapter 8 - Basic studies. *In:* STEYNBERG, A. & DRY, M. (eds.) *Studies in Surface Science and Catalysis.* Elsevier.

Coulter, K. E. & Sault, A. G. 1995. Effects of Activation on the Surface Properties of Silica-Supported Cobalt Catalysts. *Journal of Catalysis,* 154**,** 56-64.

Cushing, B. L., Kolesnichenko, V. L. & O'connor, C. J. 2004. Recent Advances in the Liquid-Phase Syntheses of Inorganic Nanoparticles. *Chemical Reviews,* 104**,** 3893-3946.

Davis, B. H. 2003. Fischer-Tropsch synthesis: relationship between iron catalyst composition and process variables. *Catalysis Today,* 84**,** 83-98.

Davis, B. H. & Occelli, M. L. 2016. *Fischer-Tropsch Synthesis, Catalysts, and Catalysis: Advances and Applications*, Taylor & Francis.

Deng, H., Li, X., Peng, Q., Wang, X., *et al.* 2005. Monodisperse Magnetic Single-Crystal Ferrite Microspheres. *Angewandte Chemie International Edition,* 44**,** 2782-2785.

Deng, Y., Wang, L., Yang, W., Fu, S., *et al.* 2003. Preparation of magnetic polymeric particles via inverse microemulsion polymerization process. *Journal of Magnetism and Magnetic Materials,* 257**,** 69-78.

Ding, M., Yang, Y., Wu, B., Wang, T., *et al.* 2011. Effect of reducing agents on microstructure and catalytic performance of precipitated iron-manganese catalyst for Fischer–Tropsch synthesis. *Fuel Processing Technology,* 92**,** 2353-2359.

Dry, M. E. & Hoogendoorn, J. C. 1981. Technology of the Fischer-Tropsch Process. *Catalysis Reviews,* 23**,** 265-278.

Enger, B. C. & Holmen, A. 2012. Nickel and Fischer-Tropsch Synthesis. *Catalysis Reviews,* 54**,** 437-488.

Espinoza, R. L., Steynberg, A. P., Jager, B. & Vosloo, A. C. 1999. Low temperature Fischer–Tropsch synthesis from a Sasol perspective. *Applied Catalysis A: General,* 186**,** 13-26.

Fan, R., Chen, X. H., Gui, Z., Liu, L., *et al.* 2001. A new simple hydrothermal preparation of nanocrystalline magnetite Fe3O4. *Materials Research Bulletin,* 36**,** 497-502.

Fischer, F. & Tropsch, H. 1926. *International Conference on Bituminous Coal, Vol. 7***,** 97-104.

Gallei, E. F., Hesse, M. & Schwab, E. 2008. Development of Industrial Catalysts. *Handbook of Heterogeneous Catalysis.* Wiley-VCH Verlag GmbH & Co. KGaA.

Gedanken, A. 2004. Using sonochemistry for the fabrication of nanomaterials. *Ultrasonics Sonochemistry,* 11**,** 47-55.

Geus, J. W. & Van Dillen, A. J. 2008. Preparation of Supported Catalysts by Deposition–Precipitation. *Handbook of Heterogeneous Catalysis.* Wiley-VCH Verlag GmbH & Co. KGaA.

Gnanamani, M. K., Hamdeh, H. H., Shafer, W. D., Sparks, D. E., *et al.* 2013. Fischer–Tropsch Synthesis: Effect of Potassium on Activity and Selectivity for Oxide and Carbide Fe Catalysts. *Catalysis Letters,* 143**,** 1123-1131.

Hao, Q.-L., Liu, F.-X., Wang, H., Chang, J., *et al.* 2007. Effect of reduction temperature on a spray-dried iron-based catalyst for slurry Fischer–Tropsch synthesis. *Journal of Molecular Catalysis A: Chemical,* 261**,** 104-111.

Henglein, A. 1989. Small-particle research: physicochemical properties of extremely small colloidal metal and semiconductor particles. *Chemical Reviews,* 89**,** 1861-1873.

Herranz, T., Rojas, S., Pérez-Alonso, F. J., Ojeda, M., *et al.* 2006. Genesis of iron carbides and their role in the synthesis of hydrocarbons from synthesis gas. *Journal of Catalysis,* 243**,** 199-211.

Hooff, E. B. M. D. a. J. H. V. V. 1993. Chapter 8 Preparation of Catalyst supports and zeolites. *In:* MOULIJN, J. A., VAN LEEUWEN, P. W. N. M. & VAN SANTEN, R. A. (eds.) *Studies in Surface Science and Catalysis.* Elsevier.

Hyeon, T., Lee, S. S., Park, J., Chung, Y., *et al.* 2001. Synthesis of Highly Crystalline and Monodisperse Maghemite Nanocrystallites without a Size-Selection Process. *Journal of the American Chemical Society,* 123**,** 12798-12801.

J.W. Geus, J. a. R. V. V. 1993. Chapter 9 Preparation of supported catalysts. *In:* MOULIJN, J. A., VAN LEEUWEN, P. W. N. M. & VAN SANTEN, R. A. (eds.) *Studies in Surface Science and Catalysis.* Elsevier.

Jacobs, T. 2013. Gas-to-Liquids Comes of Age in a World Full of Gas. *Journal of Petroleum Technology,* 65**,** 68-73.

Jager, B. & Espinoza, R. 1995. Advances in low temperature Fischer-Tropsch synthesis. *Catalysis Today,* 23**,** 17-28.

Jana, N. R., Chen, Y. & Peng, X. 2004. Size- and Shape-Controlled Magnetic (Cr, Mn, Fe, Co, Ni) Oxide Nanocrystals via a Simple and General Approach. *Chemistry of Materials,* 16**,** 3931-3935.

Jun, Y. W., Choi, J. S. & Cheon, J. 2006. Shape control of semiconductor and metal oxide nanocrystals through nonhydrolytic colloidal routes. *Angew Chem Int Ed Engl,* 45**,** 3414-39.

Kang, Y. S., Risbud, S., Rabolt, J. F. & Stroeve, P. 1996. Synthesis and Characterization of Nanometer-Size Fe3O4 and γ-Fe2O3 Particles. *Chemistry of Materials,* 8**,** 2209-2211.

Khodakov, A. Y., Chu, W. & Fongarland, P. 2007. Advances in the Development of Novel Cobalt Fischer−Tropsch Catalysts for Synthesis of Long-Chain Hydrocarbons and Clean Fuels. *Chemical Reviews,* 107**,** 1692-1744.

Kim, D. K., Mikhaylova, M., Zhang, Y. & Muhammed, M. 2003. Protective Coating of Superparamagnetic Iron Oxide Nanoparticles. *Chemistry of Materials,* 15**,** 1617-1627.

Kim, D. K., Zhang, Y., Voit, W., Rao, K. V., *et al.* 2001. Synthesis and characterization of surfactant-coated superparamagnetic monodispersed iron oxide nanoparticles. *Journal of Magnetism and Magnetic Materials,* 225**,** 30-36.

Li, H., Li, H., Zhang, J., Dai, W., *et al.* 2007. Ultrasound-assisted preparation of a highly active and selective Co-B amorphous alloy catalyst in uniform spherical nanoparticles. *Journal of Catalysis,* 246**,** 301-307.

Li, S., Krishnamoorthy, S., Li, A., Meitzner, G. D., *et al.* 2002. Promoted Iron-Based Catalysts for the Fischer–Tropsch Synthesis: Design, Synthesis, Site Densities, and Catalytic Properties. *Journal of Catalysis,* 206**,** 202-217.

Liu, X.-W., Cao, Z., Zhao, S., Gao, R., *et al.* 2017. Iron Carbides in Fischer–Tropsch Synthesis: Theoretical and Experimental Understanding in Epsilon-Iron Carbide Phase Assignment. *The Journal of Physical Chemistry C,* 121**,** 21390-21396.

Liu, Y., Chen, J.-F., Bao, J. & Zhang, Y. 2015. Manganese-Modified Fe3O4 Microsphere Catalyst with Effective Active Phase of Forming Light Olefins from Syngas. *ACS Catalysis,* 5**,** 3905-3909.

Livage, J., Henry, M. & Sanchez, C. 1988. Sol-gel chemistry of transition metal oxides. *Progress in Solid State Chemistry,* 18**,** 259-341.

Loaiza-Gil, A., Fontal, B., Rueda, F., Mendialdua, J., *et al.* 1999. On carbonaceous deposit formation in carbon monoxide hydrogenation on a natural iron catalyst. *Applied Catalysis A: General,* 177**,** 193-203.

Lokhat, D., Oliver, M. & Carsky, M. 2015. Preparation of iron oxide nanocatalysts and application in the liquid phase oxidation of benzene. 17**,** 43.

Luo, M., Hamdeh, H. & Davis, B. H. 2009. Fischer-Tropsch Synthesis: Catalyst activation of low alpha iron catalyst. *Catalysis Today,* 140**,** 127-134.

Marceau, E., Carrier, X., Che, M., Clause, O., *et al.* 2008. Ion Exchange and Impregnation. *Handbook of Heterogeneous Catalysis.* Wiley-VCH Verlag GmbH & Co. KGaA.

Massart, R. 1981. Preparation of aqueous magnetic liquids in alkaline and acidic media. *IEEE Transactions on Magnetics,* 17**,** 1247-1248.

Matijevic, E. 1993. Preparation and properties of uniform size colloids. *Chemistry of Materials,* 5**,** 412-426.

Mccullen, S. 1990. *Aromatization process and catalyst utilizing a mixture of shape-selective porous crystalline silicate zeolite and pillared layered metal oxideoxide,* United States.

Moodley, D. J., Van De Loosdrecht, J., Saib, A. M., Overett, M. J., *et al.* 2009. Carbon deposition as a deactivation mechanism of cobalt-based Fischer–Tropsch synthesis catalysts under realistic conditions. *Applied Catalysis A: General,* 354**,** 102-110.

Morales, F. & Weckhuysen, B. M. 2006. Promotion effects in Co-based Fischer-Tropsch catalysis. *Catalysis.*

Motjope, T. R., Dlamini, H. T., Hearne, G. R. & Coville, N. J. 2002. Application of in situ Mössbauer spectroscopy to investigate the effect of precipitating agents on precipitated iron Fischer–Tropsch catalysts. *Catalysis Today,* 71**,** 335-341.

Ngantsoue-Hoc, W., Zhang, Y., O'brien, R. J., Luo, M., *et al.* 2002. Fischer−Tropsch synthesis: activity and selectivity for Group I alkali promoted iron-based catalysts. *Applied Catalysis A: General,* 236**,** 77-89.

Niederberger, M., Garnweitner, G., Buha, J., Polleux, J., *et al.* 2006. Nonaqueous synthesis of metal oxide nanoparticles:Review and indium oxide as case study for the dependence of particle morphology on precursors and solvents. *Journal of Sol-Gel Science and Technology,* 40**,** 259-266.

Niederberger, M., Garnweitner, G., Pinna, N. & Neri, G. 2005. Non-aqueous routes to crystalline metal oxide nanoparticles: Formation mechanisms and applications. *Progress in Solid State Chemistry,* 33**,** 59-70.

Niemantsverdriet, J. W. 2007. *Spectroscopy in catalysis: an introduction,* John Wiley & Sons.

Nijs, H. H. & Jacobs, P. A. 1980. Metal particle size distributions and Fischer-Tropsch selectivity. An extended Schulz-Flory model. *Journal of Catalysis,* 65**,** 328-334.

Nikitenko, S. I., Koltypin, Y., Felner, I., Yeshurun, I., *et al.* 2004. Tailoring the Properties of Fe−Fe3C Nanocrystalline Particles Prepared by Sonochemistry. *The Journal of Physical Chemistry B,* 108**,** 7620-7626.

Parkinson, B. 1995. The Emerging Art of Solid-State Synthesis. *Science,* 270**,** 1157-1158.

Perego, C. & Villa, P. 1997. Catalyst preparation methods. *Catalysis Today,* 34**,** 281-305.

Pileni, M. P. 2001. Nanocrystal Self-Assemblies: Fabrication and Collective Properties. *The Journal of Physical Chemistry B,* 105**,** 3358-3371.

Pileni, M. P. 2003. The role of soft colloidal templates in controlling the size and shape of inorganic nanocrystals. *Nat Mater,* 2**,** 145-50.

Pillai, V., Kumar, P., Hou, M. J., Ayyub, P., *et al.* 1995. Preparation of nanoparticles of silver halides, superconductors and magnetic materials using water-in-oil microemulsions as nano-reactors. *Advances in Colloid and Interface Science,* 55**,** 241-269.

Pinna, N., Grancharov, S., Beato, P., Bonville, P., *et al.* 2005. Magnetite Nanocrystals: Nonaqueous Synthesis, Characterization, and Solubility. *Chemistry of Materials,* 17**,** 3044-3049.

Pinna, N., Karmaoui, M. & Willinger, M.-G. 2011. The "benzyl alcohol route": An elegant approach towards doped and multimetal oxide nanocrystals. *Journal of Sol-Gel Science and Technology,* 57**,** 323-329.

Rao, K. R. P. M., Huggins, F. E., Huffman, G. P., Gormley, R. J., *et al.* 1996. Mössbauer Study of Iron Fischer−Tropsch Catalysts during Activation and Synthesis. *Energy & Fuels,* 10**,** 546-551.

Raupp, G. B. & Delgass, W. N. 1979. Mössbauer investigation of supported Fe catalysts: III. In situ kinetics and spectroscopy during Fischer-Tropsch synthesis. *Journal of Catalysis,* 58**,** 361-369.

Reuel, R. C. & Bartholomew, C. H. 1984a. Effects of support and dispersion on the CO hydrogenation activity/selectivity properties of cobalt. *Journal of Catalysis,* 85**,** 78-88.

Reuel, R. C. & Bartholomew, C. H. 1984b. The stoichiometries of H2 and CO adsorptions on cobalt: Effects of support and preparation. *Journal of Catalysis,* 85**,** 63-77.

Reymond, J. P., Mériaudeau, P. & Teichner, S. J. 1982. Changes in the surface structure and composition of an iron catalyst of reduced or unreduced Fe2O3 during the reaction of carbon monoxide and hydrogen. *Journal of Catalysis,* 75**,** 39-48.

Rosynek, M. P. & Polansky, C. A. 1991. Effect of cobalt source on the reduction properties of silica-supported cobalt catalysts. *Applied Catalysis,* 73**,** 97-112.

Saeidi, S., Amiri, M. T., Amin, N. a. S. & Rahimpour, M. R. 2014. Progress in reactors for high-temperature Fischer–Tropsch process: determination place of intensifier reactor perspective. *International Journal of Chemical Reactor Engineering,* 12**,** 639-664.

Schnepp, Z., Wimbush, S. C., Antonietti, M. & Giordano, C. 2010. Synthesis of Highly Magnetic Iron Carbide Nanoparticles via a Biopolymer Route. *Chemistry of Materials,* 22**,** 5340-5344.

Schulz, H. 1999. Short history and present trends of Fischer–Tropsch synthesis. *Applied Catalysis A: General,* 186**,** 3-12.

Schulz, H., Beck, K. & Erich, E. 1988. Mechanism of the Fischer Tropsch Process. *In:* BIBBY, D. M., CHANG, C. D., HOWE, R. F. & YURCHAK, S. (eds.) *Studies in Surface Science and Catalysis.* Elsevier.

Sewell, G. S., Van Steen, E. & O'connor, C. T. 1996. Use of TPR/TPO for characterization of supported cobalt catalysts. *Catalysis Letters,* 37**,** 255-260.

Shroff, M. D., Kalakkad, D. S., Coulter, K. E., Kohler, S. D., *et al.* 1995. Activation of Precipitated Iron Fischer-Tropsch Synthesis Catalysts. *Journal of Catalysis,* 156**,** 185-207.

Subramanian, V., Ordomsky, V. V., Legras, B., Cheng, K., *et al.* 2016. Design of iron catalysts supported on carbon-silica composites with enhanced catalytic performance in high-temperature Fischer-Tropsch synthesis. *Catalysis Science & Technology,* 6**,** 4953-4961.

Sun, S. & Zeng, H. 2002. Size-Controlled Synthesis of Magnetite Nanoparticles. *Journal of the American Chemical Society,* 124**,** 8204-8205.

Sun, S., Zeng, H., Robinson, D. B., Raoux, S., *et al.* 2004. Monodisperse MFe2O4 (M = Fe, Co, Mn) Nanoparticles. *Journal of the American Chemical Society,* 126**,** 273-279.

Suslick, K. S. & Price, G. J. 1999. APPLICATIONS OF ULTRASOUND TO MATERIALS CHEMISTRY. *Annual Review of Materials Science,* 29**,** 295-326.

Tau, L.-M., Dabbagh, H. A., Chawla, B. & Davis, B. H. 1990. Fischer-Tropsch synthesis with an iron catalyst: Incorporation of ethene into higher carbon number alkanes. *Catalysis Letters,* 7**,** 141-149.

Twigg, M. V. 1989. *CATALYST handbook,* London, Wolfe Publishing.

Van Steen, E. & Claeys, M. 2008. Fischer-Tropsch Catalysts for the Biomass-to-Liquid (BTL)-Process. *Chemical Engineering & Technology,* 31**,** 655-666.

Vijayakumar, R., Koltypin, Y., Felner, I. & Gedanken, A. 2000. Sonochemical synthesis and characterization of pure nanometer-sized Fe3O4 particles. *Materials Science and Engineering: A,* 286**,** 101-105.

Wang, H., Yang, Y., Wu, B.-S., Xu, J., *et al.* 2009. Hydrogen reduction kinetics modeling of a precipitated iron Fischer–Tropsch catalyst. *Journal of Molecular Catalysis A: Chemical,* 308**,** 96-107.

Wang, J., Sun, J., Sun, Q. & Chen, Q. 2003. One-step hydrothermal process to prepare highly crystalline Fe3O4 nanoparticles with improved magnetic properties. *Materials Research Bulletin,* 38**,** 1113-1118.

Wang, L., Bao, J., Wang, L., Zhang, F., *et al.* 2006. One-Pot Synthesis and Bioapplication of Amine-Functionalized Magnetite Nanoparticles and Hollow Nanospheres. *Chemistry – A European Journal,* 12**,** 6341-6347.

Weil, B. H. & Lane, J. C. 1949. *The technology of the Fischer-Tropsch process,* London, Constable & Co.

Xue-Mei, L., Gaojie, X., Yue, L. & Tao, H. 2011. Magnetic Fe3O4 Nanoparticles: Synthesis and Application in Water Treatment. *Nanoscience & Nanotechnology-Asia,* 1**,** 14-24.

Yamaura, M., Camilo, R. L., Sampaio, L. C., Macêdo, M. A., *et al.* 2004. Preparation and characterization of (3-aminopropyl)triethoxysilane-coated magnetite nanoparticles. *Journal of Magnetism and Magnetic Materials,* 279**,** 210-217.

Yan, A., Liu, X., Qiu, G., Wu, H., *et al.* 2008. Solvothermal synthesis and characterization of size-controlled Fe3O4 nanoparticles. *Journal of Alloys and Compounds,* 458**,** 487-491.

Yan, Q., Wan, C., Liu, J., Gao, J., *et al.* 2013. Iron nanoparticles in situ encapsulated in biochar-based carbon as an effective catalyst for the conversion of biomass-derived syngas to liquid hydrocarbons. *Green Chemistry,* 15**,** 1631-1640.

Yan, Z., Wang, Z., Bukur, D. B. & Goodman, D. W. 2009. Fischer–Tropsch synthesis on a model Co/SiO2 catalyst. *Journal of Catalysis,* 268**,** 196-200.

Yang, Y., Xiang, H.-W., Xu, Y.-Y., Bai, L., *et al.* 2004. Effect of potassium promoter on precipitated iron-manganese catalyst for Fischer–Tropsch synthesis. *Applied Catalysis A: General,* 266**,** 181-194.

Yen, F. S., Chen, W. C., Yang, J. M. & Hong, C. T. 2002. Crystallite Size Variations of Nanosized Fe2O3 Powders during γ- to α-Phase Transformation. *Nano Letters,* 2**,** 245-252.

Zhang, D., Tong, Z., Li, S., Zhang, X., *et al.* 2008. Fabrication and characterization of hollow Fe3O4 nanospheres in a microemulsion. *Materials Letters,* 62**,** 4053-4055.

Zheng, S., Sun, J., Song, D., Chen, Z., *et al.* 2015. The facile fabrication of magnetite nanoparticles and their enhanced catalytic performance in Fischer-Tropsch synthesis. *Chemical Communications,* 51**,** 11123-11125.

Zhou, Z. H., Wang, J., Liu, X. & Chan, H. S. O. 2001. Synthesis of FeO nanoparticles from emulsions. *Journal of Materials Chemistry,* 11**,** 1704-1709.

Zhu, L., Xiu, Y., Xu, J., Tamirisa, P. A., *et al.* 2005. Superhydrophobicity on Two-Tier Rough Surfaces Fabricated by Controlled Growth of Aligned Carbon Nanotube Arrays Coated with Fluorocarbon. *Langmuir,* 21**,** 11208-11212.

Zsoldos, Z., Garin, F., Hilaire, L. & Guczi, L. 1996. Genesis of cobalt oxide-induced surface structure in PtCoxAl2O3 catalysts. *Journal of Molecular Catalysis A: Chemical,* 111**,** 113-122.

van Santen, R.A., Ciobica, I. M., van Steen, E. and Ghouri, M.M. (2011), 'Chapter 3- Mechanistic issues in Fischer-Tropsch catalysis', *Advances in Catalysis* **54**, 127.

Appendix A:

XRD Spectra and Peak lists:

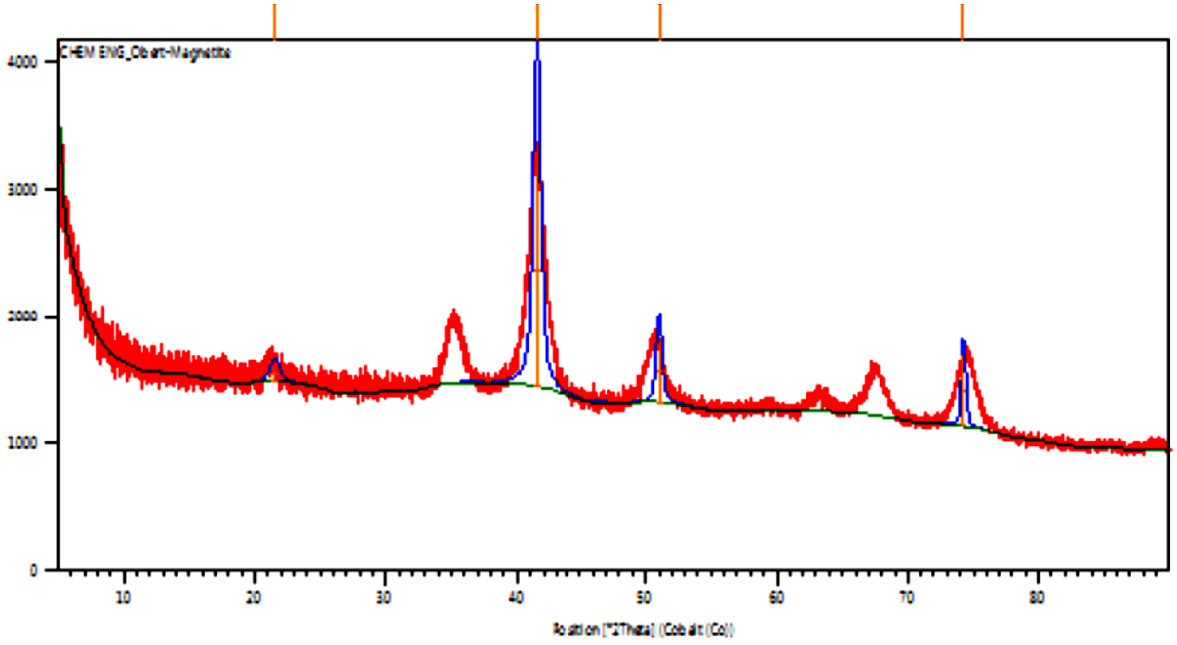

Figure A1: Magnetite XRD spectrum showing some of the major peaks that were detected.

Peak List

Pos.[°2Th.]	Height [cts]	FWHMLeft[°2Th.]	d-spacing [Å]	Rel. Int. [%]
21.5118	118.38	0.8817	4.79652	6.37
41.5028	1858.24	0.6927	2.52644	100.00
50.9968	490.63	0.5038	2.07940	26.40
[illegible]				
74.2009	567.26	0.3149	1.48397	30.53

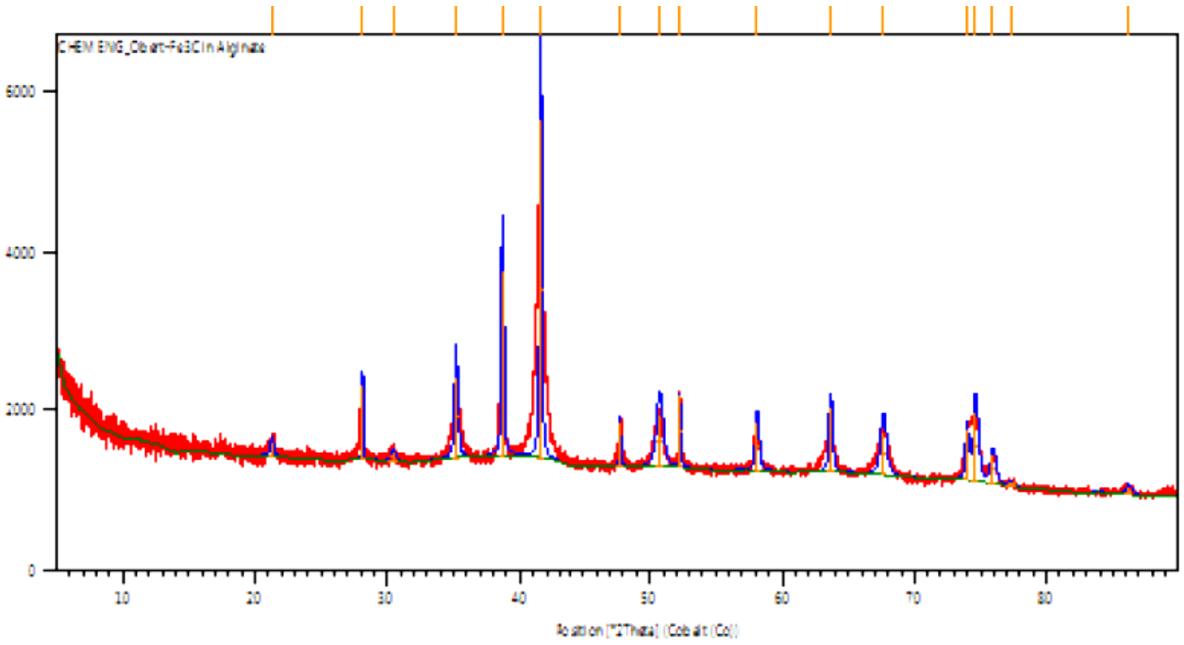

Figure A2: XRD spectrum showing some of the major iron carbide peaks that were detected from the sample prepared via the ammonium alginate biopolymer route.

Peak List

Pos.[°2Th.]	Height [cts]	FWHMLeft[°2Th.]	d-spacing [Å]	Rel. Int. [%]
21.2664	152.72	0.2519	4.85124	3.58
28.1085	926.43	0.0945	3.68617	21.72
30.4240	105.57	0.3779	3.41152	2.47
35.1745	1007.92	0.2834	2.96254	23.63
38.6859	2338.65	0.1889	2.70258	54.82
41.5563	4265.84	0.1732	2.52333	100.00
47.7320	578.22	0.1102	2.21244	13.55
50.7327	644.78	0.5668	2.08950	15.12
52.3019	904.49	0.0945	2.03103	21.20
58.0948	584.14	0.2834	1.84365	13.69
63.6374	801.02	0.2519	1.69783	18.78
67.6244	548.27	0.5038	1.60862	12.85
73.9456	636.05	0.2204	1.48836	14.91
74.6117	845.78	0.3779	1.47698	19.83
75.9201	343.68	0.3779	1.45527	8.06
77.2474	50.20	0.3779	1.43407	1.18
86.1389	98.67	0.3779	1.31084	2.31

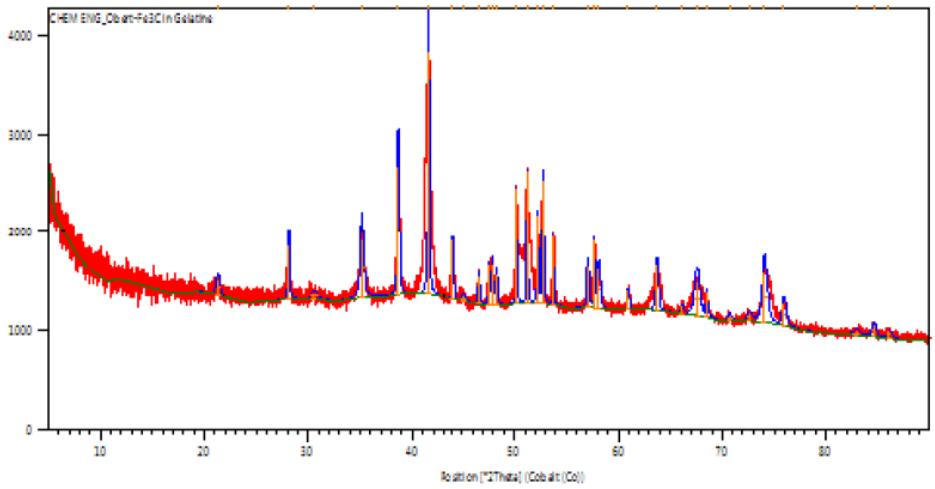

Peak List From XRD spectrum of iron carbide of nanoparticles prepared via the gelatin biopolymer route.

Pos.[°2Th.]	Height [cts]	FWHMLeft[°2Th.]	d-spacing [Å]	Rel. Int. [%]
21.2899	151.28	0.3779	4.84594	6.12
28.1139	535.75	0.1574	3.68549	21.66
30.5466	52.13	0.7557	3.39815	2.11
35.1505	595.60	0.3779	2.96449	24.08
38.6548	1311.44	0.1889	2.70467	53.03
41.5464	2472.95	0.1417	2.52391	100.00
44.0745	596.45	0.1102	2.38574	24.12
45.0811	52.92	0.3779	2.33516	2.14
46.5631	289.26	0.1574	2.26478	11.70
47.5402	399.89	0.0945	2.22085	16.17
47.8741	414.23	0.1574	2.20627	16.75
48.2812	314.69	0.1574	2.18876	12.73
50.2049	1176.65	0.0787	2.11002	47.58
51.2296	1349.74	0.0787	2.07059	54.58
52.2272	901.98	0.1102	2.03374	36.47
52.7389	1275.39	0.1260	2.01540	51.57
53.7582	696.07	0.0787	1.97995	28.15
57.0631	420.24	0.1889	1.87411	16.99
57.7037	690.07	0.0945	1.85506	27.90
58.1354	393.69	0.2204	1.84248	15.92
60.9620	186.57	0.1574	1.76471	7.54
63.7025	460.35	0.2204	1.69628	18.62
66.1303	81.19	0.2519	1.64070	3.28
67.5472	350.71	0.5668	1.61024	14.18
68.5128	266.15	0.1260	1.59026	10.76
70.7028	53.25	0.3779	1.54713	2.15
72.5817	70.40	0.3779	1.51238	2.85
74.0540	503.57	0.5038	1.48649	20.36
75.9380	229.07	0.3779	1.45498	9.26
82.8660	48.10	0.7557	1.35272	1.95
84.5707	124.81	0.3779	1.33044	5.05
86.0689	67.37	0.3779	1.31170	2.72

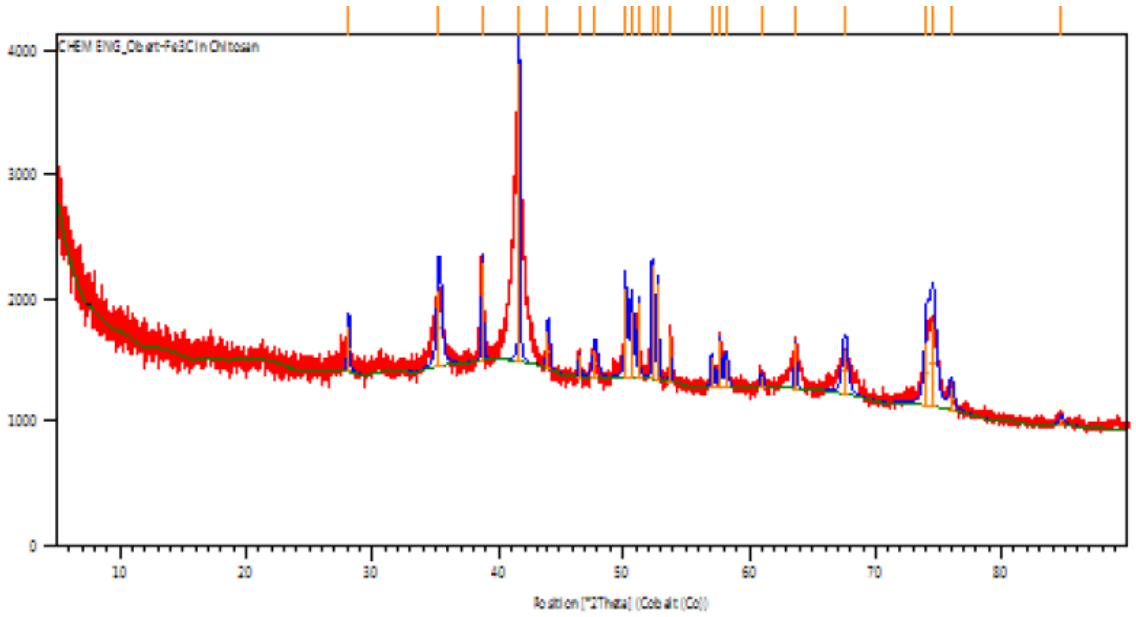

Peak List from XRD spectrum of iron carbide of nanoparticles prepared via the chitosan biopolymer route.

Pos. [°2Th.]	Height [cts]	FWHMLeft [°2Th.]	d-spacing [Å]	Rel. Int. [%]
28.0861	364.90	0.1574	3.68906	15.11
35.2827	621.17	0.4408	2.95374	25.73
38.6968	809.80	0.0945	2.70185	33.54
41.6033	2414.19	0.1102	2.52061	100.00
44.0742	300.43	0.2519	2.38576	12.44
46.5309	183.17	0.0945	2.26626	7.59
47.7977	224.65	0.4408	2.20958	9.31
50.2047	736.60	0.1574	2.11003	30.51
50.6783	524.44	0.3149	2.09160	21.72
51.2271	618.79	0.0630	2.07068	25.63
52.3286	942.57	0.0787	2.03007	39.04
52.7119	777.08	0.1417	2.01636	32.19
53.7427	361.75	0.0787	1.98048	14.98
57.0376	238.34	0.1574	1.87487	9.87
57.6596	375.24	0.1102	1.85636	15.54
58.1668	231.60	0.2519	1.84157	9.59
60.9772	97.00	0.2519	1.76431	4.02
63.6405	363.58	0.1260	1.69776	15.06
67.5546	349.21	0.5038	1.61008	14.47
74.0090	518.29	0.3779	1.48727	21.47
74.5131	686.48	0.5668	1.47865	28.44
75.9615	185.04	0.3779	1.45459	7.66
84.6921	58.65	0.3779	1.32890	2.43

Appendix B:

Sample Chromatograms:

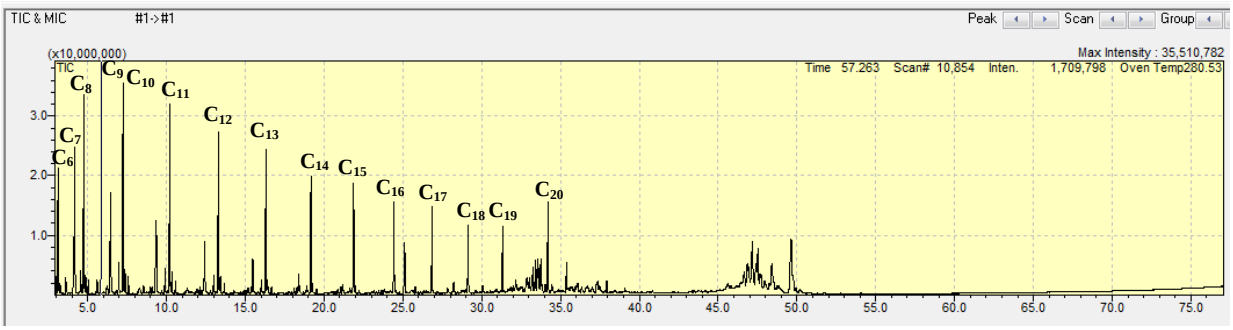

Figure B1: GC – MS chromatogram from the aqueous liquid phase analysis of hydrocarbons from the cold catch pot.

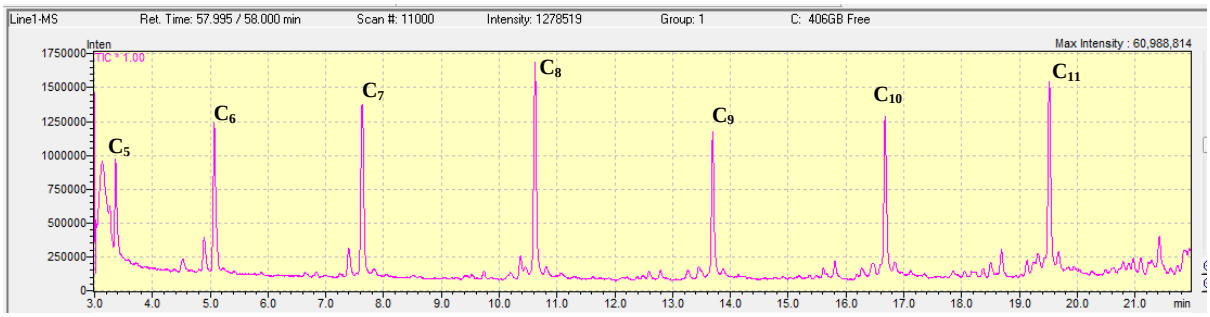

Figure B2: GC – MS chromatogram from the organic liquid phase analysis of hydrocarbons from the cold catch pot.

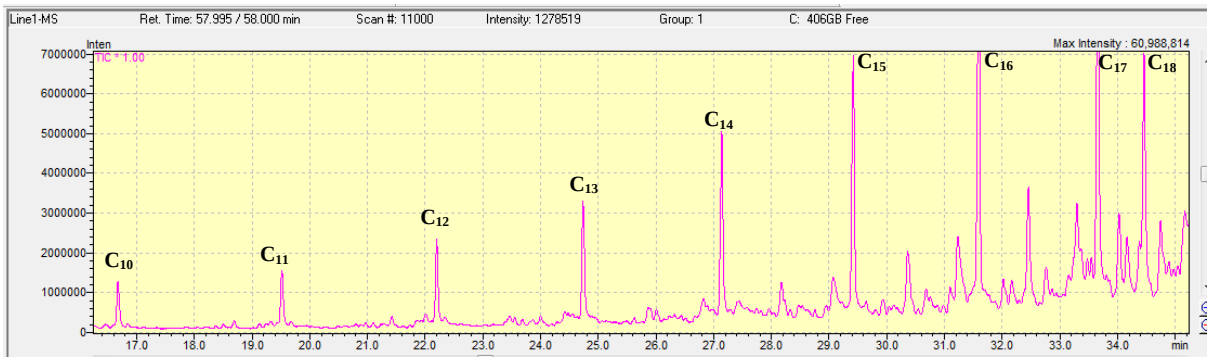

Figure B3: GC – MS chromatogram from the liquid phase analysis of hydrocarbons that remained in the reactor.

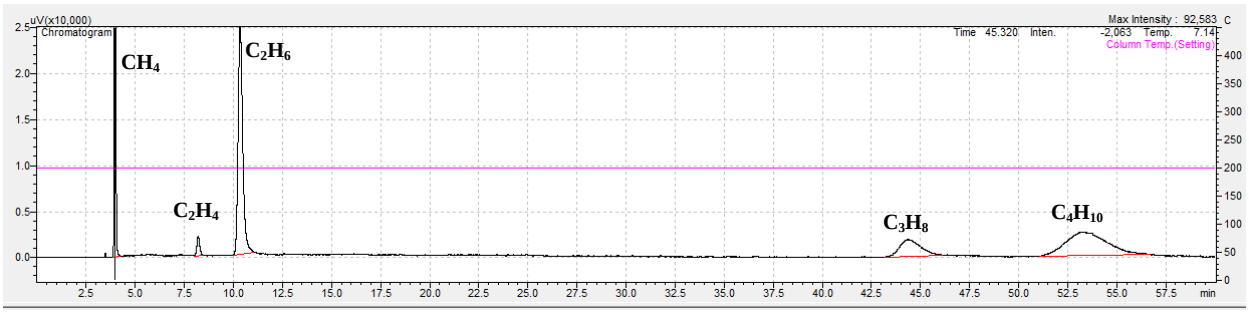

Figure B4: GC – FID chromatogram from the gaseous phase analysis of hydrocarbons.

Sample calculations:

Given the peak areas of the reactants, products and the standard gas which was Nitrogen in this work, the flow rates of the various products were calculated as illustrated below:

The following tables show the relevant data that was required for the calculations.

Compound Name	f_{TCD}
H_2	0.09544005
N_2	1
CO	0.890008594
CH_4	0.263319937
CO_2	0.911295209

Compound Name	Products Area	Reactants Area
H_2	5325486.3	8832817
N_2	103051.6	115814.6
CO	43703.8	85554.8
CH_4	21330.6	0

The flow rate of the standard gas N_2 is calculated using the following equation:

$$\dot{n}_{N_2} = x_{N_2} \frac{\dot{v}_{ref}(NTP)_.}{V_A}$$

Where: x_{N_2} is the mole fraction of the nitrogen in the internal standard gas = 1

$$\dot{v}_{ref}(NTP)_. = volumetric\ flow\ rate\ of\ the\ internal\ standard = 9.7 \times 10^{-6} m^3/min$$

$$V_A = Avogadro\ volume = 22.4 dm^3 = 22.4 \times 10^{-3} m^3/mol$$

Substituting these values gives

$$\dot{n}_{N_2} = 1 \times \frac{9.7 \times 10^{-6} m^3/min}{22.4 \times 10^{-3} m^3/mol} = \mathbf{4.33 \times 10^{-4} mol/min}$$

Molar flow rate of Hydrogen into the reactor is calculated as

$$\dot{n}_{H_2} = f_{TCD,H_2} \times \left(\frac{A_{H_2}}{A_{N_2}}\right) \dot{n}_{N_2}$$

Substituting values gives $= 0.0954 \times \left(\frac{8832817}{115814.6}\right) \times 4.33 \times 10^{-4}$

$$= \mathbf{3.15 \times 10^{-3} mol/min}$$

And the molar flow rate of CO into the reactor is calculated as:

$$\dot{n}_{CO} = f_{TCD,CO} \times \left(\frac{A_{CO}}{A_{N_2}}\right) \dot{n}_{N_2}$$

Substituting the values gives: $= 0.890 \times \left(\frac{85554.8}{115814.6}\right) \times 4.33 \times 10^{-4}$

$$= \mathbf{2.85 \times 10^{-4} mol/\ min}$$

Taking the reaction run that was carried out using 90% magnetite nanocatalysts in the mixture, the following calculations can be made to give the conversions: -

Molar flow rate of Hydrogen OUT of the reactor is calculated as:

$$\dot{n}_{H_2} = f_{TCD,H_2} \times \left(\frac{A_{H_2}}{A_{N_2}}\right) \dot{n}_{N_2}$$

$$= 0.0954 \times \left(\frac{5325486.3}{103051.6}\right) \times 4.33 \times 10^{-4}$$

$$= \mathbf{2.14 \times 10^{-3} mol/\ min}$$

Then the H_2 conversion as a percentage will be given by: -

$$X_{H_2} = \left(\frac{2.14 \times 10^{-3}}{3.15 \times 10^{-3}}\right) \times 100\%$$

$$= \mathbf{32.24}\%$$

The molar flow rate of Carbon monoxide OUT of the reactor is calculated as:

$$\dot{n}_{CO} = f_{TCD,CO} \times \left(\frac{A_{CO}}{A_{N_2}}\right) \dot{n}_{N_2}$$

$$= 0.890 \times \left(\frac{43703.8}{103051.6}\right) \times 4.33 \times 10^{-4}$$

$$= \mathbf{1.63 \times 10^{-4} mol/min}$$

And the Conversion will be equal to: -

$$X_{CO} = \left(\frac{1.63 \times 10^{-4}}{2.85 \times 10^{-4}}\right) \times 100\%$$

$$= \mathbf{42.49}\%.$$

Appendix C:

TEM Images for Spent Catalysts:

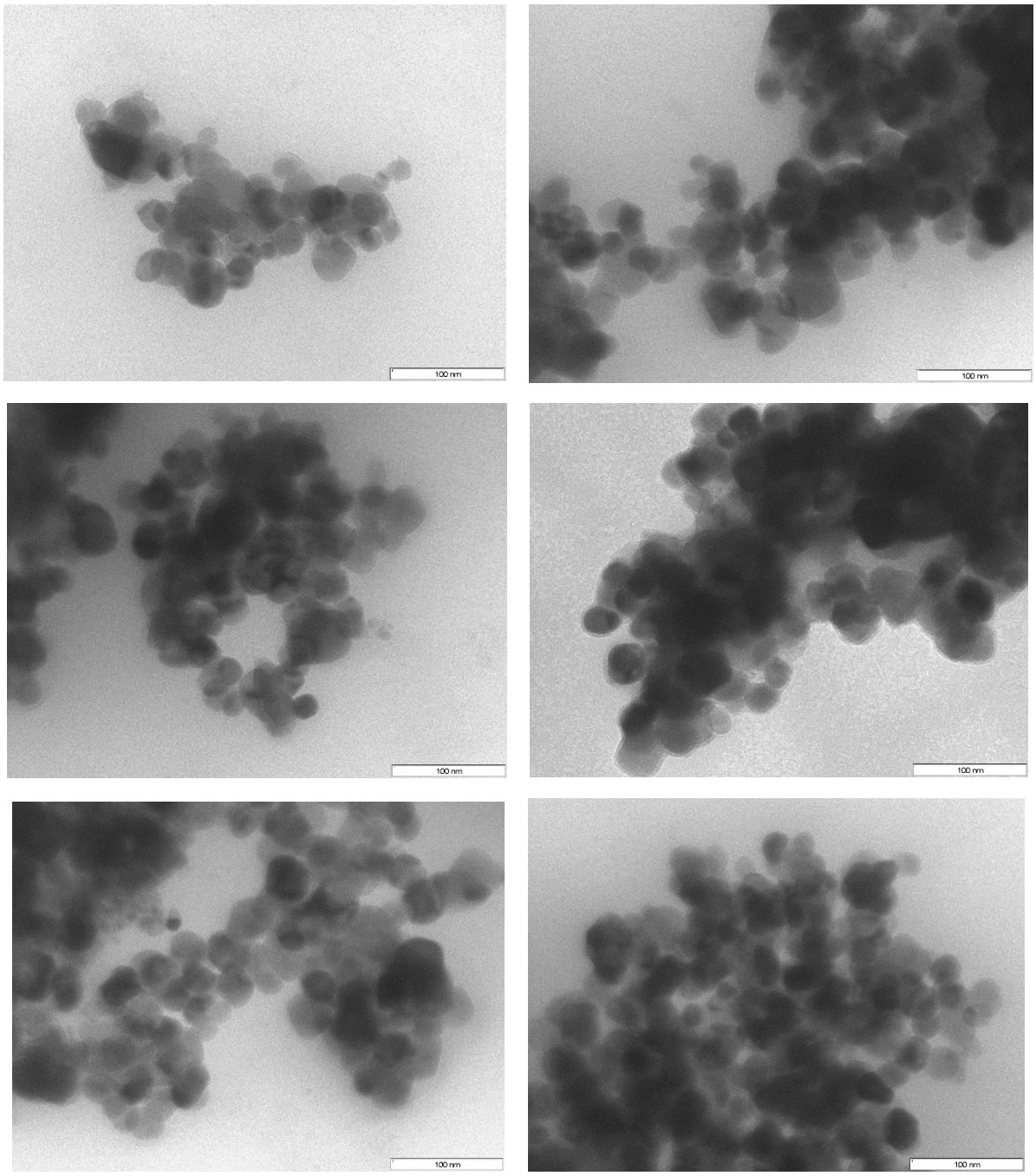

Figure C2: Some more TEM micrographs of spent catalysts analysed after 120 hours TOS.

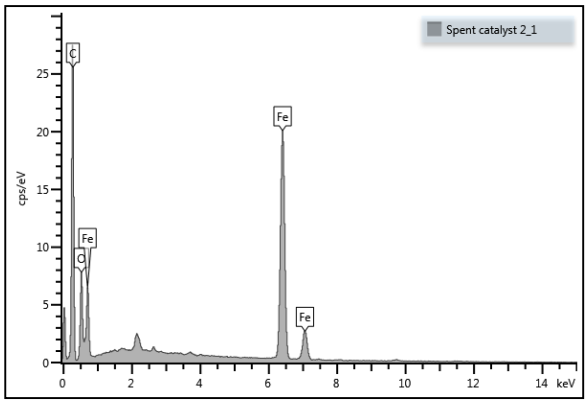

Spent catalyst 2_1	Wt%	Wt% Sigma
C	**57.38**	**0.25**
O	14.55	0.21
Fe	28.07	0.18
Total	100.00	

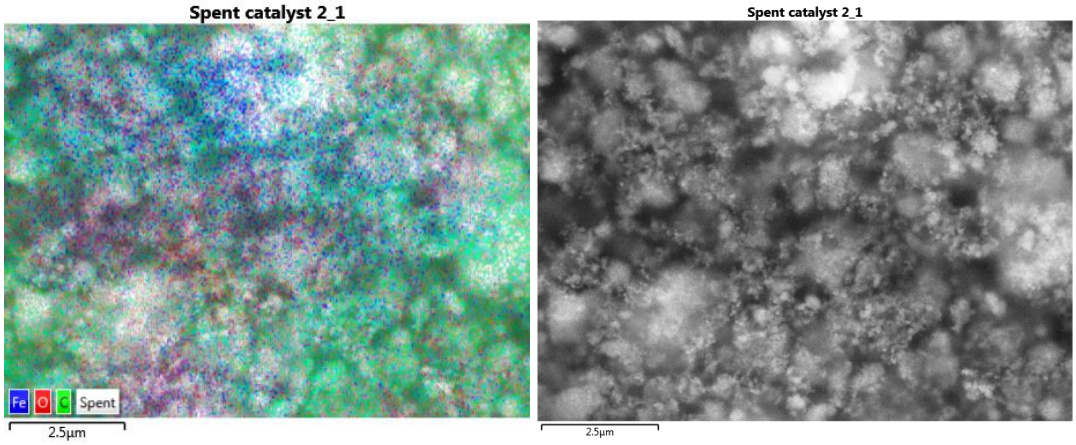

Figure C2: SEM – EDX spectrum of spent catalysts showing an increase in the carbon content.